

MOLECULAR DYNAMICS STUDY OF GEOMETRIC STABILITY, MELTING,
AND SINTERING OF CUBIC BORON NITRIDE NANOPARTICLES

by

HSIAO-FANG LEE

A Dissertation submitted to the
Graduate School-New Brunswick
Rutgers, The State University of New Jersey

In partial fulfillment of the requirements

For the degree of

Doctor of Philosophy

Graduate Program in Mechanical and Aerospace Engineering

Written under the direction of

Professor Stephen D. Tse

And approved by

New Brunswick, New Jersey

OCTOBER, 2015

ABSTRACT OF THE DISSERTATION

Molecular Dynamics Study of Geometric Stability, Melting, and Sintering of Cubic Boron Nitride Nanoparticles

By HSIAO-FANG LEE

Dissertation Director:
Professor Stephen D. Tse

A Molecular Dynamics (MD) study of cubic boron nitride (c-BN) nanoparticles of varying shapes and sizes is performed. Four geometric shapes of c-BN nanoparticles are investigated: (1) cube, (2) octahedron, (3) cuboctahedron, and (4) truncated octahedron, where facets have either boron or nitrogen termination. Using a Stillinger-Weber potential, the stability of the nanoparticles is determined to possess a strong crystal geometry and surface dependence, with the $\{111\}$ facet having the lowest surface energy. Surface reconstruction is observed to occur via two mechanisms: (i) transformation from less stable $\{100\}$ facets to more stable $\{111\}$ facets, and (ii) dimerization of nitrogen and boron atoms into rows on the nanoparticle surfaces. Geometric stability based on ground state energy is analyzed, with the octahedron being the most stable, followed in order by the truncated octahedron, the cuboctahedron, and the cube (least stable). However, MD simulations for dynamic melting as a function of temperature reveal that the truncated octahedron may actually be more stable than the octahedron. For detailed examination of the melting mechanism, the octahedral c-BN nanoparticle, which consists solely of $\{111\}$

facets, is focused on. Interestingly, phase separation occurs during melting of c-BN nanoparticles, resulting in the formation of segregated boron clusters inside the c-BN nanoparticles, along with the vaporization of surface nitrogen atoms. Four different sized octahedral c-BN nanoparticles are examined, i.e. 2.04 nm (969 atoms), 2.55 nm (1771 atoms), 3.57 nm (4495 atoms), and 4.59 nm (9139 atoms), in order to study the dependence of the melting point temperature on size. The Lindemann index of different concentric shells that comprise the nanoparticle, as well as the average Lindemann index for the entire nanoparticle, is utilized to assess melting of the nanoparticle. This assessment is compared with models considering coordination number, cohesive energy, and geometric factors, which all consistently show the large drop in melting point temperature for smaller nanoparticles. Finally, particle-particle collision of two equal-sized octahedral c-BN nanoparticles at various initial temperatures, 2500 K to 3100 K with an increment of 200 K, is investigated in isolated environments using MD simulations to evaluate the optimal temperature range for sintering. The results show that the alignment of the $\{111\}$ orientation of the two-aggregated nanoparticles occurs at a temperature slightly above the melting point, and rapid grain growth is observed when the temperature is about a few hundred degrees higher than the melting point. However, phase separation also takes place at the corners away from the plane of collision of the aggregated nanoparticles. During sintering of the two 2.55 nm octahedron c-BN nanoparticles, rapid grain growth with a nice crystallographic $\{111\}$ facet occurs between 3100 K and 3250 K; however, above 3300 K, phase separation dominates and drives melting of the entire sintered nanocluster.

Preface

Much of the content in Chapters 3, 4, 5, 6, and 7 are verbatim from soon to be submitted papers with collaborators; and I have obtained permission from the co-authors to include them in this thesis. Also, other chapters have wording similar to or identical to that found in the paper and drafts referenced in this section.

References

1. Lee, H.-F., Esfarjani, K., Dong, Z., Pelegri, A. A., Kear, B. H., and Tse, S. D., Insights into Melting of Cubic Boron Nitride Nanoparticles from Molecular Dynamics Simulations, manuscript in preparation.
2. Lee, H.-F., Esfarjani, K., Pelegri, A. A., Kear, B. H., and Tse, S. D., Sintering of Cubic Boron Nitride Nanoparticles – A Molecular Dynamics Approach, manuscript in preparation.

Acknowledgements

I am deeply appreciative of all the help and support that my adviser, Professor Stephen Tse, has provided, and most especially for his forbearance and kind understanding throughout my PhD career, which was interrupted by a change of project and the arrival of my baby daughter, Edelyn. His keen intellect and deep scientific knowledge were very helpful to my research and dissertation writing. I am also very grateful to my co-adviser, Professor Mina Pelegri, for her unfailing encouragement and kindness. The techniques I learnt from her lab are very practical and will be invaluable for my future career. I am extremely lucky to have another co-adviser, Professor Keivan Esfarjani, and it is very inspiring to work with him. His extensive experience and deep insight helped me breakthrough the impasse in my research at the mid-point of my PhD career. Under Prof. Esfarjani and Prof. Tse's mentorship, we finally managed to achieve significant results and new scientific contributions in my research. Many thanks should be given to them three for helping me complete my PhD study. In addition, I would like to thank Professor Alberto Cuitino and Professor Bernard Kear for serving on my thesis committee, and to Professor Stephen Garofalini and Professor Peter Kroll for informative discussions on SW potential and Tersoff potential.

I also thank all the professional fellows and my labmates who have given me assistance along my research path, Dr. Jafar Al-Sharab, Dr. Bob Horvath, Dr. Zhizhong Dong, Dr. Gang Xiong, Dr. Yiyang Zhang, Dr. Stuart Deutsch, Dr. Yiwen Fu, Hadi Halim, Jonathon Dolye, Max Tenorio, and Xiaodong Zhao. Especially, I would like to thank Dr. Tze Tzen Ong for research discussion and guidance.

The financial support from the Office of Naval Research, the U.S. Army Research Office, NASA, NSF, DARPA, and the fellowship and teaching assistantship from the MAE department at Rutgers University are gratefully acknowledged.

A deep gratitude and appreciation is owed to my dear family members, my dad, my mom, my husband, my daughter, and my parents-in-law. Thanks to them for their unconditional support and I love them deeply from my heart. I am also grateful for my meditation and Ch'an practice for opening up my world and transforming my life.

Table of Contents

ABSTRACT OF THE DISSERTATION	ii
Preface.....	iv
Acknowledgements.....	v
List of Tables	xi
List of Illustrations	xii
1. Introduction.....	1
1.1 Boron Nitride.....	1
1.2 Motivation and Objectives	3
1.3 Research Innovation and Strategies	4
1.4 Outline of This Dissertation	6
1.5 References	7
2 Literature Review.....	9
2.1 Introduction of Potentials.....	9
2.1.1 Tersoff Potential.....	9
2.1.2 Albe Potential.....	11
2.1.3 Stillinger-Weber Potential	12
2.2 Phase Stability of Nanoparticles	13
2.2.1 Diamond Structured Materials.....	14
2.2.2 Zincblende Structured Materials.....	17

2.3	Melting of Nanoparticles.....	19
2.3.1	Cohesive Energy & Average Coordination Number	19
2.3.2	Geometry Factor	21
2.4	Sintering of Nanoparticles.....	22
2.5	References	25
3	Simulation Methods	29
3.1	Introduction	29
3.2	Implementation of Potentials	29
3.2.1	Tersoff Potential.....	30
3.2.2	Albe Potential.....	31
3.2.3	Stillinger-Weber Potential	32
3.3	MD Simulation of c-BN Bulk Crystal	33
3.3.1	Properties of c-BN Bulk Crystal	33
3.3.2	Melting of c-BN Bulk Crystal.....	34
3.4	MD Simulation of c-BN nanoparticles.....	37
3.5	References	38
4	Geometric Stability and Surface Reconstruction of c-BN Nanoparticles.....	40
4.1	Introduction	40
4.2	Ground State Energy Analysis of Nanoparticle Geometry	41
4.3	Melting Estimation by Lindemann Index.....	45

4.4	Geometric Stability and Surface Reconstruction of c-BN Nanoparticles	46
4.4.1	Dimerization of {100} Facets and Formation of {111} Facets from Surface Reconstruction	46
4.4.2	Geometric Dependence of Melting Temperature of Nanoparticle	53
4.4.3	Melting Temperature and Surface Reconstruction of Spherical Nanoparticle.....	56
4.5	References	58
5	Melting of c-BN Octahedron Nanoparticles and Phase Separation during Melting.	60
5.1	Introduction	60
5.2	Melting Mechanism of c-BN Nanoparticles and Concurrent Phase Separation during Melting	60
5.2.1	Simultaneous Phase Separation and Melting of c-BN Octahedron	61
5.2.2	Qualitative Monitoring of Phase Separation & Corner-initiated Melting ..	63
5.2.3	Laser treatment of c-BN powders for validation of phase separation	65
5.3	Definition of Melting Point	67
5.3.1	Estimate of Melting Point Using Lindemann Index	67
5.3.2	Estimate of Melting Point Using Caloric Curve and Specific Heat	71
5.4	Size Dependence of Melting Point of Octahedral c-BN Nanoparticles	73
5.4.1	Size Dependence of Melting Point of Octahedral c-BN Nanoparticle	73
5.5	Surface Reconstruction Near Onset of Melting	76

5.6	References	81
6	Sintering of c-BN Octahedron Nanoparticles	83
6.1	Introduction	83
6.2	Statistical Study of Particle-Particle Collision	84
6.2.1	Initial Temperature of 2500 Kelvin	85
6.2.2	Comparison of Various Initial Temperature	92
6.3	Sintering of c-BN Nanoparticles	96
6.3.1	2500 & 2700 Kelvin.....	97
6.3.2	2900 & 3100 Kelvin.....	99
6.3.3	Concluding Remarks.....	103
6.4	References	104
7	Conclusions and Future Work	106
7.1	Review of Results and Conclusions	106
7.2	Suggestion for Future Work.....	110

List of Tables

Table 4-1: Summary of surface energy of different facets of c-BN.	42
Table 4-2: Summary of cohesive energy and average coordination number of various shapes of c-BN nanoparticles.....	58
Table 6-1. Comparison of particle-particle collision at various temperatures.....	94
Table 6-2. Surface energy of {100} & {111} facets with boron or nitrogen termination.	95

List of Illustrations

Figure 1-1 The four BN crystals (reproduced with caption from [4])	2
Figure 1-2 Structural relations among the four BN crystals (reproduced with caption from [4]).....	2
Figure 2-1 Phase stability of dehydrogenated diamond-structured (a) C (1.2 – 5.6 nm), (b) Si (1.6 – 7.3 nm), and (c) Ge (1.7 – 7.6 nm) nanoparticles (reproduced from [22])	15
Figure 2-2 Phase stability of hydrogenated diamond-structured (a) C (1.2 – 5.6 nm), (b) Si (1.6 – 7.3 nm), and (c) Ge (1.7 – 7.6 nm) nanoparticles (reproduced from [22])	16
Figure 2-3 The preferred shapes (left to right) of dehydrogenated diamond-structured (a) C, (b) Si, and (c) Ge, and dehydrogenated diamond-structured (d) C, (e) Si, and (f) Ge nanoparticles of ≥ 10000 atoms. Energetically undistinguishable shapes are not separated by a line (reproduced from [22]).....	17
Figure 2-4 Phase stability of III-V compounds. AlN, InN, GaN, and TiN are more stable in the WZ structure for $\Delta E_{WZ-ZB} < 0$ (reproduced from [30]).....	18
Figure 2-5 (a) Closed-shell 147 atom cuboctahedron (b) Closed-shell 55 atom icosahedron (shaded) and a portion of the next shell (reproduced from [38]).....	20
Figure 2-6 Parameter β for various geometric shapes (reproduced from [40])	21
Figure 2-7 Temporal evolution of vapor-phase particle growth (reproduced with caption from [43]).....	23
Figure 2-8 (a) Initial position of three exactly aligned Cu nanofibers (4.4 nm diameter) (b) position after sintering at 1000K for 34 ps (reproduced with caption from [45])	23
Figure 2-9 (a) Initial position of two exactly aligned Cu nanofibers (8.8 nm and 4.4 nm) (b) position after sintering at 1000K for 34 ps (reproduced with caption from [45]).....	23

Figure 2-10 (a) Initial position of two randomly oriented Cu nanofibers (8.8 nm and 2.2 nm) (b) position after sintering at 1000K for 32 ps (reproduced with caption from [45])	24
Figure 3-1. Octahedron c-BN nanoparticle in MD simulation with the application of Moon's Tersoff potential	31
Figure 3-2. Cohesive energy of c-BN	32
Figure 3-3. Lattice constant of c-BN as a function of temperature	34
Figure 3-4. Cubic BN with plane dislocations.....	36
Figure 3-5. Cubic BN crystal with plane dislocations in NVE with initial $T=4000\text{K}$ for 45ns.....	36
Figure 3-6. The caloric curve of c-BN crystals with plane dislocations in NVE with various initial temperatures.....	37
Figure 4-1. Surface energy of various shapes of c-BN nanoclusters. L refers to the side length, and the circled sizes are chosen for MD simulation.	44
Figure 4-2. Energy w.r.t. sizes of various shapes of c-BN nanoclusters.	44
Figure 4-3. Morphology and the corresponding SAED patterns of c-BN crystals (reproduced from [12]).	44
Figure 4-4. The overall Lindemann index of 2.55 nm octahedral c-BN nanoparticle w.r.t. temperature	46
Figure 4-5. Dimerization of c-BN $\{100\}$ facets. Relaxation of the cubic nanoparticle in microcanonical ensemble with an initial temperature of 400 K (a) the initial configuration: pink and green spheres denote boron and nitrogen respectively (b) dimerization on both boron and nitrogen terminations (c) dimerization on boron terminated $\{100\}$ facet (d) dimerization on nitrogen terminated $\{100\}$ facet.	48

Figure 4-6. Surface reconstruction on c-BN $\{100\}$ facets. Relaxation of the cubic nanoparticle in microcanonical ensemble with an initial temperature of 2400K (a) the initial configuration: pink and green spheres denote boron and nitrogen respectively (b) dimerization on both boron and nitrogen terminations (c) reconstructed $\{111\}$ facet shown in blue triangle and dimerized pairs shown in red rectangle	49
Figure 4-7. Lindemann index of cubic nanoparticle, showing the Lindemann index of both the entire nanoparticle in purple squares, and of the surface shell in blue diamonds. The inset figures show the melted nanoparticles at 2665 K and 2902 K, with significant $\{111\}$ reconstruction at 2902 K	50
Figure 4-8. Front (a) and rear (b) view of cube nanoparticle relaxed in NVE with final temperature of 2665 K. Dimerized nitrogen pairs are shown in blue rectangles, and no significant $\{111\}$ facet reconstruction is seen.....	50
Figure 4-9. Front (a) and rear (b) view of cube nanoparticle relaxed in NVE with final temperature of 2902 K. Dimerized nitrogen pairs are shown in blue rectangles, and significant $\{111\}$ facet reconstruction shown in red rectangles is seen	51
Figure 4-10. Surface reconstruction on c-BN cuboctahedral nanoparticle. Relaxation of the nanoparticle in microcanonical ensemble with an initial temperature of 2800K (a) the initial configuration: pink and green spheres denote boron and nitrogen respectively (b) reconstructed $\{111\}$ facet shown in blue triangle and dimerized pairs shown in red rectangle.....	52
Figure 4-11. Surface reconstruction on c-BN truncated octahedral nanoparticle. Relaxation of the nanoparticle in microcanonical ensemble with an initial temperature of 3400K (a) the initial configuration: pink and green spheres denote boron and nitrogen	

respectively (b) reconstructed $\{111\}$ facet shown in blue-circled areas and dimerized nitrogen atom pairs are indicated by red bars	52
Figure 4-12. Plot of Lindemann index w.r.t temperature of the entire cluster for all four shapes.....	54
Figure 4-13. Plot of Lindemann index w.r.t temperature of the surface shells for all four shapes.....	55
Figure 4-14. Surface reconstruction on c-BN spherical nanoparticle. Relaxation of the nanoparticle in microcanonical ensemble with an initial temperature of 2800K (a) the initial configuration showing $\{100\}$ and $\{111\}$ facets on surface: pink and green spheres denote boron and nitrogen respectively (b) reconstructed $\{111\}$ facet shown in blue triangle and dimerized pairs shown in red rectangle	57
Figure 4-15. Plot of Lindemann index w.r.t. temperature for all five geometries, including the sphere	57
Figure 5-1. Phase separation happens during melting of 2.04nm octahedral c-BN nanoparticle in NVT simulation with $T=3340K$. Bond structure view on main graphics and surface atom view on insets (a) the initial configuration: red represents boron, and yellow represents nitrogen (b) 500ps simulation time: melting starts from corners and small phase separated boron clusters formed (c) 1ns simulation time: melting proceeds to edges (d) 2ns simulation time: melting propagates to surfaces and the boron clusters tend to unite (e) 3ns simulation time: more than half of the nanoparticle is melted (f) 3.5ns simulation time: no crystalline c-BN is visible and phase separated boron clusters have formed in the interior of the nanoparticle.	62

Figure 5-2. The Lindemann index of each shell of the 2.04nm octahedral c-BN nanoparticle and the total number of B-N, B-B, and N-N bonds in NVE simulation with initial T=3340K.....	64
Figure 5-3. (a) Top-view TEM image of c-BN particles before laser treatment; inset shows the SAED pattern revealing its single-crystal feature. (b) TEM image of the phase separated boron particles after the laser treatment; inset shows the corresponding SAED pattern. (c) TEM image of the nanostructured c-BN, with polycrystalline structure after laser treatment as revealed by its SAED pattern in the inset.(These results were provided by Zhizhong Dong and Gang Xiong in Prof. Tse's group).....	66
Figure 5-4. Lindemann index of 2.55 nm octahedral c-BN nanoparticle w.r.t. temperature.	69
Figure 5-5. Linear fitting from the Lindemann index values of inner three shells of 2.55 nm octahedral c-BN nanoparticle shown as red dots.....	69
Figure 5-6. Lindemann index of 2.04 nm octahedral c-BN nanoparticle w.r.t. temperature.	70
Figure 5-7. Lindemann index of 3.57 nm octahedral c-BN nanoparticle w.r.t. temperature.	70
Figure 5-8. Lindemann index of 4.59 nm octahedral c-BN nanoparticle w.r.t. temperature.	71
Figure 5-9. The caloric curve of the 2.55nm octahedral c-BN nanoparticle has a jump, and the plots of the specific heat show that melting occurs at approximately 2950K.....	72

Figure 5-10. The Lindemann index of the overall nanoparticle versus temperature of varied-sized octahedral c-BN nanoparticles. The melting points are determined by the 5% deviation point from the low-temperature linear behavior.	74
Figure 5-11. The Lindemann index of the inner three shells versus temperature of varied-sized octahedral c-BN nanoparticles. The melting points are determined by the 5% deviation point from the low-temperature linear behaviour..	74
Figure 5-12. The Lindemann index of the surface shell versus temperature of varied-sized octahedral c-BN nanoparticles. Notice that there is a suppression of the Lindemann index near the onset of melting for all the sizes, indicated by the red dashed circle.....	75
Figure 5-13. Size dependence of the melting point of octahedral c-BN nanoparticles with 1% error bars included, and the predictions from several melting point depression models.	76
Figure 5-14. 2.04 nm octahderon in NVT simulation with T=2840K for 50ns. The red retangular area shows the dimered {100} face in between two blue triangular areas of {111} faces. The vertex is melted shows in yellow circled area.	78
Figure 5-15. 2.55 nm octahderon in NVT simulation with T=2968K for 40ns. The red retangular area shows the dimered {100} face in between two blue triangular areas of {111} faces. The vertex is melted shows in yellow circled area.	79
Figure 5-16. 3.57 nm octahderon in NVT simulation with T=3076K for 42ns. The red retangular areas show the dimered {100} face in between the {111} faces. The vertice are melted shows in yellow circled area.	79

Figure 5-17. 4.59 nm octahderon in NVE simulation with initial T=3500K for 3ns. The vertice are melted shows in yellow circled area and nitrogen atoms diffuse around on boron facets.	80
Figure 5-18. Surface reconstruction on c-BN {100} facets. Relaxation of the cubic nanoparticle in microcanonical ensemble with an initial temperature of 2400K (a) the initial configuration shown as bond structure seen from {100} direction (b) 0ps: red and yellow spheres denote boron and nitrogen, respectively (c) 10ps: dimerized boron pairs on {100} facet (d) 10ps: dimerized nitrogen pairs on {001} facet (e) 2700ps: reconstructed {111} facet and dimerized {100} facets on the surface of cube nanoparticle (f) 2700ps: the same orientation as (e) but shown as bond structure.	80
Figure 5-19. Morphology of c-BN clusters (reproduced from [8]).	81
Figure 6-1. Two octahedral c-BN nanoparticles with the same size for simulation of particle-particle collision.	84
Figure 6-2. 100 sets of random rotation angles for initial orientations of NP2.	85
Figure 6-3. Two Octahedron c-BN nanoparticle in MD NVE simulation with initial temperature of 2500K. (a) 0 ps: red and green spheres denote boron and nitrogen respectively (b) 70 ps: tip hitting edge (c) 75 ps: boron facet in contact with another boron facet (d) 80 ps: surface sliding and merging (e) 500 ps: reaching the maximum contact surface area.	86
Figure 6-4. The kinetic energy as a function of time showing the boron-boron collision case in 2500K.	87
Figure 6-5. Boron-boron grain boundary at the contact interface.	87

Figure 6-6. Boron-nitrogen collision in NVE with initial temperature of 2500K. (a) 0 ps: red and green spheres denote boron and nitrogen respectively (b) 73 ps: tip hitting corner (c) 80 ps: edge in contact with boron facet (d) 82 ps: nitrogen facet in contact with boron facet (e) 90 ps: sliding and merging (f) 3 ns:some atoms diffusing around the surface and formed small clusters on the surface.....	88
Figure 6-7. The kinetic energy as a function of time showing the nitrogen-boron collision case in 2500K.....	89
Figure 6-8. Grain growth at the interface of nitrogen-boron collision.	89
Figure 6-9. Statistics of change in kinetic energy from 100 collision cases in NVE 2500K.	91
Figure 6-10. Statistics of change in kinetic energy from BN collision cases in NVE 2500K.....	91
Figure 6-11. Statistics of change in kinetic energy from BB collision cases in NVE 2500K.....	91
Figure 6-12. Binding energies of B-N, B-B and N-N bonds.	92
Figure 6-13. Statistics of change in kinetic energy from 100 collision cases at each temperature.	93
Figure 6-14. Statistics of change in kinetic energy from BN collision cases at each temperature.	94
Figure 6-15. Statistics of change in kinetic energy from BB collision cases at each temperature.	94
Figure 6-16. Vertex-to-facet case at T=3100K.....	96

Figure 6-17. Initial configuration of NP2 with rotation along z-axis of 106° & along new x-axis of 73°	96
Figure 6-18. NVE simulation with initial temperature of 2500K for 50ns (a) 70ps (b) 3ns (c) 50ns (d) 50ns with surface presentation.	97
Figure 6-19. NVE simulation with initial temperature of 2700K for 50ns. (a) 70ps (b) 50ns with top view (c) 50ns with side view (d) 50ns side view with surface presentation.	98
Figure 6-20. NVE simulation with initial temperature of 2900K for 50ns. (a) 100ps (b) 38ns.	100
Figure 6-21. NVE simulation with initial temperature of 2900K for 50ns. (a) 38ns (b) 43ns (c) 45ns: the bond presentation on the left and atom presentation on the right (d) 48ns (e) 49ns (f) 50ns: phase separation taking place.	100
Figure 6-22. NVE simulation with initial temperature of 3100K for 50ns. (a) 100ps with T=3050K (b) 8ns with T=3125K (c) 12ns with T=3230K (d) 15ns with T=3320K.	102

Chapter 1

1. Introduction

1.1 Boron Nitride

The group III-V boron nitride compounds have an interesting history of discovery; they were first produced synthetically as a hexagonal layered structure in 1842¹, while the first naturally occurring boron nitride mineral, qingsongite, was actually discovered almost two centuries later in 2009 in Tibet and declared the zincblende crystalline structure in 2013². There are four different allotropes of boron nitride, namely hexagonal boron nitride (h-BN), rhombohedral boron nitride (r-BN), cubic boron nitride (c-BN), and wurtzite boron nitride (w-BN), as shown in Figure 1-1. Hexagonal-BN has a crystal structure similar to graphene, and is similarly formed from sp^2 bonds. It is also termed α -BN, or graphene-like BN (g-BN), and was first synthesized by Balmin¹ in 1842. The other sp^2 6-rings sheet structure is rhombohedral Boron Nitride (r-BN), which has the same bond length (1.44 Å) as h-BN, but with a different stacking sequence along the c-axis. The former has an *AaAa* stacking sequence, while the latter has an *ABCABC* stacking sequence. The zincblende (sphalerite) structure of BN analogous to carbon diamond with sp^3 bonding is cubic boron nitride (c-BN), which is also known as z-BN or β -BN. Wentorf³ first synthesized c-BN under high-pressure (85000 atmospheres) and high-temperature (1800°C) conditions in 1957, and the lattice constant of c-BN was measured to be 3.615 Å. The last crystalline phase of BN with also an sp^3 bonding structure is w-BN, also known as γ -BN. Both c-BN and w-BN have a bond length equal to 1.57Å, along with a tetrahedral structure; however, the angles between neighboring tetrahedrons and stacking sequence are different. Figure 1-2 shows the structural relations

among h-BN, w-BN, r-BN, and c-BN. There are also other sp^2 and sp^3 BN structures termed turbostratic BN (t-BN) and sp^3 -amorphous BN (a-BN) respectively. Gissler⁴ found that amorphous BN is formed from a mixture of h-BN and c-BN clusters. A detailed overview of boron nitride is presented in Mishima and Era⁵.

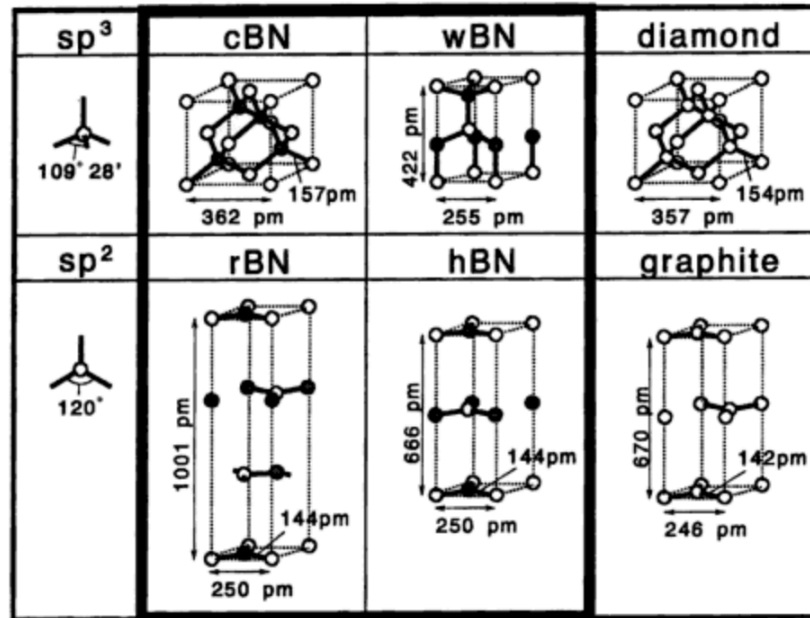


Figure 1-1 The four BN crystals (reproduced with caption from [4])

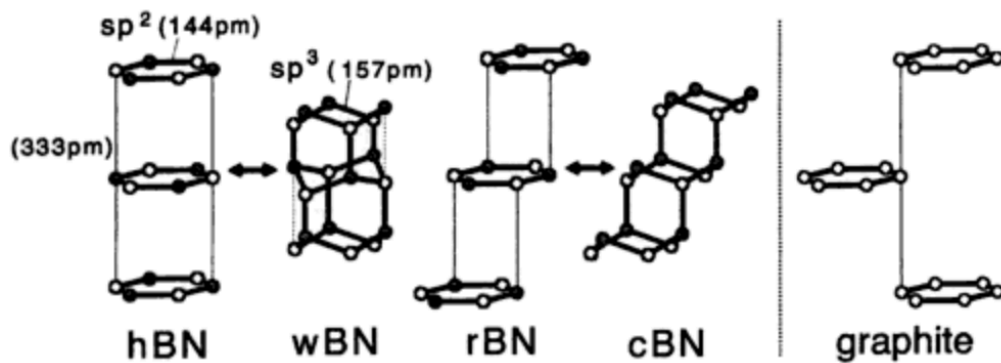


Figure 1-2 Structural relations among the four BN crystals (reproduced with caption from [4])

Cubic-BN is well known for its outstanding mechanical properties, thermal characteristics, and wide band gap structure⁶. Its superior hardness makes c-BN a commonly used material in tank armor, nuclear reactor coating, and industrial cutting and

grinding tools. It is considered as a replacement for synthetic carbon diamond because at high temperatures, diamond tends to react with some metals to form metal carbides, as well as graphitize, while c-BN is much less reactive and decomposes at a higher temperature ($\geq 2000\text{K}$). Since its hardness, with a Mohs scale of 9.5 – 10 or Vickers hardness of 48 – 100 GPa, is secondary only to diamond (Mohs scale of 10 or Vickers hardness of 115 GPa), c-BN makes it a great substitute for diamond in various mechanical and thermal applications. Moreover, c-BN has the widest band gap energy, approximately 6.3 eV, among all known semiconductors; hence, it has various potential electronic and electrical applications^{7, 8}. Cubic-BN can also be utilized as a heat sink substrate for Si-based electronic device because of its good thermal conductivity and similar thermal expansion coefficient to Si near room temperature⁵.

1.2 Motivation and Objectives

Commercial c-BN powders synthesized by high-pressure ($\leq 5\text{GPa}$) and high-temperature ($\geq 1500^\circ\text{C}$) processing usually consists of microparticles smaller than or around $500\mu\text{m}$, and a catalyst/solvent is typically used in the production. However, the rapid crystal growth of c-BN under high-pressure has been found to be the possible cause of defects such as fine cracks, solvent-trapped pools, and twins⁵. Alternatively, small sized c-BN nanocrystals ($< 100\text{nm}$) or thin films can be synthesized using low-pressure methods like chemical vapor deposition (CVD)⁹ and physical vapor deposition (PVD)¹⁰. The synthesis of c-BN nanopowders is challenging, and Prof. Tse's research group at Rutgers investigates thermal plasma aerosol synthesis to produce c-BN nanoparticles. In complement, this work, examines the fundamental processes of c-BN nanoparticle

formation, as well as the thermodynamic properties of c-BN nanoparticles at ambient pressure and in vacuum conditions, using molecular dynamics (MD) simulations. Specifically, the melting properties, particle-particle collision, and high temperature sintering of c-BN nanoparticles are studied. Insights into the geometric stability and melting mechanism of c-BN nanoparticles are gained. Furthermore, the size dependent melting of c-BN nanoparticles is also revealed. Finally, the particle-particle collision and sintering of c-BN nanoparticles at high temperature are also investigated, thereby providing a basic understanding of agglomeration processes involved during gas-phase synthesis.

1.3 Research Innovation and Strategies

The physical properties of c-BN have been intensively studied experimentally since 1957. Kleinman and Phillips¹¹ first studied the electronic properties and band structure of c-BN by in 1960. They found the energy gap of c-BN ($\sim 10\text{eV}$) to be about twice that of diamond. Since then, theoretical study of c-BN via first principle calculations has caught the interest of the community, and a diverse array of theoretical approaches have been employed, including Density functional theory (DFT) computations, molecular dynamics (MD) simulations, and analytical methods.. Zunger and Freeman¹² calculated the charge density of c-BN and found that c-BN bonding is not purely covalent, but has a low ionicity ($\text{B}^{0.35}\text{N}^{-0.35}$). Boron nitride, like other III-V materials has a shift in number of valence electrons that makes its properties differ from those of diamond, with c-BN found to have a mixed bonding of about 75% covalency and 25% ionicity¹³. The very first experimental and theoretical equation of state for c-BN was proposed by Knittle *et.*

*al.*¹⁴ in 1989, where they reported the the 300K equation of state of c-BN at very high pressure of 115 GPa, with the zero-pressure bulk modulus being measured to be 369 ± 14 GPa.

Sekkal *et. al.*¹⁵ were the first to propose a set of parameters for the empirical Tersoff potential in a molecular dynamics simulation for c-BN, and using which, they studied the structural and thermodynamic properties of c-BN in 1998. They used carbon's parameters as a starting point for fitting the potential parameters to structural properties of c-BN; and only the boron-nitrogen bond was considered, while neglecting both the Boron-Boron and Nitrogen-Nitrogen bonds. The linear and bulk thermal coefficients were determined to be $5.96 \times 10^{-6} \text{ K}^{-1}$ and $1.79 \times 10^{-5} \text{ K}^{-1}$, respectively. Furthermore, they studied liquid c-BN at high temperatures from 6000K to 8000K, but the melting point and melting mechanism were not discussed in their study. In the same year, Albe and Moller¹⁶ also proposed the parameters for a Tersoff-like potential for c-BN and carried out atomic-scale simulations of c-BN thin film growth. After that, several other groups have conducted molecular dynamics studies of c-BN bulk crystals and thin films¹⁷⁻²⁰. The structural, mechanical, and thermodynamic properties were reported in these studies, but none of them discussed the melting of c-BN bulk crystals. To our knowledge, a molecular dynamics study of c-BN nanoparticles is lacking in the field. Therefore, this is one of the first molecular dynamics investigations on c-BN nanoparticles, with focus on their melting and sintering properties.

We first investigate the potentials that have been used for c-BN bulk crystals and apply them to c-BN nanoparticles. Then, we test these potentials and find the best one for c-BN nanoparticles. Based on the empirical potential, the surface energy of $\{100\}$, $\{110\}$,

and $\{111\}$ facets is extracted; and the stabilities of various shapes of c-BN nanoparticles are analyzed. The geometric stability of c-BN nanoparticles is further investigated by observing the melting behavior of various shapes. Using the most stable c-BN nanoparticle shape, we investigate the melting mechanism by monitoring the Lindemann index, and also by utilizing the VMD visualization tool. In addition, the statistical study of particle-particle collision of c-BN nanoparticles with random initial orientations under high temperature is discussed. Collisions are examined for cases below the melting temperature, near the melting temperature, and above the melting temperature, allowing the determination of the optimal temperature for sintering with respect to the specific size of the c-BN nanoparticle.

1.4 Outline of This Dissertation

In Chapter 2, the various potentials used for c-BN are briefly introduced, and current research on melting and sintering of nanoparticles by MD simulation is also discussed. Chapter 3 describes the simulation method and analysis tools utilized in this study, with the comparison of various potentials applied to c-BN bulk crystals by MD simulation. Chapter 4 investigates the stability of single c-BN nanoparticles of various shapes. Chapter 5 studies the melting mechanism and size effects on the melting point and behavior of c-BN octahedral nanoparticles. In addition, models of melting point depression with size are also discussed and compared with our MD results. Chapter 6 examines particle-particle collision and sintering of c-BN nanoparticles. Finally, Chapter 7 concludes this thesis and remarks on the important results, as well as future research directions.

1.5 References

1. Balmain W. Bemerkungen über die bildung von verbindungen des bors und siliciums mit stickstoff und gewissen metallen. *Journal für Praktische Chemie*. 1842;27(1):422-430.
2. Dobrzhinetskaya LF, Wirth R, Yang J, et al. Qingsongite, natural cubic boron nitride: The first boron mineral from the earth's mantle. *Am Mineral*. 2014;99(4):764-772.
3. Wentorf Jr R. Cubic form of boron nitride. *J Chem Phys*. 1957;26(4):956-956.
4. Gissler W, Haupt J, Hoffmann A, Gibson P, Rickerby D. Mixed phase nanocrystalline boron nitride films: Preparation and characterization. *Thin Solid Films*. 1991;199(1):113-122.
5. Mishima O, Era K. Science and technology of boron nitride. *Electric Refractory Materials*. 2000:495-556.
6. Mirkarimi P, McCarty K, Medlin D. Review of advances in cubic boron nitride film synthesis. *Materials Science and Engineering: R: Reports*. 1997;21(2):47-100.
7. Wentorf Jr R. Preparation of semiconducting cubic boron nitride. *J Chem Phys*. 1962;36(8):1990-1991.
8. Mishima O, Tanaka J, Yamaoka S, Fukunaga O. High-temperature cubic boron nitride p-N junction diode made at high pressure. *Science*. 1987;238(4824):181-183.
9. Saitoh H, Yarbrough WA. Preparation and characterization of nanocrystalline cubic boron nitride by microwave plasma-enhanced chemical vapor deposition. *Appl Phys Lett*. 1991;58(20):2228-2230.
10. Ikeda T. Cubic boron nitride films synthesized by low-energy ion-beam-enhanced vapor deposition. *Appl Phys Lett*. 1992;61(7):786-788.
11. Kleinman L, Phillips JC. Crystal potential and energy bands of semiconductors. II. self-consistent calculations for cubic boron nitride. *Physical Review*. 1960;117(2):460.
12. Zunger A, Freeman A. Ab initio self-consistent study of the electronic structure and properties of cubic boron nitride. *Physical Review B*. 1978;17(4):2030.
13. Heimann RB. Non-oxide ceramics: Structure, technology, and applications. In: *Classic and advanced ceramics: From fundamentals to applications*. WILEY; 2010:446.
14. Knittle E, Wentzcovitch RM, Jeanloz R, Cohen ML. Experimental and theoretical equation of state of cubic boron nitride. *Nature*. 1989;337(6205):349-352.

15. Sekkal W, Bouhafs B, Aourag H, Certier M. Molecular-dynamics simulation of structural and thermodynamic properties of boron nitride. *Journal of Physics: Condensed Matter*. 1998;10(23):4975.
16. Albe K, Möller W. Modelling of boron nitride: Atomic scale simulations on thin film growth. *Computational Materials Science*. 1998;10(1):111-115.
17. Matsunaga K, Fisher C, Matsubara H. Tersoff potential parameters for simulating cubic boron carbonitrides. *Japanese Journal of Applied Physics*. 2000;39(1A):L48.
18. Moon WH, Son MS, Hwang HJ. Molecular-dynamics simulation of structural properties of cubic boron nitride. *Physica B: Condensed Matter*. 2003;336(3):329-334.
19. Moon WH, Hwang HJ. A modified Stillinger–Weber empirical potential for boron nitride. *Appl Surf Sci*. 2005;239(3):376-380.
20. Koga H, Nakamura Y, Watanabe S, Yoshida T. Molecular dynamics study of deposition mechanism of cubic boron nitride. *Science and Technology of Advanced Materials*. 2001;2(2):349-356.

Chapter 2

2 Literature Review

2.1 Introduction of Potentials

Molecular dynamics simulation is a method of particle tracking by using classical mechanics, where the positions and velocities of atoms in a system are derived from the interatomic force that is defined by the potential energy (see Equation 2-1). Therefore, it is essential and important to have an appropriate interatomic potential for molecular dynamics simulation. Nowadays, there are three major many-body potentials used for MD simulation of c-BN, and the following sections describe each of them. The simulation work of c-BN crystals are introduced in each section as well.

Equation 2-1: $\frac{dr_i}{dt} = v_i, \frac{d}{dt}(m_i v_i) = F_i = -\nabla_i V = -\nabla_i [\sum_j V_2(r_i, r_j) + \sum_{j,k} V_3(r_i, r_j, r_k)]$

2.1.1 Tersoff Potential

In the early stages of MD simulation, there were two pair potentials commonly used to describe the interatomic attractive and repulsive forces as a function of pair distance (r). The first is the Lennard-Jones “6-12” potential, as shown in Equation 2-2, which was proposed, and best suited for, describing the van der Waals forces between non-bonding particles. The van der Waals forces included dipole-dipole interaction, dipole-induced interactions, and instantaneously induced dipole interactions (London forces). Here, ϵ is the strength of the potential well; σ is the van der Waals radius (i.e. where the inter-particle potential is equal to zero and is the nearest distance non-bonding particles can approach each other); and r_m is the distance at which the potential reaches its minima (i.e. the equilibrium distance of a pair). The other potential, which was proposed to describe the inter-atomic potential energy of a diatomic molecule, is the exponential Morse

potential, as shown in Equation 2-3. D_e is the well depth; K_e is the force constant at the energy minimum; and r_e is the distance that potential reaches its minimum. These pair potentials are applicable to systems with completely arbitrary configurations of atoms, but neither of them is applicable to strongly covalent bonding systems. Therefore, Jerry Tersoff proposed a new empirical approach to study the structure and energy of covalent systems¹⁻³. The multicomponent Tersoff potential is shown in Equation 2-4, which includes considerations of both distance and bond angle between the particles for determining the inter-atomic potential. More details can be found in Ref.³.

$$\text{Equation 2-2: } V_{LJ}(r) = 4\varepsilon \left[\left(\frac{\sigma}{r} \right)^{12} - \left(\frac{\sigma}{r} \right)^6 \right] = \varepsilon \left[\left(\frac{r_m}{r} \right)^{12} - 2 \left(\frac{r_m}{r} \right)^6 \right]$$

$$\text{Equation 2-3: } V(r) = D_e [e^{-2a(r-r_e)} - 2e^{-a(r-r_e)}], a = \sqrt{K_e/2D_e}$$

$$\text{Equation 2-4: } V_{ij} = f_c(r_{ij})[f_R(r_{ij}) - b_{ij}f_A(r_{ij})]$$

$$f_R(r_{ij}) = A_{ij} \exp(-\lambda_{ij}r_{ij}), f_A(r_{ij}) = -B_{ij} \exp(-\mu_{ij}r_{ij})$$

$$f_c(r_{ij}) = \begin{cases} 1, r_{ij} < R_{ij} \\ \frac{1}{2} + \frac{1}{2} \cos \left[\frac{\pi(r_{ij} - R_{ij})}{(S_{ij} - R_{ij})} \right], R_{ij} < r_{ij} < S_{ij} \\ 0, r_{ij} > S_{ij} \end{cases}$$

$$b_{ij} = \chi_{ij}(1 + \beta_i^{n_i} \zeta_{ij}^{n_i})^{-1/2n_i}, \zeta_{ij} = \sum_{k \neq i,j} f_c(r_{ik})g(\theta_{ijk})$$

$$g(\theta_{ijk}) = 1 + \frac{c_i^2}{d_i^2} - \frac{c_i^2}{d_i^2 + (h_i - \cos \theta_{ijk})^2}$$

$$\lambda_{ij} = \frac{(\lambda_i + \lambda_j)}{2}, \mu_{ij} = \frac{(\mu_j + \mu_i)}{2}, A_{ij} = (A_i A_j)^{1/2}, B_{ij} = (B_i B_j)^{1/2}$$

$$R_{ij} = (R_i R_j)^{1/2}, S_{ij} = (S_i S_j)^{1/2}$$

A decade after the Tersoff potential was developed, Sekkal et al.⁴ first treated BN as a single component system, using the Tersoff parameters² for carbon as the starting point for fitting the potential parameters to the structural properties of BN. They

calculated a lattice constant of 3.623Å; and the cohesive energy, bulk modulus, and thermal expansion of c-BN were extracted from the simulations using the Tersoff potential. In 2000, Matsunaga et al.⁵ then proposed a set of Tersoff potential parameters for c-BN and cubic boron carbon nitrides, but the lattice constant of 3.658Å that they obtained was slightly larger than the experimental value⁶ of 3.615Å. Moon et al.⁷ took the Tersoff parameters of nitrogen from silicon nitride^{8,9} and developed another set of parameters of boron to fit to c-BN to study the structural properties of c-BN. They calculated a lattice constant of 3.609Å and a cohesive energy of -6.58eV, as compared to the experimental values of 3.615Å and -6.60eV, respectively. In addition, they also used the Tersoff-like potential to investigate the optimized geometry and thermal behavior of BN nanotubes¹⁰.

2.1.2 Albe Potential

In the same year that the Tersoff potential was first applied to model c-BN by Sekkal⁴, Albe and Moller¹¹ also proposed a Tersoff-like potential for the simulation of c-BN thin film growth. The potential is still based on the Tersoff structure, but the repulsive and attractive force terms are similar to the Morse potential as proposed by Brenner¹². This integrated potential is the so-called Albe potential, as given in Equation 2-5. They have observed the sp²-bonded and sp³-bonded phases of BN growth in MD simulations. Using the same potential, Koga et al.¹³ simulated the deposition of c-BN, as well as the conversion of g-BN into c-BN.

Equation 2-5: $V_{ij} = f_c(r_{ij})[f_R(r_{ij}) - b_{ij}f_A(r_{ij})]$

$$f_R(r_{ij}) = \frac{D_0}{S-1} \exp\left(-\beta\sqrt{2S}(r_{ij} - r_0)\right)$$

$$f_A(r_{ij}) = \frac{SD_0}{S-1} \exp\left(-\beta\sqrt{2/S}(r_{ij} - r_0)\right)$$

$$f_c(r_{ij}) = \begin{cases} 1, r_{ij} < R - D \\ \frac{1}{2} - \frac{1}{2} \sin \left[\frac{\pi(r_{ij} - R)}{2D} \right], |R - r| \leq D \\ 0, r_{ij} \geq R + D \end{cases}$$

$$b_{ij} = (1 + \gamma^n \chi_{ij}^n)^{-1/2n}$$

$$\chi_{ij} = \sum_{k \neq i, j} f_c(r_{ik}) g(\theta_{ijk}) \exp [\lambda_3^3 (r_{ij} - r_{ik})^3]$$

$$g_{ijk}(\theta) = 1 + \frac{c^2}{d^2} - \frac{c^2}{d^2 + (h - \cos \theta_{ijk})^2}$$

2.1.3 Stillinger-Weber Potential

The Stillinger-Weber (SW) potential, as presented in Equation 2-6, is another widely used potential for the computational study of covalent bonding systems. This potential was proposed by Stillinger and Weber¹⁴ in 1985 to simulate the tetrahedral semiconductor – silicon. The molten state of Si was also studied using this potential. A comparative study of the Tersoff potential versus the SW potential on simulating the surface reconstruction of the Si {100} surface was reported, and the SW potential was found to perform better¹⁵. Moon and Hwang¹⁶ modified the two-body force term of the SW potential, given in Equation 2-7, and fit the parameters for BN to study the structural properties and elastic constants of c-BN and w-BN, as well as the thermodynamic properties of c-BN. The lattice constant found in their study is 3.6078Å, slightly lower than the experimental value of 3.615Å, resulting in a lower cohesive energy of -6.718eV. In addition, the Debye temperature of c-BN was calculated to be 1744K, and the linear thermal expansion was found to be $5.47 \times 10^{-6} \text{ K}^{-1}$, compared with the experimental values of 1700K and $6 \times 10^{-6} \text{ K}^{-1}$ to $8 \times 10^{-6} \text{ K}^{-1}$, respectively. In addition, they also applied the modified SW potential to investigate the structural property of BN fullerenes¹⁷. In general, the SW potential is

extensively used for MD simulations of many materials, including carbon¹⁸⁻²⁰, GaN²¹, and Si & O mixed systems²².

Equation 2-6: $V_2(r_{ij}) = \epsilon f_2(r_{ij}/\sigma)$, $V_3(r_i, r_j, r_k) = \epsilon f_3(r_i/\sigma, r_j/\sigma, r_k/\sigma)$

$$f_2(r) = \begin{cases} A(Br^{-p} - r^{-q}) \exp[(r - a)^{-1}], & r < a \\ 0, & r \geq a \end{cases}$$

$$f_3(r_i, r_j, r_k) = h(r_{ij}, r_{ik}, \theta_{jik}) + h(r_{ji}, r_{jk}, \theta_{ijk}) + h(r_{ki}, r_{kj}, \theta_{ikj})$$

$$h(r_{ij}, r_{ik}, \theta_{jik}) = \lambda \exp[\gamma(r_{ij} - a)^{-1} + \gamma(r_{ik} - a)^{-1}] \times (\cos\theta_{jik} + \cos\theta_t)^2$$

Equation 2-7: $f_2(r) = \begin{cases} A(Br^{-p} - r^{-q}) \exp\left[\frac{\delta}{r-a}\right], & r < a \\ 0, & r \geq a \end{cases}$

Out of the above three potentials widely used for simulating covalent systems, we choose to use the modified SW potential in this study of c-BN nanoparticles. A detailed comparison between the potentials applied to c-BN will be presented in Chapter 3, and the rationale for choosing the SW potential will be discussed.

2.2 Phase Stability of Nanoparticles

The geometry of nanoparticles plays an important role in affecting their chemical, optical, electronic, and thermodynamic properties; thus it also contributes to their phase stability²³. The shape evolution with particle size has caught the attention of theorists, and Barnard²⁴⁻²⁷ has carried out thorough studies of the phase stability of nanoparticles as a function of size and shape. Here, we review the phase stability of diamond structured (cubic phase in single elemental systems) and zincblende/sphalerite (cubic phase in binary systems) structured materials.

2.2.1 Diamond Structured Materials

Winter and Ree²⁸ proposed the phase stability for carbon graphite and atomic diamond clusters as a function of size via first-principle and semi-empirical molecular orbital calculations. C₁₀, C₃₅, C₁₀, C₈₄, and C₁₆₅ carbon clusters were discussed in their study, and they calculated the cohesive energies of the different clusters. They also mentioned the structural effects of surface bonding, and found that the capping of surface dangling bonds by hydrogen helps to stabilize sp² and sp³ bonding. Barnard et al.²⁹ determined the heat of formation in order to estimate the phase stability of nanodiamond clusters and fullerenes. They found that fullerenes are the most stable form of carbon for small clusters, and that diamond is stable in the range of 1.9 nm to approximately 5.2 nm, beyond which graphite is most stable. In addition, Barnard and Zapol²⁴ developed a thermodynamic model for calculating the Gibbs free energy that includes bulk, surface, edge, and corners energies for arbitrary nanoparticles. The phase stability results of both dehydrogenated and hydrogenated diamond-structured C, Si, and Ge nanoparticles from their study are shown in Figure 2-1 and Figure 2-2, respectively. For nanoparticles containing more than ten thousand atoms, the relative stability of the different shapes of both dehydrogenated and hydrogenated diamond-structured C, Si, and Ge nanoparticles are shown in Figure 2-3.

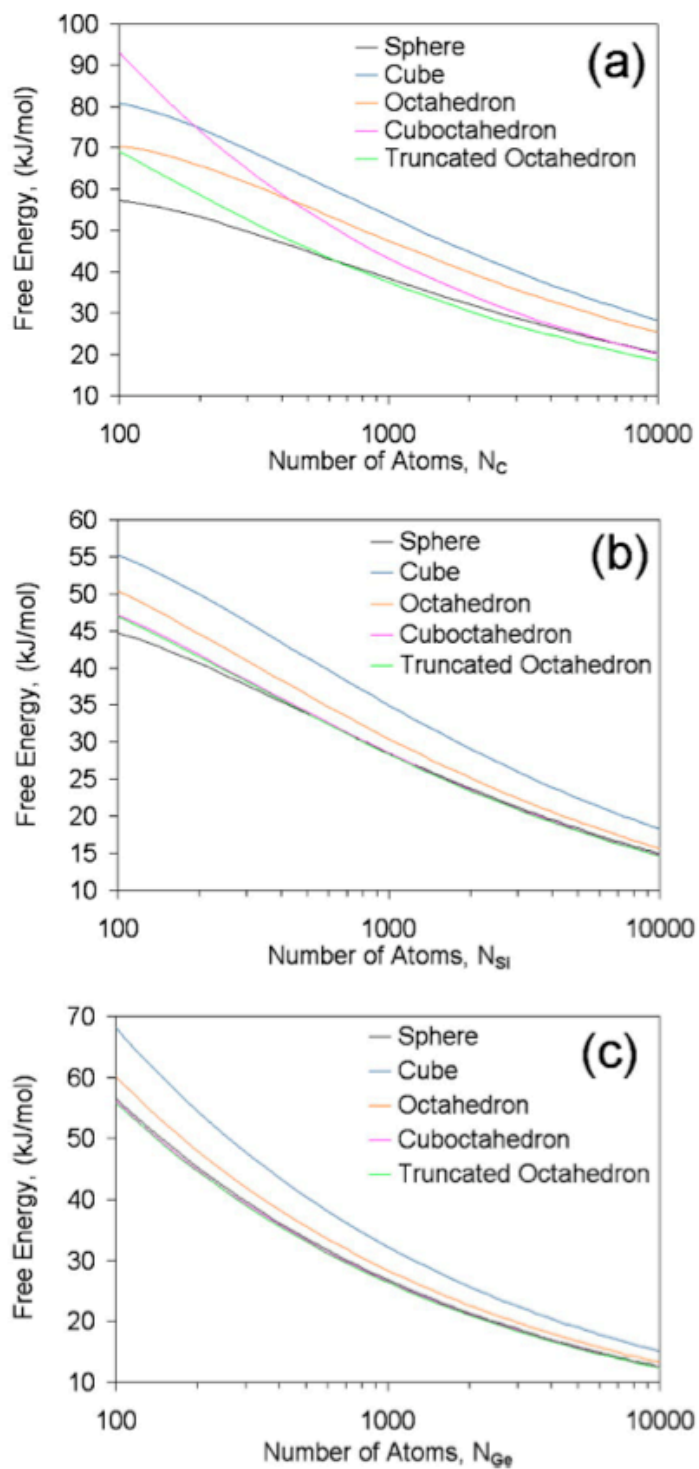


Figure 2-1 Phase stability of dehydrogenated diamond-structured (a) C (1.2 – 5.6 nm), (b) Si (1.6 – 7.3 nm), and (c) Ge (1.7 – 7.6 nm) nanoparticles (reproduced from [24])

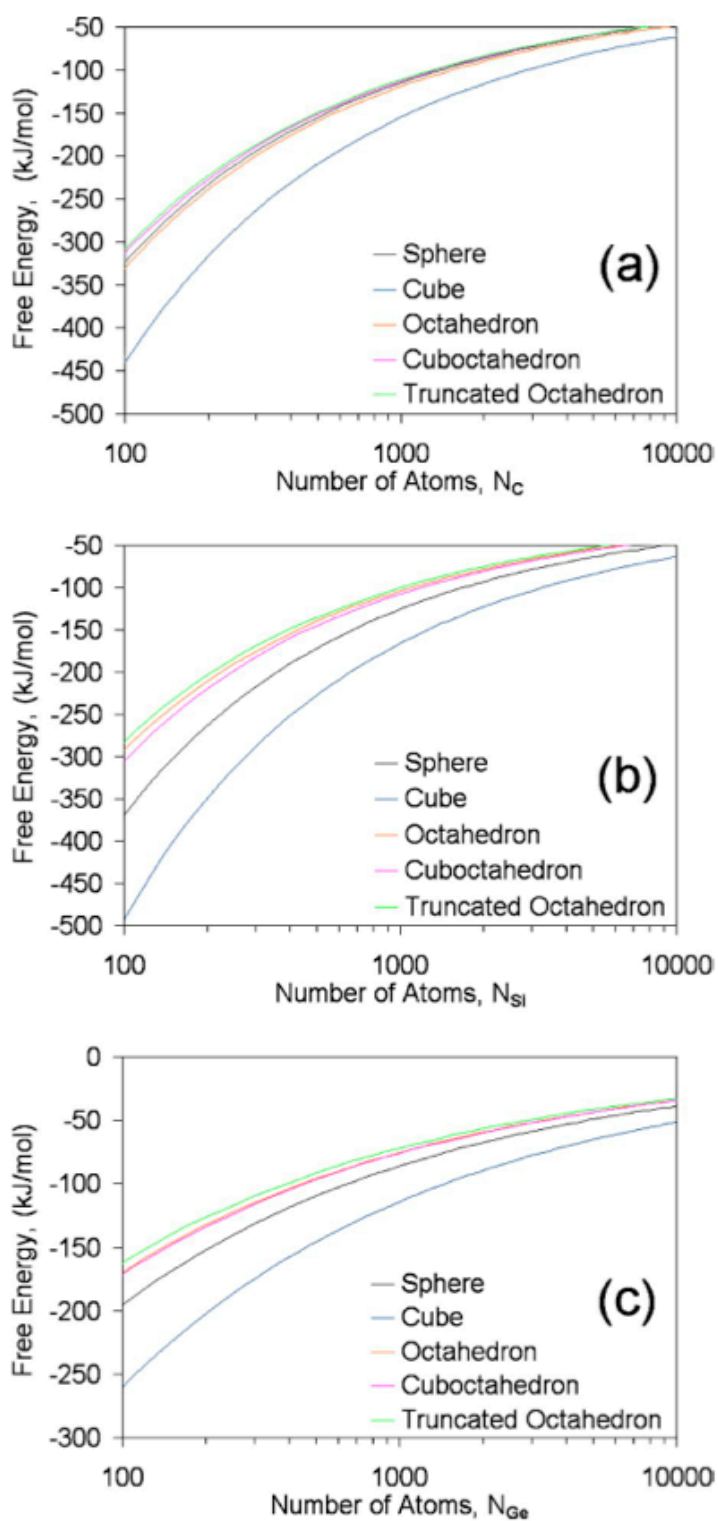


Figure 2-2 Phase stability of hydrogenated diamond-structured (a) C (1.2 – 5.6 nm), (b) Si (1.6 – 7.3 nm), and (c) Ge (1.7 – 7.6 nm) nanoparticles (reproduced from [24])

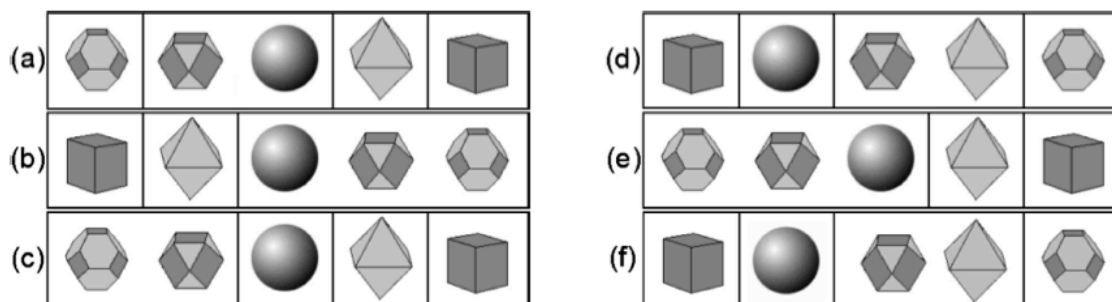


Figure 2-3 The preferred shapes (left to right) of dehydrogenated diamond-structured (a) C, (b) Si, and (c) Ge, and dehydrogenated diamond-structured (d) C, (e) Si, and (f) Ge nanoparticles of ≥ 10000 atoms. Energetically undistinguishable shapes are not separated by a line (reproduced from [24])

2.2.2 Zincblende Structured Materials

For binary covalent systems, there are many MD studies discussing the phase stability of nanoparticles. Zhang et. al.³⁰ carried out a comprehensive study of the phase stability of ZnS nanoparticles both theoretically and experimentally. They examined two phases of ZnS, i.e. zincblende and wurtzite, and found that the smaller wurtzite ZnS nanoparticles are thermodynamically more stable than the zincblende ZnS nanoparticles. This stability is also observed through the MD simulation of a 3 nm ZnS particle transforming from zincblende to wurtzite structure. However, water adsorption onto ZnS nanoparticles makes the zincblende structure more stable than wurtzite structure. In addition, Wright and Gale³¹ have also developed a new interatomic potential that includes the four-body contribution to the energy for simulating the zincblende and wurtzite forms of ZnS and CdS. They predicted that the cubic polytype is the most favorable structure for ZnS, and that the hexagonal phase is the most stable for CdS. The structural attributes, elastic properties, and the defect formation energies of both materials were also presented in their study.

Wang and Ye³² used first-principles calculation to study III-V compounds and presented the phase stability and elastic properties of zincblende (ZB) and wurtzite (WZ) structures. As shown in Figure 2-4, BN is more stable in the zincblende structure, with a difference in ground state energy of $\Delta E_{WZ-ZB} \approx 35$ meV, with respect to wurtzite structure.

However, a study of the relative stability of different shapes of c-BN nanoparticles is lacking in the community; hence, we propose and conduct MD simulations of c-BN nanoparticles of varying shapes, with the results discussed in Chapter 4.

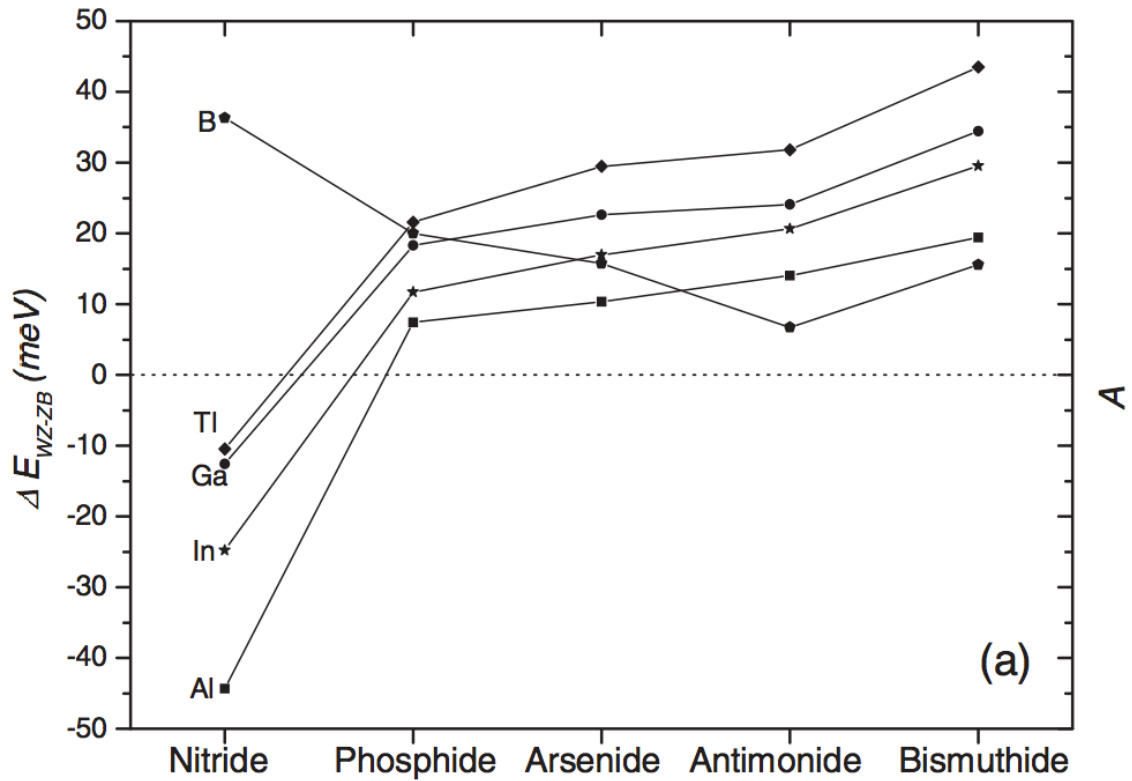


Figure 2-4 Phase stability of III-V compounds. AlN, InN, GaN, and TiN are more stable in the WZ structure for $\Delta E_{WZ-ZB} < 0$ (reproduced from [32])

2.3 Melting of Nanoparticles

The melting of nanoparticles differs from that of its bulk in several key aspects³³. First, the melting point is lowered, with a complex dependence on size, which is known as melting-point depression. Four major mechanisms have been proposed for predicting the melting point of small clusters, i.e. liquid drop model, liquid shell nucleation model, liquid nucleation and growth model, and bond-order-length-strength (BOLS) model. The BOLS model is based on the cohesive energy of individual atoms (instead of a classic thermodynamic approach), which is more suitable for our c-BN nanoparticles. Furthermore, the solid-liquid phase transition in nanoparticles does not occur sharply at one temperature but rather smoothly over a finite temperature range, because of finite size effects. The pre-melting phenomena³⁴ depends crucially on materials and cluster structures properties. It is termed surface melting³⁵ if the melting first takes place on the surface atoms, leading to a core-shell structure for the nanoparticles³⁶.

Most models of melting-point depression for freestanding nanoparticles use the linear relation between the melting point of the nanoparticle (T_{mp}) and the bulk melting temperature (T_{mb}), as shown in Equation 2-8. However, this linear relation might fail for nanoparticles of very small sizes. Therefore, in the following sections, we discuss several models that are not based upon this linear relationship, and which might be capable of predicting the melting points of our c-BN nanoparticles

Equation 2-8: $\frac{T_{mp}}{T_{mb}} = 1 - \frac{K}{D}$, *D: nanoparticle diameter, K: modeling constant*

2.3.1 Cohesive Energy & Average Coordination Number

The cohesive energy of a nanoparticle is the energy required to separate it apart into individual atoms. The surface atoms of nanoparticles have a lower coordination number

compared with the internal atoms or with bulk crystals, resulting in a lower binding energy for the surface atoms. Therefore, the cohesive energy per atom of a nanoparticle is expected to be smaller than that of bulk crystals, with Equation 2-9 displaying the relation³⁷. The cohesive energy directly affects the melting temperature as revealed in Nanda's study³⁸, which is based on Lindemann's criterion of melting. Shandiz et. al.³⁹ calculated the relation between cohesive energy and average coordination number for nanoparticles and bulk crystals. In doing so, they derived a relation between the ratio of the coordination number of a nanoparticle to that of the bulk crystal, and the ratio of the melting temperature of the nanoparticle and that of the bulk crystal, as given in Equation 2-10. Moreover, Safaei et. al.⁴⁰ calculated the surface-to-volume coordination number by considering the surface packing (Figure 2-5), thereby obtaining an expression for the melting limit of nanoparticles, as given in Equation 2-11. However, a key assumption in their study is that there are no surface reconstruction and relaxation, which as we will show, are crucial to understanding the melting mechanism for c-BN nanoparticles.

Equation 2-9: $E_p = E_b \left(1 - \frac{d}{D}\right)$, D : *nanoparticle diameter*, d : *atomic diameter*

Equation 2-10: $\frac{E_p}{E_b} = \frac{T_{mp}}{T_{mb}} = \frac{Z_{lp}}{Z_{lb}} \left(1 - 2(1 - q) \frac{D_0}{D + D_0}\right)$

Equation 2-11: $\frac{T_{mp}}{T_{mb}} = 1 - (1 - q) \frac{n_s}{n_t}$, q : *surface – to – volume coordinaton number*

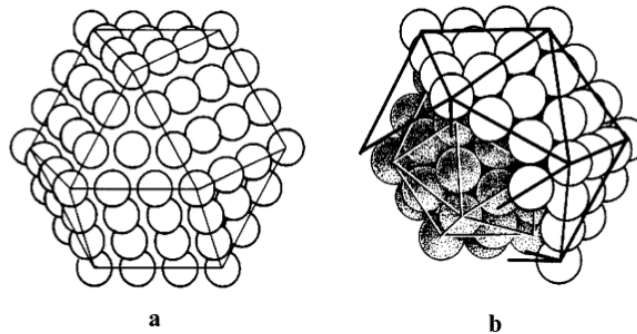


Figure 2-5 (a) Closed-shell 147 atom cuboctahedron (b) Closed-shell 55 atom icosahedron (shaded) and a portion of the next shell (reproduced from [40])

2.3.2 Geometry Factor

Following the pioneering work of Pawlow in 1909⁴¹, most thermodynamic approaches of melting-point depression have assumed the nanoparticle to be spherical. However, the nanoparticle's shape and size plays an important role in its chemical and thermodynamic properties, especially with faceting like c-BN. Wautelet et al.⁴² proposed a model that is also based upon the basic idea of surface-to-volume ratio, but attempts to capture the difference between different geometric shapes by calculating the surface-to-volume ratio of spherical and non-spherical nanoparticles. Equation 2-12 shows the relationship that they obtained for the melting temperature of nanoparticles of various shapes to the bulk melting temperature, along with the geometric constants for all the different shapes, as listed in Figure 2-6.

In this thesis, the cohesive energy/coordination number, as well as the geometric-shape dependence of c-BN nanoparticle melting temperatures, is studied. Both factors play key roles in the melting mechanism of c-BN nanoparticles. Additionally, size effects on melting point will be also discussed in Chapter 5.

Equation 2-12: $T_{mp} = T_{mb} \left(1 - D \frac{A}{V} \right), \frac{A}{V} = \frac{\beta(shape)}{V^{1/3}}, D: \text{material constant}$

Shape	β	Remarks
Sphere	4.836	
Cube	6	
Octahedron	5.719	
Icosahedron	5.149	
Spheroids (oblate)	$\pi^{1/3} [3(1 - \varepsilon^2)/4]^{2/3} \times \{2(1 - \varepsilon^2)^{-1} + \varepsilon^{-1} \ln[(1 + \varepsilon)/(1 - \varepsilon)]\}$	$\varepsilon = \sqrt{1 - (b/a)^2}$
Spheroids (prolate)	$(\pi/2)^{1/3} [3/(1 - \varepsilon^2)]^{2/3} \times \{(1 - \varepsilon^2) + \varepsilon^{-1} (1 - \varepsilon^2)^{1/2} \arcsin \varepsilon\}$	$\varepsilon = \sqrt{1 - (b/a)^2}$
Drop on a flat substrate	$\pi^{1/2} 3^{2/3} [2(1 - \cos \theta) + \sin^2 \theta] / [2(1 - \cos \theta) - \sin^2 \theta \cos \theta]^{2/3}$	$\theta = \text{contact angle}$ $r = \text{radius of the contact surface}$ $R = \text{radius of the sphere}$ $h = R(1 - \cos \theta); r = R \sin \theta$

Figure 2-6 Parameter β for various geometric shapes (reproduced from [42])

2.4 Sintering of Nanoparticles

In the vapor-phase particle growth process, the rate of particle coalescence is an important factor affecting the final morphology of the particles. Zachariah and Carrier⁴³ studied the kinetics of particle coalescence and revealed that particles agglomerate if the sintering time is longer than the collision time, as displayed in Figure 2-7. In liquid-phase growth, the sintering process is governed primarily by viscous flow because of the amorphous nature of the materials. Cushing et al.⁴⁴ comprehensively investigated liquid-phase synthesis and sintering of inorganic nanoparticles. In solid-phase growth, there are six distinct mechanisms contributing to the sintering of crystalline particles, namely, surface diffusion, lattice diffusion from the surface, vapor transport, grain boundary diffusion, lattice diffusion from the grain boundary, and lattice diffusion through dislocation. Zeng et al.⁴⁵ employed MD simulations to examine the sintering of Cu nanofibers, and observed that surface diffusion and grain boundary diffusion are the most significant transport processes in initially aligned nanofibers of the same size (Figure 2-8), and also of different sizes (Figure 2-10). Neck growth is clearly seen in the sintering of unequal sized Cu nanofibers. They also simulated two randomly oriented Cu nanofibers, with the smaller nanofiber one quarter the size of the larger nanofiber, finding that the smaller nanofiber is first amorphized, and then merged into the larger particle and recrystallized (Figure 2-10).

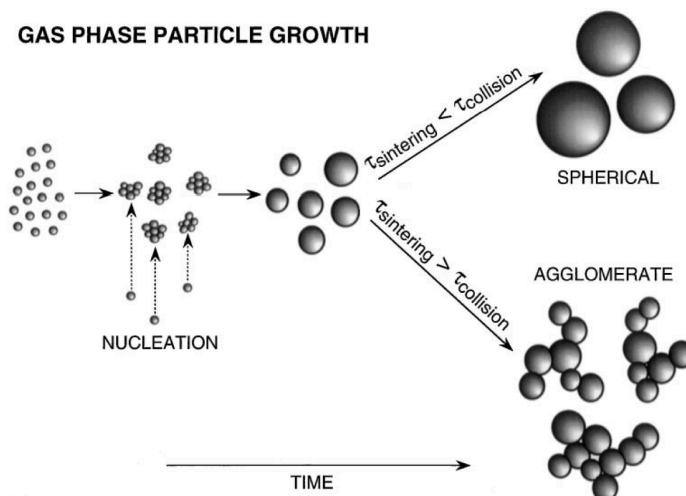


Figure 2-7 Temporal evolution of vapor-phase particle growth (reproduced with caption from [45])

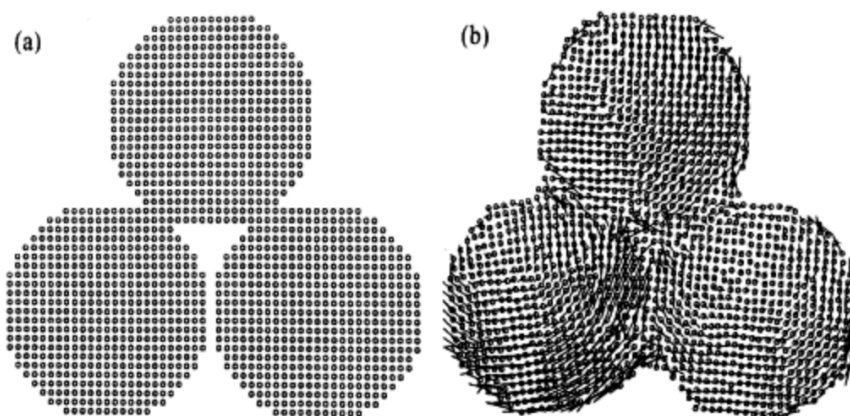


Figure 2-8 (a) Initial position of three exactly aligned Cu nanofibers (4.4 nm diameter) (b) position after sintering at 1000K for 34 ps (reproduced with caption from [45])

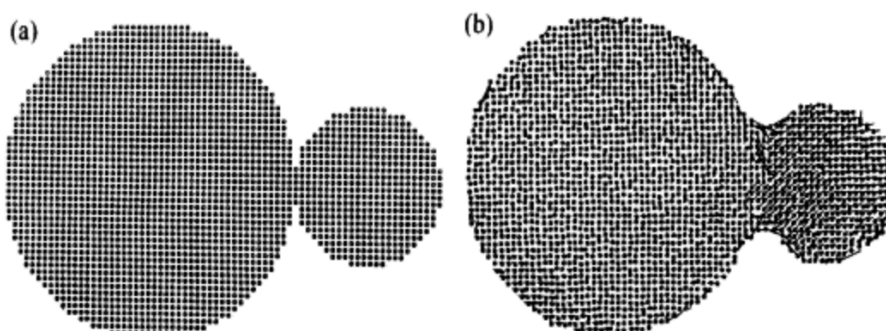


Figure 2-9 (a) Initial position of two exactly aligned Cu nanofibers (8.8 nm and 4.4 nm) (b) position after sintering at 1000K for 34 ps (reproduced with caption from [45])

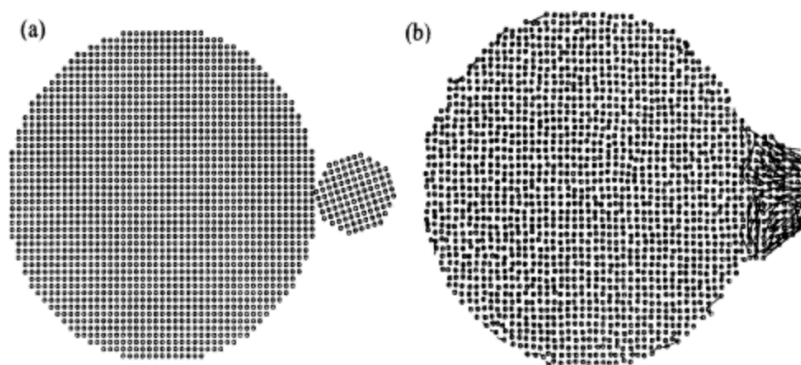


Figure 2-10 (a) Initial position of two randomly oriented Cu nanofibers (8.8 nm and 2.2 nm) (b) position after sintering at 1000K for 32 ps (reproduced with caption from [45])

The process of diffusion is extremely sensitive to temperature, and the rise of temperature after particle-particle collision can consequently cause the melting of nanoparticles. Thus, accurately knowing the melting point of nanoparticles is essential for understanding the sintering of nanoparticles. Koparade and Cummings⁴⁶ simulated titanium dioxide nanoparticles using MD, scrutinizing the melting points of varying-sized titanium dioxide nanoparticles. They also calculated the ionic diffusivities of titanium dioxide nanoparticles of different crystalline structures, and employed a simulated x-ray diffraction analysis to assess phase transition. They successfully observed a rutile-anaphase phase transition during sintering of titania nanoparticles⁴⁷, which is a remarkable finding within a molecular dynamics simulation approach.

Apart from the sintering of spherical nanoparticles, Alimohammadi and Fichthorn⁴⁸ have conducted an aggregation study of faceted TiO₂ nanoparticles by MD simulations and found that the electrostatic interactions between under-coordinated Ti and O surface atoms drive the aggregation from the statistical result of particle-particle collisions. The simulation condition for the sintering environment of our c-BN nanoparticles is very similar to their study, which will be discussed in Chapter 6.

2.5 References

1. Tersoff J. New empirical approach for the structure and energy of covalent systems. *Physical Review B*. 1988;37(12):6991.
2. Tersoff J. Empirical interatomic potential for carbon, with applications to amorphous carbon. *Phys Rev Lett*. 1988;61(25):2879.
3. Tersoff J. Modeling solid-state chemistry: Interatomic potentials for multicomponent systems. *Physical Review B*. 1989;39(8):5566.
4. Sekkal W, Bouhafs B, Aourag H, Certier M. Molecular-dynamics simulation of structural and thermodynamic properties of boron nitride. *Journal of Physics: Condensed Matter*. 1998;10(23):4975.
5. Matsunaga K, Fisher C, Matsubara H. Tersoff potential parameters for simulating cubic boron carbonitrides. *Japanese Journal of Applied Physics*. 2000;39(1A):L48.
6. Knittle E, Wentzcovitch RM, Jeanloz R, Cohen ML. Experimental and theoretical equation of state of cubic boron nitride. *Nature*. 1989;337(6205):349-352.
7. Moon WH, Son MS, Hwang HJ. Molecular-dynamics simulation of structural properties of cubic boron nitride. *Physica B: Condensed Matter*. 2003;336(3):329-334.
8. de Brito Mota F, Justo J, Fazzio A. Structural and electronic properties of silicon nitride materials. *International journal of quantum chemistry*. 1998;70(4-5):973-980.
9. de Brito Mota F, Justo J, Fazzio A. Structural properties of amorphous silicon nitride. *Physical Review B*. 1998;58(13):8323.
10. Moon WH, Hwang HJ. Molecular-dynamics simulation of structure and thermal behaviour of boron nitride nanotubes. *Nanotechnology*. 2004;15(5):431.
11. Albe K, Möller W. Modelling of boron nitride: Atomic scale simulations on thin film growth. *Computational Materials Science*. 1998;10(1):111-115.
12. Brenner DW. Empirical potential for hydrocarbons for use in simulating the chemical vapor deposition of diamond films. *Physical Review B*. 1990;42(15):9458.
13. Koga H, Nakamura Y, Watanabe S, Yoshida T. Molecular dynamics study of deposition mechanism of cubic boron nitride. *Science and Technology of Advanced Materials*. 2001;2(2):349-356.
14. Stillinger FH, Weber TA. Computer simulation of local order in condensed phases of silicon. *Physical review B*. 1985;31(8):5262.

15. Nurminen L, Tavazza F, Landau DP, Kuronen A, Kaski K. Comparative study of si (001) surface structure and interatomic potentials in finite-temperature simulations. *Physical Review B*. 2003;67(3):035405.
16. Moon WH, Hwang HJ. A modified Stillinger–Weber empirical potential for boron nitride. *Appl Surf Sci*. 2005;239(3):376-380.
17. Moon WH, Son MS, Hwang HJ. Theoretical study on structure of boron nitride fullerenes. *Appl Surf Sci*. 2007;253(17):7078-7081.
18. Barnard A, Russo S. Development of an improved stillinger-weber potential for tetrahedral carbon using ab initio (hartree-fock and MP2) methods. *Mol Phys*. 2002;100(10):1517-1525.
19. Marks N, McKenzie D, Pailthorpe B. Molecular-dynamics study of compressive stress generation. *Physical Review B*. 1996;53(7):4117.
20. Pailthorpe B. Molecular-dynamics simulations of atomic processes at the low-temperature diamond (111) surface. *J Appl Phys*. 1991;70(2):543-547.
21. Aichoune N, Potin V, Ruterana P, Hairie A, Nouet G, Paumier E. An empirical potential for the calculation of the atomic structure of extended defects in wurtzite GaN. *Computational materials science*. 2000;17(2):380-383.
22. Watanabe T, Fujiwara H, Noguchi H, Hoshino T, Ohdomari I. Novel interatomic potential energy function for si, O mixed systems. *Japanese journal of applied physics*. 1999;38(4A):L366.
23. Barnard A, Russo S, Snook I. Structural relaxation and relative stability of nanodiamond morphologies. *Diamond and related materials*. 2003;12(10):1867-1872.
24. Barnard AS, Zapol P. A model for the phase stability of arbitrary nanoparticles as a function of size and shape. *J Chem Phys*. 2004;121(9):4276-4283.
25. Barnard A, Curtiss L. Computational nanomorphology: Modeling shape as well as size. *Rev. Adv. Mater. Sci*. 2005;10:105-109.
26. Barnard AS, Zapol P. Effects of particle morphology and surface hydrogenation on the phase stability of ti O 2. *Physical Review B*. 2004;70(23):235403.
27. Barnard A. Modelling of nanoparticles: Approaches to morphology and evolution. *Reports on Progress in Physics*. 2010;73(8):086502.
28. Winter NW, Ree FH. Carbon particle phase stability as a function of size. *Journal of computer-aided materials design*. 1998;5(2-3):279-294.

29. Barnard A, Russo S, Snook I. Size dependent phase stability of carbon nanoparticles: Nanodiamond versus fullerenes. *J Chem Phys*. 2003;118(11):5094-5097.
30. Zhang H, Huang F, Gilbert B, Banfield JF. Molecular dynamics simulations, thermodynamic analysis, and experimental study of phase stability of zinc sulfide nanoparticles. *The Journal of Physical Chemistry B*. 2003;107(47):13051-13060.
31. Wright K, Gale JD. Interatomic potentials for the simulation of the zinc-blende and wurtzite forms of ZnS and CdS: Bulk structure, properties, and phase stability. *Physical Review B*. 2004;70(3):035211.
32. Wang S, Ye H. First-principles study on elastic properties and phase stability of III-V compounds. *physica status solidi (b)*. 2003;240(1):45-54.
33. Baletto F, Ferrando R. Structural properties of nanoclusters: Energetic, thermodynamic, and kinetic effects. *Reviews of modern physics*. 2005;77(1):371.
34. Calvo F, Spiegelmann F. Mechanisms of phase transitions in sodium clusters: From molecular to bulk behavior. *J Chem Phys*. 2000;112(6):2888-2908.
35. Neyts EC, Bogaerts A. Numerical study of the size-dependent melting mechanisms of nickel nanoclusters. *The Journal of Physical Chemistry C*. 2009;113(7):2771-2776.
36. Zhang Y, Li S, Yan W, Stephen DT. Effect of size-dependent grain structures on the dynamics of nanoparticle coalescence. *J Appl Phys*. 2012;111(12):124321.
37. Qi W, Wang M. Size effect on the cohesive energy of nanoparticle. *J Mater Sci Lett*. 2002;21(22):1743-1745.
38. Nanda K, Sahu S, Behera S. Liquid-drop model for the size-dependent melting of low-dimensional systems. *Physical Review A*. 2002;66(1):013208.
39. Shandiz MA, Safaei A, Sanjabi S, Barber Z. Modeling the cohesive energy and melting point of nanoparticles by their average coordination number. *Solid State Commun*. 2008;145(9):432-437.
40. Safaei A, Shandiz MA, Sanjabi S, Barber Z. Modeling the melting temperature of nanoparticles by an analytical approach. *The Journal of Physical Chemistry C*. 2008;112(1):99-105.
41. Pawlow P. The dependency of the melting point on the surface energy of a solid body. *Z Phys Chem*. 1909;65:545-548.
42. Wautelet M, Dauchot J, Hecq M. On the phase diagram of non-spherical nanoparticles. *Journal of Physics: Condensed Matter*. 2003;15(21):3651.

43. Zachariah MR, Carrier MJ. Molecular dynamics computation of gas-phase nanoparticle sintering: A comparison with phenomenological models. *J Aerosol Sci.* 1999;30(9):1139-1151.
44. Cushing BL, Kolesnichenko VL, O'Connor CJ. Recent advances in the liquid-phase syntheses of inorganic nanoparticles. *Chem Rev.* 2004;104(9):3893-3946.
45. Zeng P, Zajac S, Clapp P, Rifkin J. Nanoparticle sintering simulations. *Materials Science and Engineering: A.* 1998;252(2):301-306.
46. Koparde VN, Cummings PT. Sintering of titanium dioxide nanoparticles: A comparison between molecular dynamics and phenomenological modeling. *Journal of Nanoparticle Research.* 2008;10(7):1169-1182.
47. Koparde VN, Cummings PT. Phase transformations during sintering of titania nanoparticles. *ACS nano.* 2008;2(8):1620-1624.
48. Alimohammadi M, Fichthorn KA. Molecular dynamics simulation of the aggregation of titanium dioxide nanocrystals: Preferential alignment. *Nano letters.* 2009;9(12):4198-4203.

Chapter 3

3 Simulation Methods

3.1 Introduction

The aim of atomistic simulation is to understand and model the motion of each atom in a material. There are different modeling techniques capable of simulating systems at the atomic scale, nanoscale, microscale, mesoscale, and macroscale systems. Quantum mechanical approaches, such as exact diagonalization and Density Functional Theory (DFT) methods, are applicable in the atomic and nanoscale range. In comparison, molecular dynamics simulation is classical simulation of collective physical movements of large numbers of atoms and molecules, bridging the atomic scale to meso/macro-scale phenomena, thereby helping to study the basic properties of materials. The trajectories of atoms are determined by numerically solving the equations of motion, and the time-dependent behavior of a molecular system is defined by integrating their equations of motion. The forces between atoms are determined by potential force fields, which are very material and objective specific. An open-source classical MD simulation program, Large-scale Atomic/Molecular Massively Parallel Simulator (LAMMPS)¹, is utilized in our study. Three kinds of potential, i.e. Tersoff, Albe and Stillinger-Weber (SW) potentials, are investigated to find the most favorable one for simulating c-BN nanoclusters.

3.2 Implementation of Potentials

We tested the three aforementioned empirical potentials for c-BN using LAMMPS, starting with c-BN crystals with a 5x5x5 unit cell that consists of 1000 atoms in the MD

box with periodic boundary conditions. The time step used is 0.1 femtosecond. The simulation is run in the microcanonical (NVE) ensemble at two initial temperatures, i.e. at room temperature and at 4400K (which is about 1100K higher than the reported melting temperature of c-BN²). Next, we cut a c-BN nanoparticle from a perfect lattice and place it in a MD box with sufficient vacuum space so that it is isolated in a gas phase, with periodic boundary conditions are imposed. The nanoparticle simulation is run in NVE with the initial temperature close to the reported c-BN melting temperature, i.e. ~3246 K. The results are discussed in the following sections.

3.2.1 Tersoff Potential

As discussed in the literature review in Chapter 2, three main groups have used the Tersoff potential for the MD simulation of c-BN crystals, i.e. Sekkal et al.³, Matsunaga et al.⁴, and Moon et al.⁵. Since Sekkal and co-workers treated the B-N bond as a single component, i.e. boron and nitrogen use the same Tersoff parameters, their approach may not be sufficient for studying the melting/decomposition behavior of c-BN nanoclusters. If decomposition occurs, it would involve breaking and formation of inter-species B-N bonds as well as intra-species B-B and N-N bonds. When we adopted the Matsunaga et al.'s parameters⁴, the simulation for bulk failed in NVE conditions with an initial temperature of 4400K because of a sudden collapse of the crystalline structure. Simulation using parameters from Moon et al. passed the test of successfully simulating bulk c-BN crystal at both 300 K and 4400 K in NVE conditions. Hence, we further examined the MD simulation of an octahedral c-BN nanoparticle with an initial temperature close to the reported c-BN melting temperature. It was found that a sheet of BN layer peeled off from the surface of the c-BN nanoparticle, as shown in Figure 3-1. In

addition, chains of atoms also detached from the surface and were observable in the vacuum space around the nanoparticle. Additionally, the peeled off structures attached and detached periodically from the surface of the nanoparticle. These effects indicate that the Tersoff potential may not be adequate for simulating c-BN nanoparticles in high temperature environments.

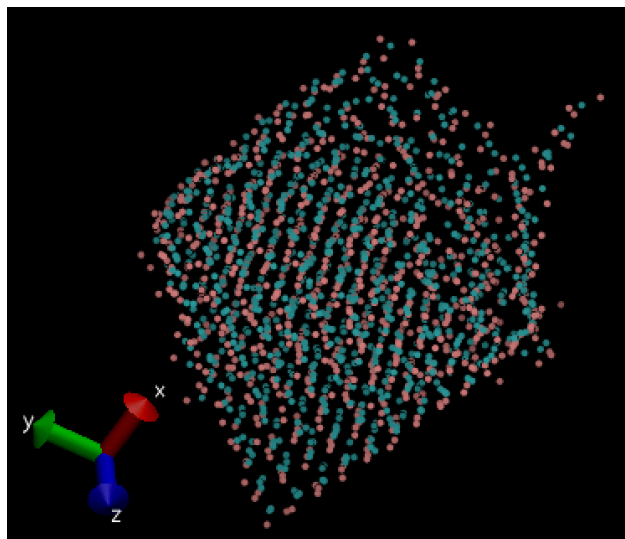


Figure 3-1. Octahedron c-BN nanoparticle in MD simulation with the application of Moon's Tersoff potential

3.2.2 Albe Potential

The Albe potential is very similar to the Tersoff potential, but the repulsive and attractive force terms are exponential functions of the pair distance as discussed in Chapter 2. We implemented the Albe potential in LAMMPS by modifying the existing Tersoff many-body potential module, using the parameters from Albe's work⁶. Like Moon et al.'s parameters for the Tersoff potential, the Albe potential also passed the test of simulating bulk c-BN crystal at 300 K NVE and 4400 K NVE conditions. Thus, the MD simulation of an octahedral c-BN nanoparticle with an initial temperature close to the reported c-BN melting temperature is examined. However, this c-BN nanoparticle started to disintegrate,

with all the atoms separating eventually. Therefore, we do choose to use Albe potential for simulating c-BN nanoparticles under high temperature environments.

3.2.3 Stillinger-Weber Potential

Moon and Hwang⁷ adjusted the two-body force term of the Stillinger-Weber potential for c-BN and w-BN. As such, we modified the code in the LAMPS SW potential module in accordance with their modified SW potential. The parameters of the SW potential are identical to Moon and Hwang's study, except for the ϵ values. Due to variations between different computational packages for implementing the SW potential, we needed to adjust the potential minima via ϵ for optimal relaxation of the crystal structure. We fine-tuned the ϵ values to obtain a lattice constant and cohesive energy close to Moon's values⁷, and the ϵ values are 1.075, 1.012, and 1.012 for B-B, B-N, and N-N bond respectively, while Moon used the value of 1 for all three. As shown in Figure 3-2, the lattice constant of c-BN from Moon's work is 3.6078 Å, and is 3.6076 Å from our parameters. The values of the cohesive energy are -6.718 eV/atom and -6.717 eV/atom, respectively.

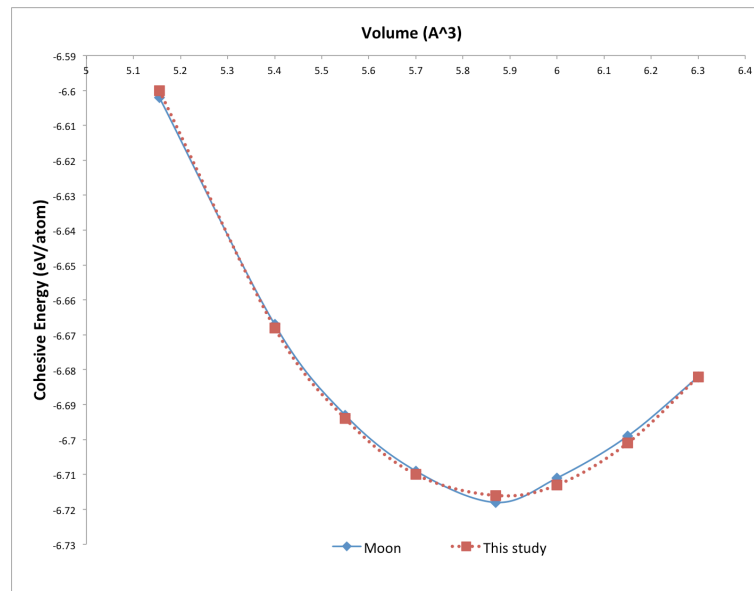


Figure 3-2. Cohesive energy of c-BN

The test of simulating bulk c-BN crystal at 300 K NVE and 4400 K in NVE conditions is successful using the SW potential, and the c-BN octahedron nanoparticle is also successfully simulated. Therefore, our MD study of c-BN nanoparticles will adopt the modified Stilling-Weber potential from Moon's work⁷. We will now discuss the MD simulations of c-BN bulk crystals in the next section.

3.3 MD Simulation of c-BN Bulk Crystal

The structural properties of c-BN crystal are determined by employing the SW potential in MD simulations, which is discussed in the following section. Moreover, we subject c-BN bulk crystals to a high temperature environment to observe the melting behavior of c-BN, which we will use as a reference for c-BN nanoparticle simulations.

3.3.1 Properties of c-BN Bulk Crystal

To obtain the lattice constant as a function of temperature, we carry out MD simulations in an isothermal-isobaric (NPT) ensemble, i.e. fixed number of atoms, pressure, and temperature, for the c-BN bulk crystal with 10x10x10 unit cells containing 8000 atoms in periodical boundary condition. The target pressure of the simulations is 0 GPa, and the temperature ranges from 1500 K to 4000 K. The result from the NPT simulations is shown as the blue diamond curve in Figure 3-3, and the linear thermal expansion can be extracted from this result, i.e. $\alpha_L = (\partial a / \partial T) / a$ at constant pressure. Here, we obtain a value of $\alpha_L = 2.07 \times 10^{-6} \text{ K}^{-1}$, compared with the value of $\alpha_L = 5.47 \times 10^{-6} \text{ K}^{-1}$ from Moon's result⁷. Since our value is about only 1/3 of Moon's result, we carry out further simulations in the canonical (NVT) ensemble for verification of our results.

The range of temperature in the NVT simulations is from 2000 K to 3200 K, and we change the volume of the c-BN crystal and record the total energy and pressure results from the NVT simulations. We next find the lattice constant (a_0) at that specific temperature by locating the zero pressure point and plot it as a green cross in Figure 3-3. The estimated lattice constant (a_0) from the NVT simulations agrees with the result from the NPT simulations. In addition, the lattice constant of c-BN as a function of temperature can be obtained from the polynomial fitting of MD data and is given in Equation 3-1. Thus, the high temperature performance in our MD simulations might result in a less-stretchable lattice constant for c-BN clusters.

Equation 3-1: $a(T) = 3.6074 + 8 \times 10^{-6}T + 9 \times 10^{-12}T^2$

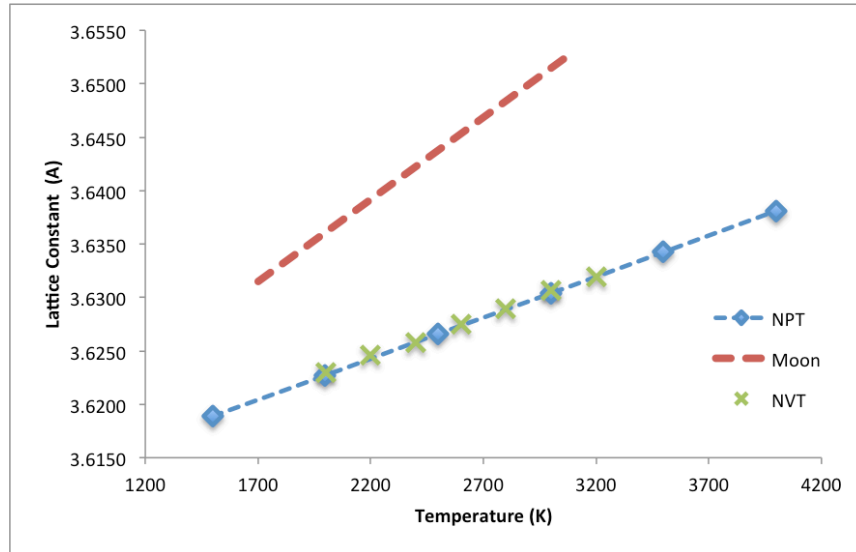


Figure 3-3. Lattice constant of c-BN as a function of temperature

3.3.2 Melting of c-BN Bulk Crystal

The c-BN bulk crystal with 10x10x10 unit cells containing 8000 atoms is simulated in the NVE microcanonical ensemble with various initial temperatures for detailed study of the melting process. Since melting of a perfect lattice is in the metastable regime, we introduce dislocations by cutting planes out from the c-BN bulk crystal, as shown in

Figure 3-4. This imperfect c-BN bulk crystal contains 7620 atoms with an equal number of boron atoms and nitrogen atoms, and the simulation is run in NVE with an initial temperature of 4000 K, compared with the experimentally reported melting point of 3246K^2 . After 45 nanoseconds of simulation, with a time step of 0.1 femtosecond (450,000,000 steps in total), one end and a few spots in the dislocation planes start to melt, but the crystalline structure still remains intact. If the initial temperature of the NVE simulation is raised up to 4400 K, the melting starts much earlier at 3 nanoseconds.

In general, the dislocations have a reduced coordination number and higher mobility, acting as imperfection sites for the initiation of melting⁸⁻¹⁰. Therefore, the melting temperature in c-BN bulk crystals with dislocations should correspond to the phase equilibrium coexistence boundary, being lower than that of a perfect crystal which may not melt until the spinodal limit. However, it still takes a long simulation time for a c-BN bulk crystal with dislocations to start melting at a high temperature of 4000 K. Due to the limitation of computational resource, we could not define the precise melting temperature of c-BN bulk crystals. Instead, we obtained the caloric curve of c-BN bulk crystals with dislocations from NVE simulations with various initial temperatures, as shown in Figure 3-6. Here, we only can conclude that at the specific c-BN crystal with plane dislocations has a phase transition happening around 4150 K due to the discontinuity in its caloric curve.

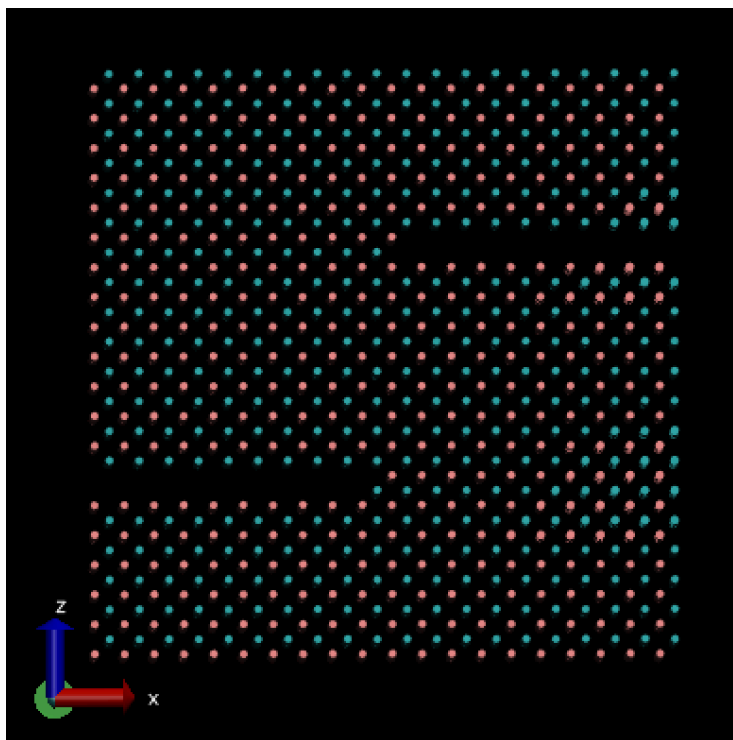


Figure 3-4. Cubic BN with plane dislocations

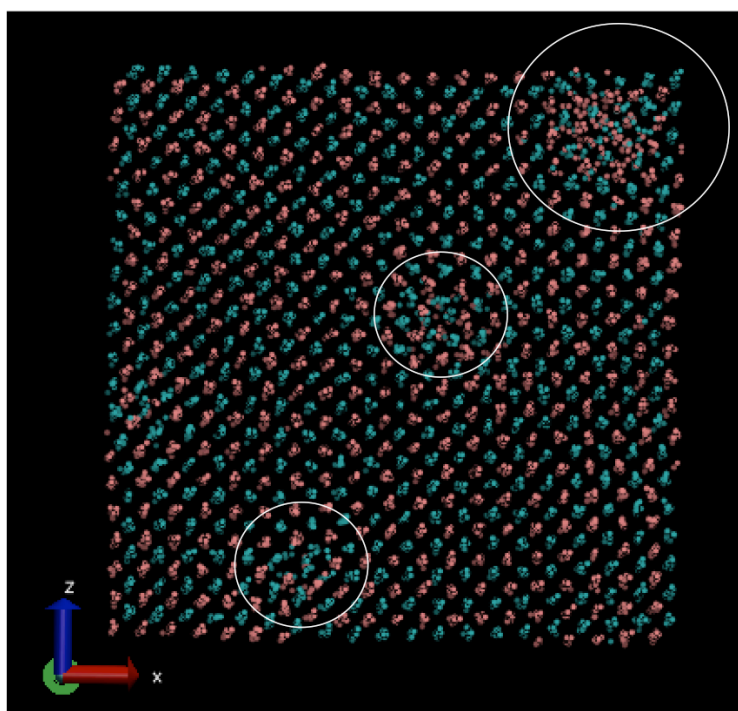


Figure 3-5. Cubic BN crystal with plane dislocations in NVE with initial $T=4000\text{K}$ for 45ns

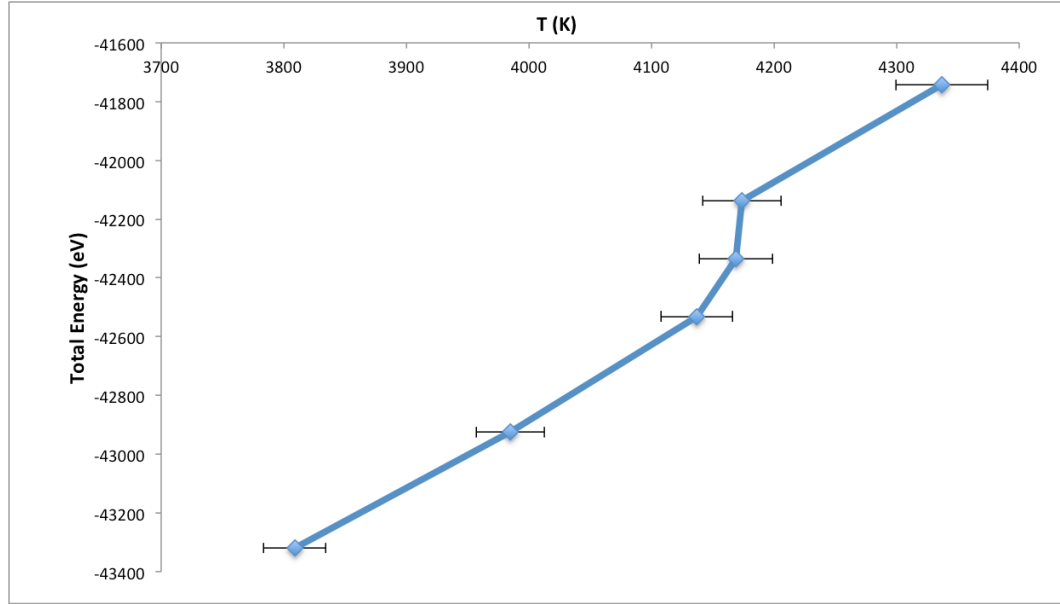


Figure 3-6. The caloric curve of c-BN crystals with plane dislocations in NVE with various initial temperatures

3.4 MD Simulation of c-BN nanoparticles

Each c-BN nanoparticle is excised from a perfect lattice in accordance to the shapes, namely cube, cuboctahedron, octahedron, and truncated octahedron. The nanoparticle is placed in a MD box with sufficient vacuum space so that it is isolated in a gas phase, and periodic boundary conditions are imposed. Due to conservation of angular momentum, the c-BN nanoparticle starts rotating when the surface nitrogen atoms begin vaporizing. Since the c-BN nanoparticle is simulated in an MD box with periodic boundary conditions, the vaporized nitrogen atoms fly around in the gas phase and sometimes get re-absorbed by the nanoparticle, but leave the nanoparticle again soon after. The NVE and NVT ensembles are utilized in MD simulation of c-BN nanoparticles; and the trajectory, velocity, and acceleration of each atom are recorded every picosecond. The temperature, kinetic energy, potential energy, and total energy of the nanoparticle are also monitored.

Due to conservation of momentum, the nature of MD simulation, the c-BN nanoparticle starts rotating when the surface nitrogen begins vaporizing and sometimes crosses the boundary. For data analysis, we develop a post-processing code for measuring the properties of four regions (shells) comprising the nanoparticle as well as the entire nanoparticle, and more importantly, for handling the problem of the nanoparticle crossing the boundary of the MD box. The code reconstructs the neighbor list of each atom, re-sorts atoms in each shell according to their distance from the center of the nanoparticle, and measures the bond stretch, Lindemann index, and temperature for each atom of the nanoparticle at every 1 picosecond. This procedure allows us to track the gas atoms, the number of B-N bonds, B-B bonds, and N-N bonds; hence, we are able to calculate the average coordination number and the average bond length of the nanoparticle. Matlab is used here for plotting the properties of the c-BN nanoparticle as a function of time. Thus, we have detailed information available for visualizing our results in VMD¹¹. The details of the MD simulation of c-BN nanoparticles will be discussed in Chapters 4, 5, and 6.

3.5 References

1. Sandia National Laboratory. Large-scale atomic /molecular massively parallel simulator. *LAMMPS*. ;lammmps-28Aug12.
2. Madelung O, Rossler U, Schulz M. Boron nitride (BN), melting point, debye temperature density, entropy,etc., cubic modification. In: *Group IV elements, IV-IV and III-V compounds. part b - electronic, transport, optical and other properties*. Vol 41A1b. Springer Berlin Heidelberg; 2002:1-8.
3. Sekkal W, Bouhafs B, Aourag H, Certier M. Molecular-dynamics simulation of structural and thermodynamic properties of boron nitride. *Journal of Physics: Condensed Matter*. 1998;10(23):4975.
4. Matsunaga K, Fisher C, Matsubara H. Tersoff potential parameters for simulating cubic boron carbonitrides. *Japanese Journal of Applied Physics*. 2000;39(1A):L48.

5. Moon WH, Son MS, Hwang HJ. Molecular-dynamics simulation of structural properties of cubic boron nitride. *Physica B: Condensed Matter*. 2003;336(3):329-334.
6. Albe K, Möller W. Modelling of boron nitride: Atomic scale simulations on thin film growth. *Computational Materials Science*. 1998;10(1):111-115.
7. Moon WH, Hwang HJ. A modified Stillinger–Weber empirical potential for boron nitride. *Appl Surf Sci*. 2005;239(3):376-380.
8. Nelson DR, Halperin B. Dislocation-mediated melting in two dimensions. *Physical Review B*. 1979;19(5):2457.
9. Cotterill R, Kristensen WD, Jensen E. Molecular dynamics studies of melting: III. spontaneous dislocation generation and the dynamics of melting. *Philosophical Magazine*. 1974;30(2):245-263.
10. Esfarjani K. A theory of quantum melting and its application to the wigner solid. . 1991.
11. Humphrey W, Dalke A, Schulten K. VMD: Visual molecular dynamics. *J Mol Graph*. 1996;14(1):33-38.

Chapter 4

4 Geometric Stability and Surface Reconstruction of c-BN

Nanoparticles

4.1 Introduction

We are interested in studying the fundamental properties of c-BN nanoparticles; and in this chapter, we will examine the stability of c-BN nanoparticles of varying shapes using two different methods. First, we carry out a ground state energy analysis using the modified Stillinger-Weber potential (Equation 4-1) to calculate the surface binding energy of different crystallographic terminations, namely the {100}, {110}, and {111} facets of the c-BN nanoparticle with both boron and nitrogen termination. This process allows us to determine the geometric dependence of the stability for the cubic, octahedral, cuboctahedral, and truncated octahedral nanoparticles. Second, we examine the melting/decomposition characteristics of the different shaped nanoparticles via MD simulations in a microcanonical (NVE) ensemble. The melting phenomenon of the nanoparticles is monitored using the Lindemann index, a bond-length fluctuation indicator.

Equation 4-1: $U = \sum V_2(\mathbf{r}_{ij}) + \sum V_3(\mathbf{r}_i, \mathbf{r}_j, \mathbf{r}_k)$

$$V_2(r_{ij}) = \varepsilon f_2\left(\frac{r_{ij}}{\sigma}\right), \quad f_2(r) = \begin{cases} A(Br^{-p} - r^{-q}) \exp\left[\delta/r - a\right], & r < a \\ 0, & r \geq a \end{cases}$$

$$V_3(r_i, r_j, r_k) = \varepsilon f_3\left(\frac{r_i}{\sigma}, \frac{r_j}{\sigma}, \frac{r_k}{\sigma}\right), \quad f_3(r_i, r_j, r_k) = h(r_{ij}, r_{ik}, \theta_{jik}) +$$

$$h(r_{ji}, r_{jk}, \theta_{ijk}) + h(r_{ki}, r_{kj}, \theta_{ikj}), \quad h(r_{ij}, r_{ik}, \theta_{jik}) = \lambda \exp\left[\gamma(r_{ij} - a)^{-1} + \right.$$

$$\left. \gamma(r_{ik} - a)^{-1}\right] \times (\cos\theta_{jik} + \kappa)^2, \quad \lambda > 0$$

The large surface area to volume ratio of nanoparticles plays a crucial role in many of its unique properties, including plasmonics, catalysis, and biological sensing¹⁻⁷. The size of the nanoparticle also strongly affects its physical properties, and experiments have shown that the melting temperature decreases with the size of the nanoparticle⁸. Clearly, the stability of the nanoparticle will also have a strong surface dependence, and our energy analysis shows that the $\{111\}$ facet has the lowest potential energy. Hence, the octahedron-shaped nanoparticle, which consists solely of $\{111\}$ facets, has the lowest ground state energy, followed by truncated octahedron, cuboctahedron, and finally cube, in order of stability.

We verify our energy analysis by simulating the melting of the varied shaped nanoparticles in an NVE micro-canonical ensemble, and monitor the melting process using the Lindemann index. In general, we find that the melting temperatures of the nanoparticles follow the prediction of the energy analysis, with the cube melting at the lowest temperature, followed by the cuboctahedron. However, surprisingly, the truncated octahedron has a slightly higher melting temperature than does the octahedron, which is due to the effects of corners on melting and surface reconstruction. As we will discuss later, this effect is related to the melting mechanism of c-BN nanoparticles.

4.2 Ground State Energy Analysis of Nanoparticle Geometry

To calculate the bulk binding energy, as well as the surface energies of the $\{100\}$, $\{110\}$ and $\{111\}$ crystallographic facets, the c-BN bulk crystals and slabs of varying shapes and sizes are utilized for extracting energy information. We adopt the modified Stillinger-Weber (SW) potential as shown in Equation 4-1, which is widely used for describing the

covalent bonding in semiconductors, with modifications by Moon and Hwang⁹ for boron nitride.

We find that the energy per unit volume of c-BN is $e_{\text{bulk}} = -1.1572 \text{ eV/\AA}^3$; and the stability of different crystallographic terminations of c-BN is also obtained. The energy per unit surface area of c-BN $\{100\}$, $\{110\}$, and $\{111\}$ facets is displayed in Table 4-1. From the results, the $\{111\}$ facet is found to be more stable than the $\{100\}$ facet due to its larger average coordination number – a value of 3 for the $\{111\}$ facet and a value of 2 for the $\{100\}$ facet, compared to the value of 4 for full-coordinated c-BN. The $\{110\}$ is the cleavage plane of c-BN crystals, and the forming of striations with a $\{110\}$ direction are found on the real c-BN $\{100\}$ faces¹⁰. Synthesized c-BN crystals contain mainly $\{111\}$ and $\{100\}$ faces, and the striations parallel to $\{110\}$ direction are used for characterization of $\{111\}$ and $\{100\}$ faces¹¹. Therefore, in this study, we consider c-BN nanoparticles with four main kinds of geometry, i.e. cube, octahedron, truncated octahedron, and cuboctahedron. Cube has a simple $\{100\}$ facet-terminated geometry, and octahedron has $\{111\}$ facet-terminated geometry. Truncated octahedron geometry is formed by truncating the six corners of an octahedron, thereby forming $\{100\}$ square facets at these corners. A cuboctahedron is obtained from cutting away the eight corners of a cube, forming triangular $\{111\}$ facets.

Table 4-1: Summary of surface energy of different facets of c-BN.

Facet	Energy per unit surface area (eV/ \AA^2)	Average Coordination Number
$\{100\}$	$\gamma_{100} = -1.0438$	2
$\{110\}$	$\gamma_{110} = -1.9524$	3
$\{111\}$	$\gamma_{111} = -2.1240$	3

Using these results, we compare the potential energy of a pure $\{111\}$ -faceted c-BN nanoparticle (i.e. octahedron) with one having $\{100\}$ facets (like cube) and a mixture of $\{100\}$ and $\{111\}$ facets (like cuboctahedron and truncated octahedron) by simply calculating the bulk energy and surface energy ($E = e_{bulk} \times C_1 L^3 + Y \times C_2 L^2$). Figure 4-1 shows the energy per atom versus the inverse of one over the cube root of the number of atoms ($\frac{1}{N^{1/3}}$) comprising the nanoparticle. The cube has the steepest slope due to the highest surface energy of pure $\{100\}$ facets, followed by the cuboctahedron with six square $\{100\}$ facets and eight triangular $\{111\}$ facets, and the truncated octahedron with six square $\{100\}$ facets and eight hexagonal $\{111\}$ facets. We have also calculated the energy per atom versus particle size for the four different kinds of c-BN shapes, as shown in Figure 4-2.

The octahedron is the most stable shape because of its lowest surface energy from the energy analysis. Moreover, this type of c-BN particles has been synthesized in experiments. Wentorf¹² found octahedral c-BN crystal fragments of up to 300 μm in HP-HT synthesis of c-BN; and Lian et al.¹³ obtained octahedral c-BN particles of around 1 μm in hydrothermal solutions, as shown in Figure 4-3. Therefore, we focus upon the melting mechanism and properties of octahedral c-BN nanoparticles in our molecular dynamics simulations, which are discussed in detail in Chapter 5.

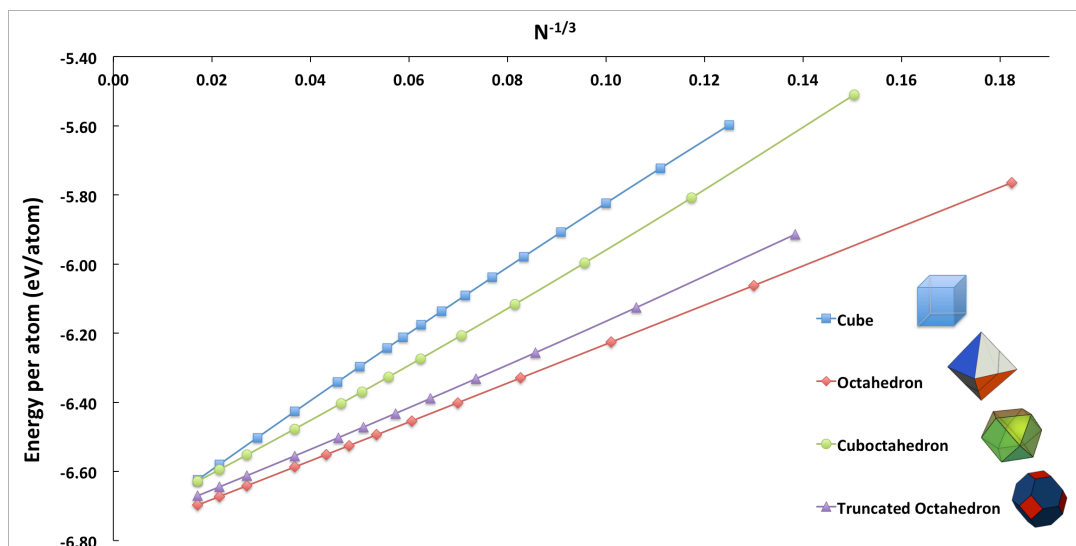


Figure 4-1. Surface energy of various shapes of c-BN nanoclusters. L refers to the side length, and the circled sizes are chosen for MD simulation.

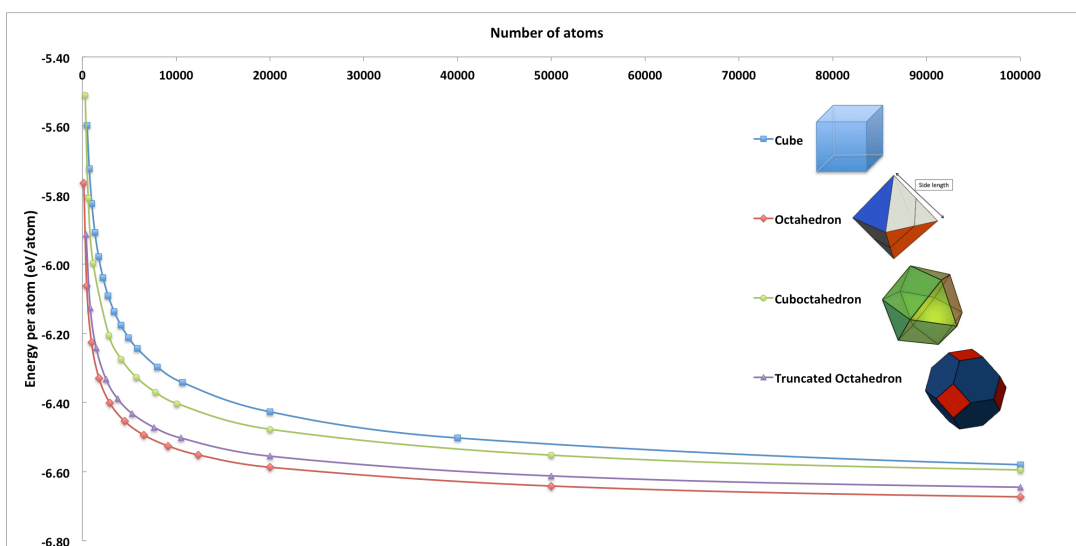


Figure 4-2. Energy w.r.t. sizes of various shapes of c-BN nanoclusters.

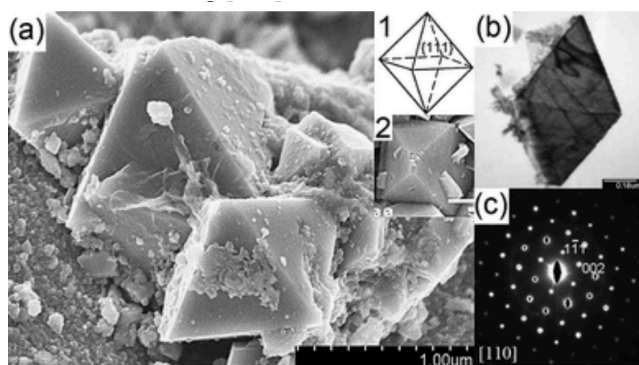


Figure 4-3. Morphology and the corresponding SAED patterns of c-BN crystals (reproduced from [12]).

4.3 Melting Estimation by Lindemann Index

We utilize a bond-length fluctuation indicator, the Lindemann index, which is defined in Equation 4-2, to monitor the melting behavior of c-BN nanoparticles. The Lindemann index of the entire nanoparticle is plotted with respect to temperature, and the onset of melting is estimated as the temperature at which the Lindemann index deviates from its low-temperature linear behavior. Figure 4-4 shows the overall cluster Lindemann index of a 2.55-nm octahedral c-BN nanoparticle. The Lindemann index initially increases linearly between 2150K and 2950K, as the vibrational motion of the atoms increases with kinetic energy and temperature. At the onset of melting, the Lindemann index starts to exhibit nonlinear behavior because the boron-nitrogen bonds start to break, and there is increased motion of the boron and nitrogen atoms. In the MD simulations, melting of c-BN nanoparticles is observed to be a complex process involving both surface reconstruction and phase separation of the boron and nitrogen. A careful discussion of the surface reconstruction process is discussed later in Section 4.4.1, and a detailed discussion of the melting process is deferred to Chapter 5, where a careful study of the melting process of the octahedral c-BN nanoparticle is presented.

Equation 4-2:
$$\gamma_{np} = \sqrt{\frac{1}{N_{tot}} \sum_{i=1}^{N_{tot}} \frac{(r_{ic} - \langle r_{ic} \rangle)^2}{a^2}}$$

c & a denote the center of nanoparticle & lattice constant

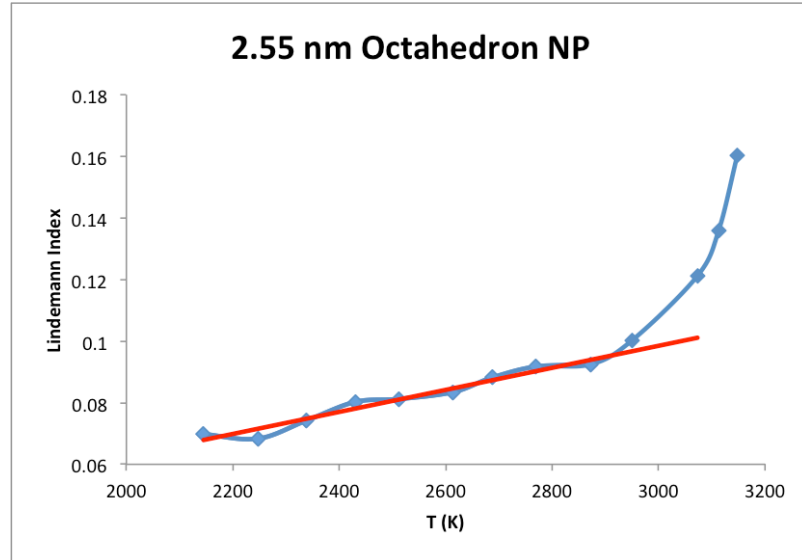


Figure 4-4. The overall Lindemann index of 2.55 nm octahedral c-BN nanoparticle w.r.t. temperature

4.4 Geometric Stability and Surface Reconstruction of c-BN Nanoparticles

In this section, we discuss the stability of various c-BN nanoparticle shapes by comparing the melting of cube, octahedron, cuboctahedron, and truncated octahedron c-BN nanoparticles. Most remarkably, we observe surface reconstruction of the $\{100\}$ facet, with resultant formation of the stable $\{111\}$ facet, during the melting process of the cube, cuboctahedron, and truncated octahedron nanoparticles, which all contain $\{100\}$ facets. Such an explicit result is a striking affirmation of our surface energy analysis which predicts the stability of the $\{111\}$ facet. Finally, the spherical c-BN nanoparticle is also investigated, and its stability vis-à-vis the other shapes is discussed towards the end of this section.

4.4.1 Dimerization of $\{100\}$ Facets and Formation of $\{111\}$ Facets from Surface Reconstruction

The surface energy analysis above evinces that the $\{111\}$ facet is the most stable, with the $\{100\}$ facet being the least stable, suggesting that surface reconstruction may occur

on nanoparticles with non- $\{111\}$ facets, and most likely on the $\{100\}$ facets. Indeed, there have been already DFT studies¹⁴ and quantum chemical calculations¹⁵ observing surface reconstruction of the c-BN $\{100\}$ facet. Similarly, we also find that the $\{100\}$ facet displays significant reconstruction in our MD simulations, with formation of boron-boron and nitrogen-nitrogen dimer pairs as well as transformation into the most stable $\{111\}$ facet. Given the classical nature of molecular dynamics, we believe this is a significant result, and strengthens our confidence in the validity of our results.

We shall first focus on the cube as it consists solely of the least stable $\{100\}$ facets. A c-BN cube nanoparticle with a side length of 2.08 nm, containing 1728 atoms, and six $\{100\}$ facets (3 boron-terminated surfaces and 3 nitrogen-terminated surfaces) is relaxed in MD under the microcanonical ensemble (NVE) with an approximate initial temperature of 400 K for 3 nanoseconds. As the simulation is carried out in the microcanonical ensemble, total energy is conserved; hence, any potential energy gained from surface reconstruction will lead to an increase in the internal kinetic energy.

From an initial temperature of 400 K, the temperature rises dramatically to 1600 K, which is determined by averaging over the last 150 picoseconds of the simulation. This response reflects the extensive dimerization of surface atoms that occurs on the $\{100\}$ facets, showing that the $\{100\}$ surface is unstable towards formation of boron-boron and nitrogen-nitrogen dimer pairs even at near room temperatures – a phenomena similar to the well-known reconstruction of Si $\{100\}$ surfaces¹⁶. The original configuration of the cube nanoparticle is shown in Figure 4-5(a). In Figure 4-5(b), the atoms on both the boron and the nitrogen terminated $\{100\}$ surfaces of the cubic nanoparticle tend to dimerize and form B-B and N-N pairs. This reconstruction is due to pairing of the

dangling bonds of the surface atoms, resulting in formation of dimers with lower energies. In fact, we observe that dimerization occurs at all temperatures. Hence, we conclude that the $\{100\}$ facets always reconstruct to form rows of dimerized B-B and N-N pairs after relaxation in MD simulation, as it leads to a nanostructured surface of lower energy.

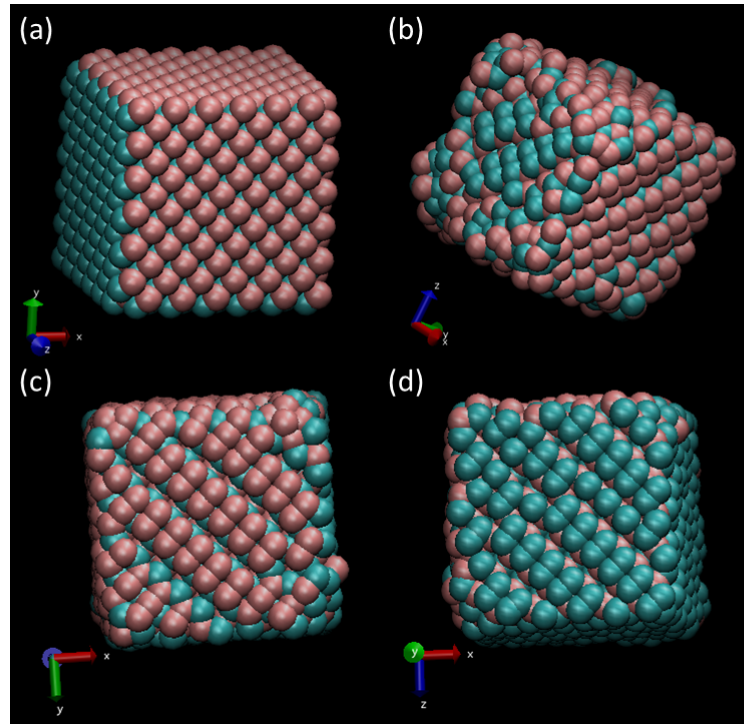


Figure 4-5. Dimerization of c-BN $\{100\}$ facets. Relaxation of the cubic nanoparticle in microcanonical ensemble with an initial temperature of 400 K (a) the initial configuration: pink and green spheres denote boron and nitrogen respectively (b) dimerization on both boron and nitrogen terminations (c) dimerization on boron terminated $\{100\}$ facet (d) dimerization on nitrogen terminated $\{100\}$ facet.

The more striking result that we obtained was the formation of $\{111\}$ facets upon surface reconstruction of the $\{100\}$ facets at around 2900 K. This phenomenon is explicitly seen in Figure 4-6 (c), from an MD simulation of an identical cube nanoparticle with an initial temperature of 2400 K rising to a final temperature around 3070K. The transformation from $\{100\}$ into $\{111\}$ upholds the conclusion from our surface energy analysis that the $\{111\}$ facet is most stable.

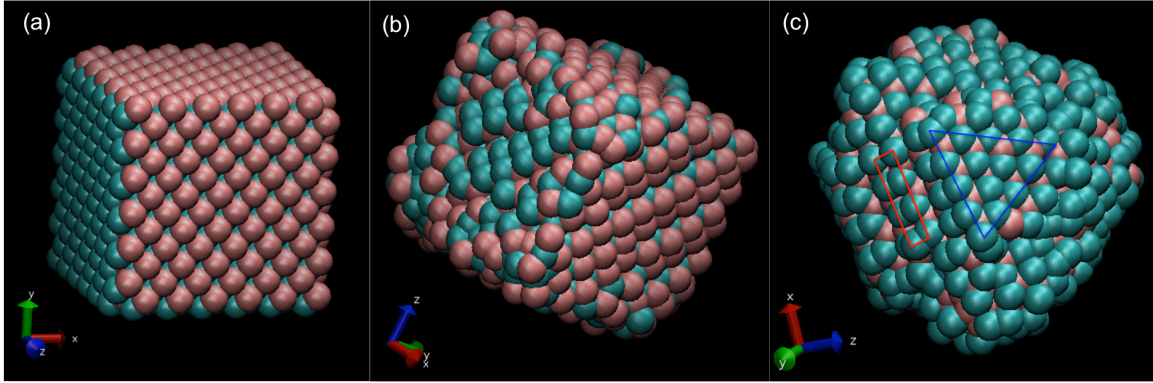


Figure 4-6. Surface reconstruction on c-BN {100} facets. Relaxation of the cubic nanoparticle in microcanonical ensemble with an initial temperature of 2400K (a) the initial configuration: pink and green spheres denote boron and nitrogen respectively (b) dimerization on both boron and nitrogen terminations (c) reconstructed {111} facet shown in blue triangle and dimerized pairs shown in red rectangle

Since reconstruction into the {111} facet gains $171.6 \text{ meV}/\text{\AA}^2$, the reconstructed surface should stabilize the cube nanoparticle, and this is indeed corroborated by the Lindemann index of the cube nanoparticle, as shown Figure 4-7. At 2900 K, a distinct inflexion point is seen with a depressed Lindemann index, indicating that there are reduced fluctuations at that temperature. The mechanism for this stabilization is the formation of {111} facets due to surface reconstruction at around 2900 K, which is verified by visualizing the nanoparticle at 2902 K and slightly below at 2665 K. Figure 4-8 shows the initial cube nanoparticle at a final temperature of 2665 K, where there are no significant patches of reconstructed {111} facets observable. The well-defined dimerized {100} facets have clearly melted, leaving only strips of N-N dimers. However, at 2902 K, patches of reconstructed {111} facets are clearly seen, as illustrated in Figure 4-9. Therefore, we conclude that formation of reconstructed {111} facet acts as a stabilizing mechanism for {100} facets. Noteworthy, the octahedron, which consists solely of {111} facets, starts to melt at the temperature beyond 2950 K; hence, the Lindemann index value at 3017K, as shown in Figure 4-7, jumps up again nonlinearly due to the occurrence of melting on the {111} facet.

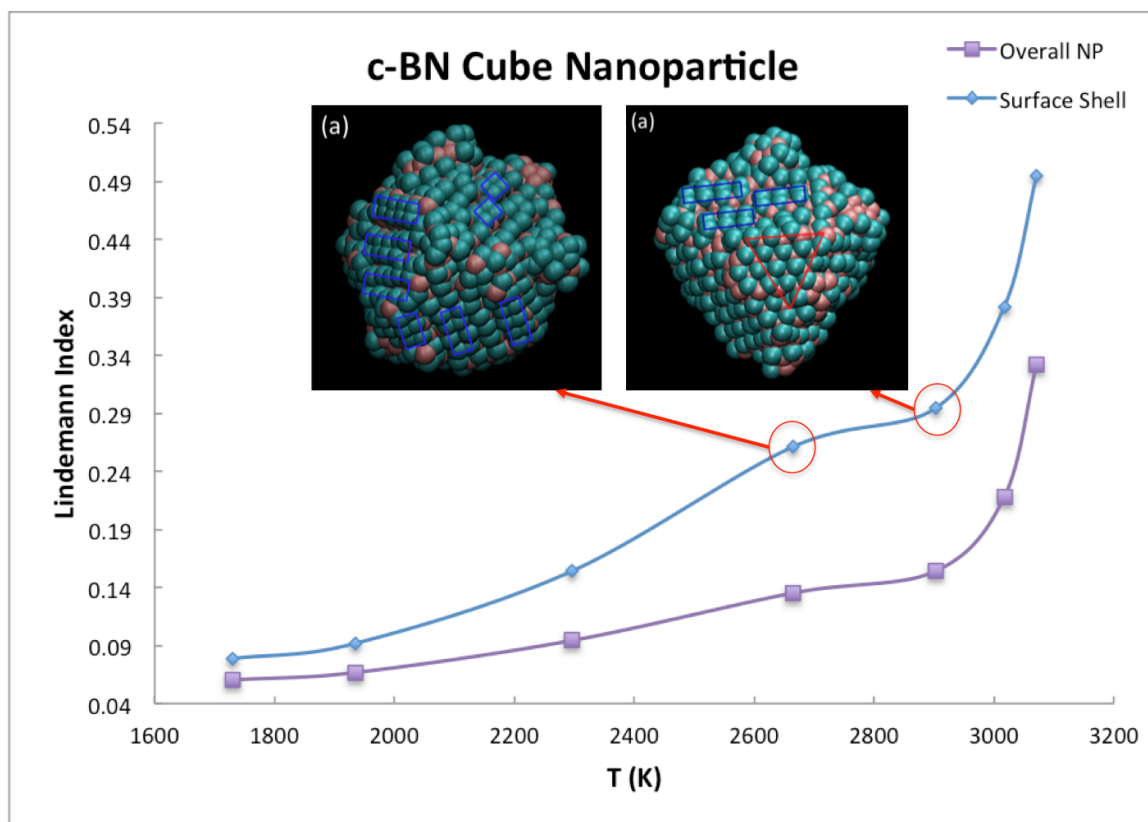


Figure 4-7. Lindemann index of cubic nanoparticle, showing the Lindemann index of both the entire nanoparticle in purple squares, and of the surface shell in blue diamonds. The inset figures show the melted nanoparticles at 2665 K and 2902 K, with significant $\{111\}$ reconstruction at 2902 K

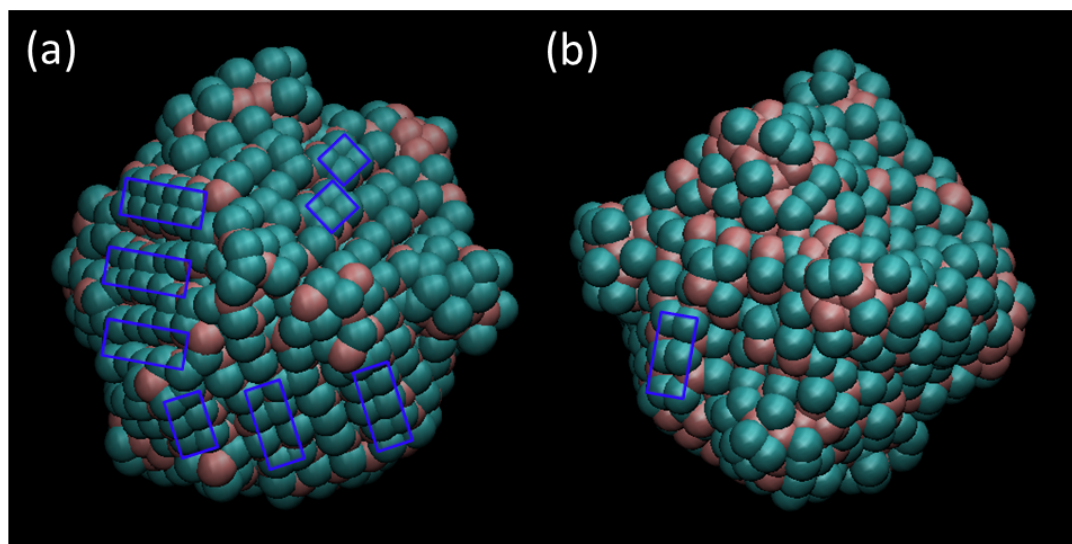


Figure 4-8. Front (a) and rear (b) view of cube nanoparticle relaxed in NVE with final temperature of 2665 K. Dimerized nitrogen pairs are shown in blue rectangles, and no significant $\{111\}$ facet reconstruction is seen

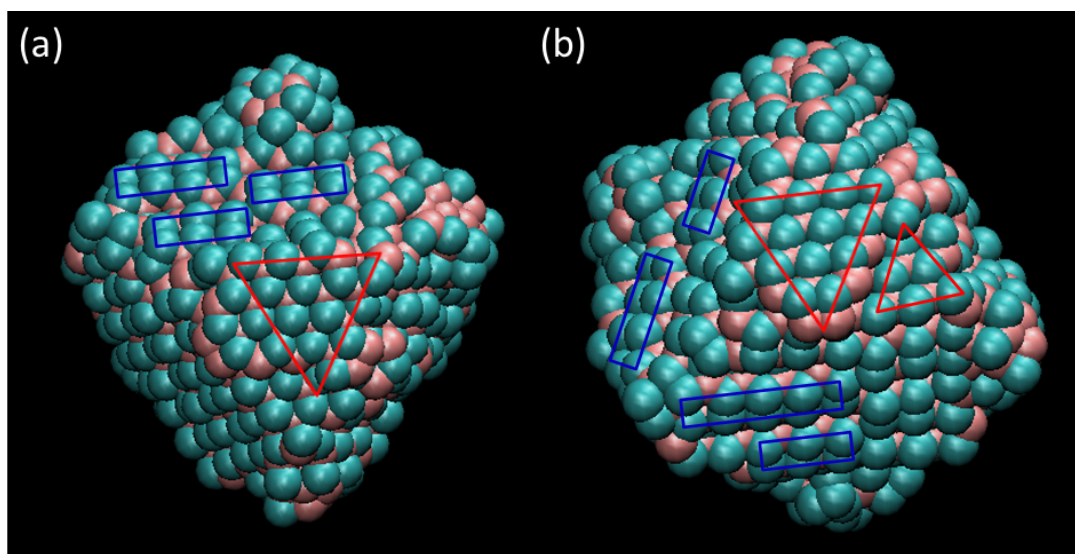


Figure 4-9. Front (a) and rear (b) view of cube nanoparticle relaxed in NVE with final temperature of 2902 K. Dimerized nitrogen pairs are shown in blue rectangles, and significant $\{111\}$ facet reconstruction shown in red rectangles is seen

The phenomena of dimerization and surface reconstruction occur not only in cube nanoparticles, but also on cuboctahedron and truncated octahedron nanoparticles, which have both $\{100\}$ and $\{111\}$ facets. Figure 4-10 shows the initial and melted configurations of a cuboctahedral c-BN cube nanoparticle with a side length of 1.53 nm, containing 1846 atoms, and consisting of six $\{100\}$ facets (3 boron and 3 nitrogen terminated surfaces) that is relaxed in MD under the microcanonical ensemble (NVE) with an initial temperature around 2800K for 3 nanoseconds. Figure 4-11 shows the initial and melted configurations of a truncated octahedral c-BN cube nanoparticle with a side length of 0.89 nm, containing 1592 atoms, and six $\{100\}$ facets (half boron and half nitrogen terminations) that is relaxed in MD under microcanonical ensemble (NVE) with an initial temperature around 3400K for 3ns.

In both the cuboctahedron and the truncated octahedron, clear signs of dimerization of the boron and nitrogen atoms on the $\{100\}$ facets are again manifested.

The boron and nitrogen atoms on the $\{100\}$ facet have a coordination number of 2, i.e. they have two dangling bonds each, and can thus lower their potential energy by forming rows of dimer pairs. This arrangement establishes a more stable and ordered nanostructured surface, with a higher coordination number of 3 instead of 2.

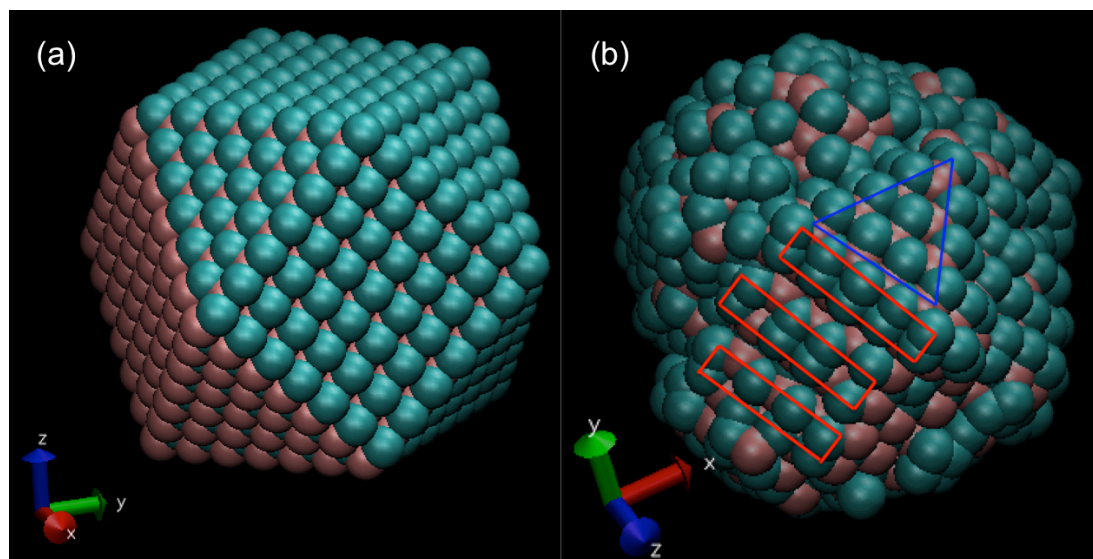


Figure 4-10. Surface reconstruction on c-BN cuboctahedral nanoparticle. Relaxation of the nanoparticle in microcanonical ensemble with an initial temperature of 2800K (a) the initial configuration: pink and green spheres denote boron and nitrogen respectively (b) reconstructed $\{111\}$ facet shown in blue triangle and dimerized pairs shown in red rectangle

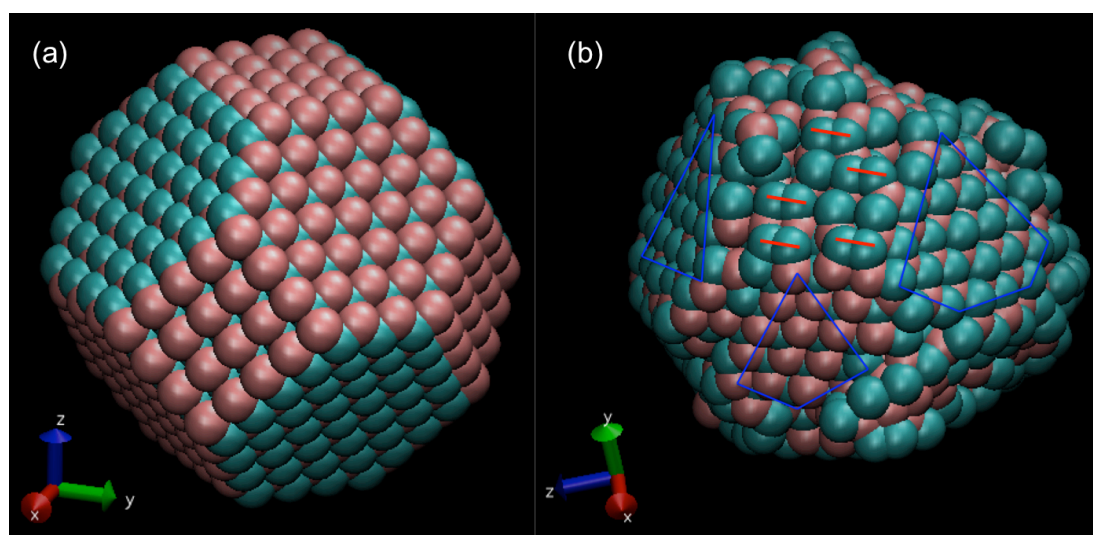


Figure 4-11. Surface reconstruction on c-BN truncated octahedral nanoparticle. Relaxation of the nanoparticle in microcanonical ensemble with an initial temperature of 3400K (a) the initial configuration: pink and green spheres denote boron and nitrogen respectively (b) reconstructed $\{111\}$ facet shown in blue-circled areas and dimerized nitrogen atom pairs are indicated by red bars

4.4.2 Geometric Dependence of Melting Temperature of Nanoparticle

From the energy analysis in Section 4.2, the cohesive energy per atom for cube, cuboctahedron, truncated octahedron, and octahedron are -5.98 eV, -6.0928 eV, -6.254 eV, and -6.3279 eV, respectively. Hence, the melting temperatures of the nanoparticles should have a strong geometric dependence, with the cube being the least stable, followed by cuboctahedron, truncated octahedron, and finally with octahedron being the most stable.

In order to compare properly the melting of c-BN nanoparticles with different shapes as mentioned earlier in the surface energy analysis, the total number of atoms is set to about 1700 for all shapes. The octahedron nanoparticle with a side length of 2.55 nm contains 1771 atoms, and the truncated octahedron nanoparticle with a side length of 0.89 nm has 1592 atoms. The 2.08 nm cube nanoparticle consists of 1728 atoms, and the 1.53 nm cuboctahedron nanoparticle contains 1846 atoms. All of them are uniformly cut to have surface facets where half the terminations are boron and half are nitrogen. As previously discussed, the surface energy strongly affects the ground state energy of a nanoparticle. To investigate the dynamic stability of the nanoparticles, they are relaxed in a microcanonical ensemble with various initial temperatures for a computationally efficient MD simulation of 3 ns.

As explained in Section 4.3, an estimate of the onset of melting for each nanoparticle is obtained by determining the point at which the Lindemann index curve deviates from its low temperature linear behavior; therefore, Figure 4-12 displays the Lindemann index value of the entire cluster with respect to temperature for all four shapes. The Lindemann index for the cube nanoparticle starts to turn up at around 2300 K,

followed by cuboctahedron at around 2700 K, and then octahedron at 2950 K. The truncated octahedron has the highest estimated melting temperature at around 3100 K.

In general, the melting temperatures of the nanoparticles, as estimated from the Lindemann index curves in Section 4.2, follows the same trend, with the sole exception of the truncated octahedron having a slightly higher melting temperature than that for the octahedron, even though it has a slightly smaller cohesive energy, i.e. a difference of 73.9 meV/atom. Since the binding energy of a dimer pair exceeds this small difference, it is strongly likely that the dimerization of the boron and nitrogen atoms stabilizes the truncated octahedral nanoparticle, thereby increasing its melting temperature above that of the octahedron. Although dimerization also occurs in the cuboctahedron, its cohesive energy is more than 150 meV/atom less than those of the octahedron and the truncated octahedron; and dimerization is not expected to affect the relative stability significantly.

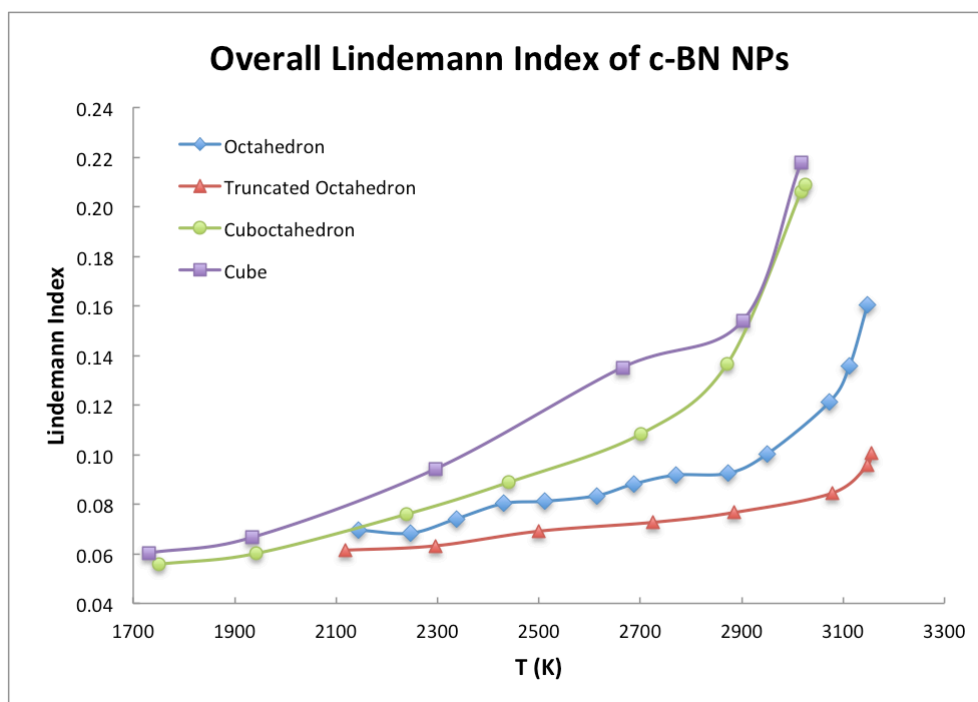


Figure 4-12. Plot of Lindemann index w.r.t temperature of the entire cluster for all four shapes

From the results of Figure 4-7, the surface shells of all four nanoparticles have melted at their respective T_m . Comparing the nanoparticles with the lowest and highest T_m , the Lindemann index value of the surface shell of a cube nanoparticle reaches $\gamma = 0.15$ when the temperature approaches the onset of melting at 2300K. Similarly, the surface shell of a truncated octahedron nanoparticle also displays the beginning of melting when the temperature exceeds 3100K, $\gamma = 0.17$ at 3148 K (Figure 4-13). These results indicate that nanoparticles in this size range undergo a surface melting phenomenon near its melting temperature, which will be discussed in Chapter 5.

Thus, surface reconstruction is an important phenomenon in melting of nanoparticles, with dimerization acting to form more stable nanostructures on $\{100\}$ facets. A detailed study of the melting mechanism by focusing on octahedral nanoparticles will be discussed in the next chapter.

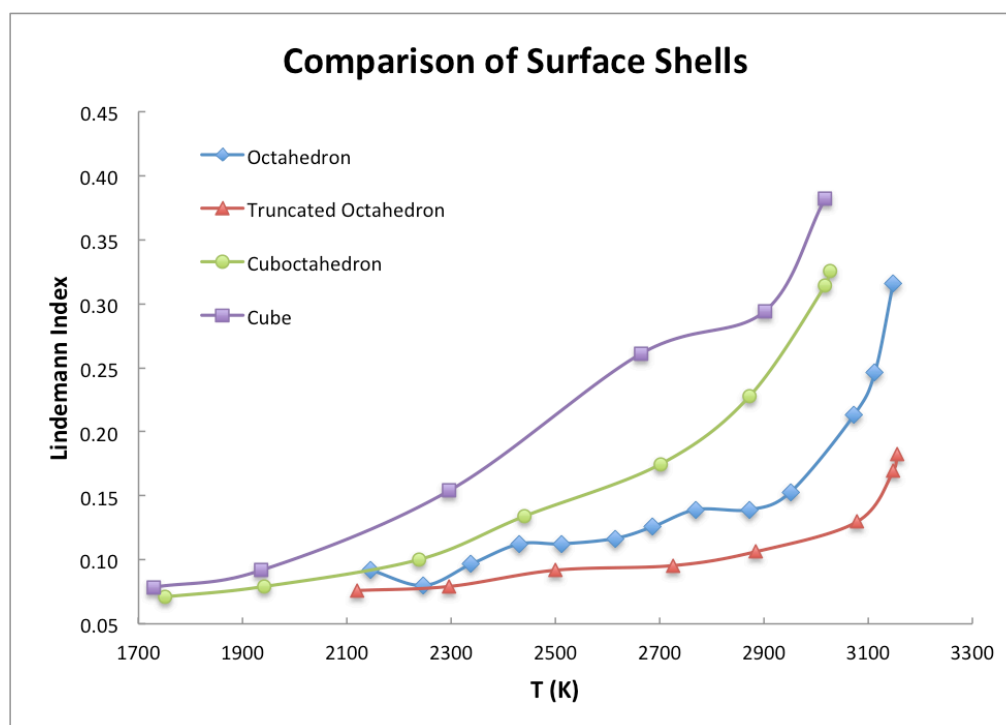


Figure 4-13. Plot of Lindemann index w.r.t temperature of the surface shells for all four shapes

4.4.3 Melting Temperature and Surface Reconstruction of Spherical Nanoparticle

For completeness, the melting of a spherical nanoparticle is simulated and compared to the four other shapes discussed above. The spherical nanoparticle is constructed by removing all atoms beyond a radius of 1.335 nm from a crystal lattice. It contains 1755 atoms, and is not a perfect sphere, but is instead a multi-faceted nanostructure consisting of both $\{111\}$ and $\{100\}$ surfaces, as shown in Figure 4-14 (a). Once again, dimerization of nitrogen atoms occurs on the $\{100\}$ facets, as indicated by the red-colored rectangles in Figure 4-14 (b).

A calculation of the cohesive energy per atom for the spherical nanoparticle gives a value of -6.2093 eV/atom; thus, it is expected to be more stable than the cuboctahedron, but less stable than the octahedron, as listed in Table 4-2. Such stability is again verified by similarly calculating the Lindemann index versus temperature curve for the spherical nanoparticle to determine its melting point. As seen from Figure 4-15, the upturning point of the Lindemann index curve for the spherical nanoparticle lies between cuboctahedron and octahedron, which makes it the third most stable shape among the five.

Thus, a general trend for melting temperature and cohesive energy is determined, proving that the surface energy of different crystallographic terminations is the key factor in determining the stability and melting temperature of a nanoparticle. Another significant mechanism is discovered in the MD simulation for lowering the ground state energy of a nanoparticle is surface reconstruction near the melting point, whereby the $\{100\}$ surface reconstructs into the most stable $\{111\}$ facet.

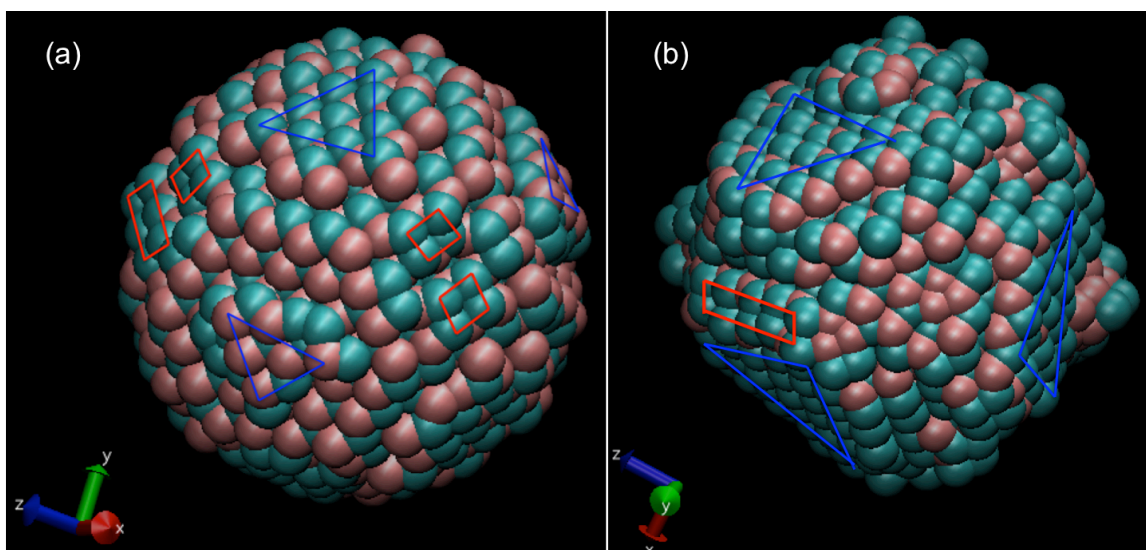


Figure 4-14. Surface reconstruction on c-BN spherical nanoparticle. Relaxation of the nanoparticle in microcanonical ensemble with an initial temperature of 2800K (a) the initial configuration showing $\{100\}$ and $\{111\}$ facets on surface: pink and green spheres denote boron and nitrogen respectively (b) reconstructed $\{111\}$ facet shown in blue triangle and dimerized pairs shown in red rectangle

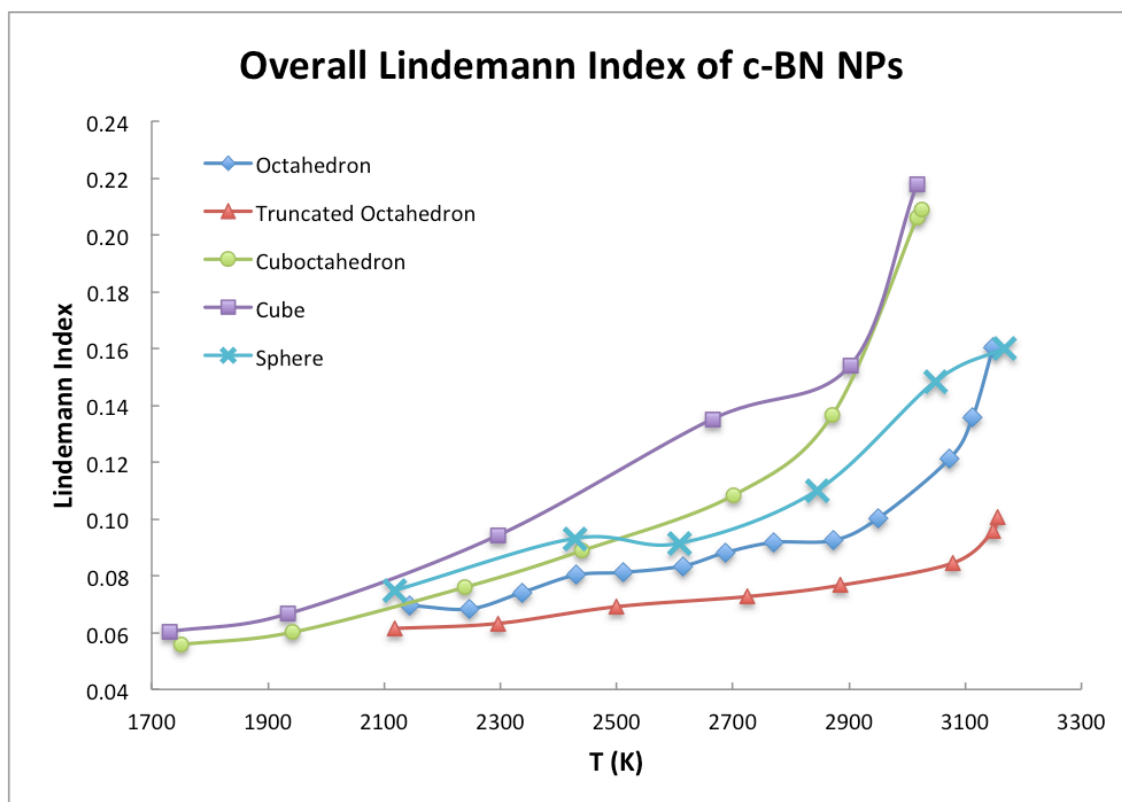


Figure 4-15. Plot of Lindemann index w.r.t. temperature for all five geometries, including the sphere

Table 4-2: Summary of cohesive energy and average coordination number of various shapes of c-BN nanoparticles

Geometry	Total number of atoms	Length (nm)	Average Coordination Number	Cohesive Energy (eV)
Cube	1728	2.08	3.5208	−5.9800
Cuboctahedron	1846	1.53	3.5872	−6.0928
Sphere	1755	2.67	3.6558	−6.2093
Truncated Octahedron	1592	0.89	3.6822	−6.2540
Octahedron	1771	2.55	3.7267	−6.3279

4.5 References

1. Cheng D, Wang W, Huang S. The onion-ring structure for pd-pt bimetallic clusters. *The Journal of Physical Chemistry B*. 2006;110(33):16193-16196.
2. Toshima N, Harada M, Yamazaki Y, Asakura K. Catalytic activity and structural analysis of polymer-protected gold-palladium bimetallic clusters prepared by the simultaneous reduction of hydrogen tetrachloroaurate and palladium dichloride. *J Phys Chem*. 1992;96(24):9927-9933.
3. Baletto F, Mottet C, Ferrando R. Molecular dynamics simulations of surface diffusion and growth on silver and gold clusters. *Surf Sci*. 2000;446(1):31-45.
4. Leonard BM, Bhuvanesh NS, Schaak RE. Low-temperature polyol synthesis of AuCuSn₂ and AuNiSn₂: Using solution chemistry to access ternary intermetallic compounds as nanocrystals. *J Am Chem Soc*. 2005;127(20):7326-7327.
5. Timp G, Howard R, Mankiewich P. Nano-electronics for advanced computation and communication. In: *Nanotechnology*. Springer; 1999:7-87.
6. Robbins MO, Grest GS, Kremer K. Effect of finite system size on thermal fluctuations: Implications for melting. *Physical Review B*. 1990;42(9):5579.

7. Liang L, Liu D, Jiang Q. Size-dependent continuous binary solution phase diagram. *Nanotechnology*. 2003;14(4):438.
8. Buffat P, Borel JP. Size effect on the melting temperature of gold particles. *Physical Review A*. 1976;13(6):2287.
9. Moon WH, Hwang HJ. A modified Stillinger–Weber empirical potential for boron nitride. *Appl Surf Sci*. 2005;239(3):376-380.
10. Mishima O, Era K. Science and technology of boron nitride. *Electric Refractory Materials*. 2000:495-556.
11. Kagamida M, Kanda H, Akaishi M, Nukui A, Osawa T, Yamaoka S. Crystal growth of cubic boron nitride using Li_3BN_2 solvent under high temperature and pressure. *J Cryst Growth*. 1989;94(1):261-269.
12. Wentorf Jr R. Cubic form of boron nitride. *J Chem Phys*. 1957;26(4):956-956.
13. Lian G, Zhang X, Zhu L, Tan M, Cui D, Wang Q. New strategies for selectively synthesizing cubic boron nitride in hydrothermal solutions. *CrystEngComm*. 2010;12(4):1159-1163.
14. Karlsson J, Larsson K. Hydrogen-induced de/reconstruction of the c-BN (100) surface. *The Journal of Physical Chemistry C*. 2010;114(8):3516-3521.
15. Osuch K, Verwoerd W. Surface reconstruction of cubic boron nitride (001). *Surf Sci*. 1993;285(1):59-65.
16. Chadi D. Atomic and electronic structures of reconstructed Si (100) surfaces. *Phys Rev Lett*. 1979;43(1):43.

Chapter 5

5 Melting of c-BN Octahedron Nanoparticles and Phase Separation during Melting

5.1 Introduction

We discuss the melting mechanism of c-BN nanoparticles by focusing on octahedral nanoparticles in this chapter, as it consists solely of the most stable $\{111\}$ facet. As shown in Chapter 4, the $\{100\}$ facet is unstable towards dimerization, and undergoes surface reconstruction into the $\{111\}$ facet at the onset of melting. Hence, the melting of non-octahedral nanoparticles will involve non-crystallographic dimer-stabilized $\{100\}$ facets, as well as reconstructed $\{111\}$ facets. In order to study the basic melting mechanism of c-BN nanoparticles without these additional complications, we therefore, choose to focus on the octahedron. This shape allows us to observe a remarkable phenomenon of concurrent phase separation and melting, and this prediction is seemingly corroborated in measurements of laser-heated c-BN particles. This phase separation in nanoparticles has been mentioned in Shirinyan and Wautelet's theoretically study¹, and it has also been observed in graphene boron-nitride nanotube systems^{2,3}.

5.2 Melting Mechanism of c-BN Nanoparticles and Concurrent Phase Separation during Melting

The detailed melting mechanism of octahedral nanoparticles with simultaneous phase separation is discussed in this section. First, the data is visualized by post-processing the MD simulation results in VMD at different time steps, which allows tracking the initiation and progress of melting, as well as the physical segregation of the boron and

nitrogen atoms throughout the melting process. This analysis allows clear observation of corner-initiated melting and phase separation that may occur. Two quantitative measures, i.e. the Lindemann index and the number of B-N, B-B, and N-N bonds, are also tracked as a function of time, with the results supporting our picture of corner-initiated melting. Finally, striking evidence of melting with phase separation, as predicted by the simulations, is obtained from complementary experiments of laser-heated c-BN particles, which was conducted by fellow members in Professor Tse's research group.

5.2.1 Simultaneous Phase Separation and Melting of c-BN Octahedron

A 2.04 nm octahedral c-BN nanoparticle containing 969 atoms is heated up to 3340K in MD simulation using the canonical ensemble (NVT). This temperature is about 100 degrees higher than the reported 3246K melting point of c-BN bulk crystals⁴. It is found that the melting starts from the vertex, and then propagates to an edge and surface, and finally proceeds gradually inwards. The hexagonal rings along the {111} direction of c-BN can be seen in Figure 5-1(a), with boron and nitrogen represented in red and yellow respectively. This octahedron has eight {111} facets with half being boron terminations and half-being nitrogen terminations, as displayed in the inset of Figure 5-1 (a). The six vertices have the same coordination number of 2. Melting starts with bonds breaking at the vertices, and at the 500 picosecond mark of the NVT simulation (Figure 5-1 (b)), half of the octahedron's corners are melted. Several boron-boron bonds have formed, resulting in small boron clusters at the corners, as shown in Figure 5-1 (b). Seven nitrogen atoms have vaporized from the nanoparticle, with a number of nitrogen atoms diffusing around the surface to form small clusters on the boron terminated surface, as displayed in the inset of Figure 5-1 (b). At the 1 nanosecond mark, melting has spread to

the edges and surfaces of the nanoparticle, with the c-BN nanoparticle losing its octahedral shape, as depicted in Figure 5-1 (c). The boron cluster inside the nanoparticle has clearly grown bigger at 2 nanoseconds, as depicted in Figure 5-1(d); and only half of the nanoparticle remains crystalline at 3 nanoseconds, as shown in Figure 5-1(e). At the 3.5 nanoseconds simulation mark, there are 130 vaporized nitrogen atoms, and a boron-rich nanoparticle with a nitrogen-rich shell is formed. The c-BN crystalline structure is no longer visible at this moment, as revealed in Figure 5-1(f). The concurrent occurrence of this phase separation phenomenon during melting is quite fascinating, with important implications for the melting mechanism of nanoparticles, as well as the sintering process for c-BN.

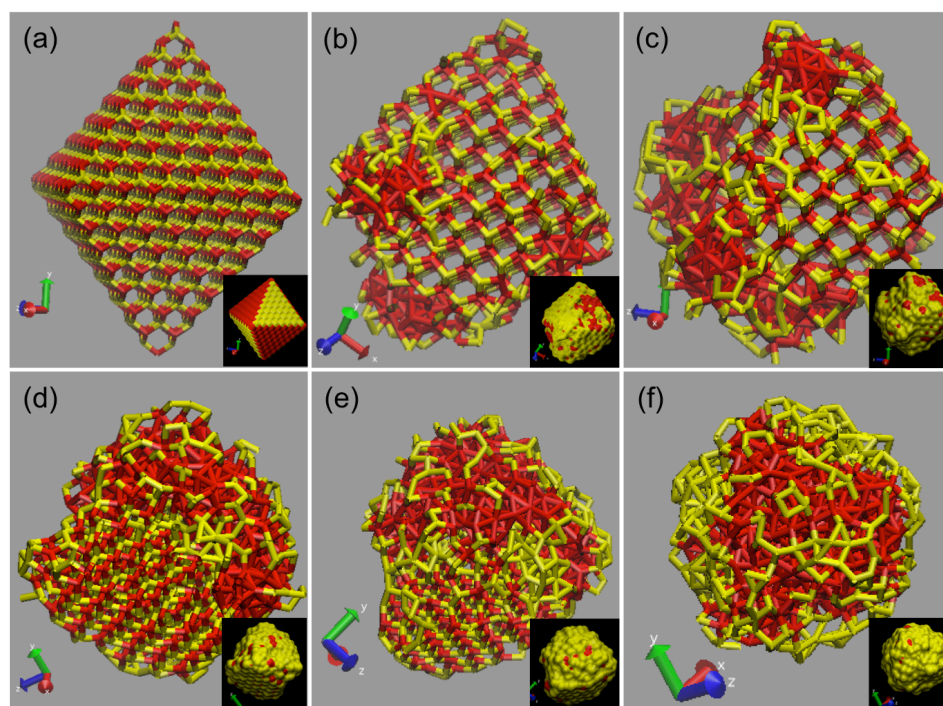


Figure 5-1. Phase separation happens during melting of 2.04nm octahedral c-BN nanoparticle in NVT simulation with $T=3340\text{K}$. Bond structure view on main graphics and surface atom view on insets (a) the initial configuration: red represents boron, and yellow represents nitrogen (b) 500ps simulation time: melting starts from corners and small phase separated boron clusters formed (c) 1ns simulation time: melting proceeds to edges (d) 2ns simulation time: melting propagates to surfaces and the boron clusters tend to unite (e) 3ns simulation time: more than half of the nanoparticle is melted (f) 3.5ns simulation time: no crystalline c-BN is visible and phase separated boron clusters have formed in the interior of the nanoparticle.

5.2.2 Qualitative Monitoring of Phase Separation & Corner-initiated Melting

Melting of octahedral c-BN nanoparticles has been evinced. Here, melting starts from the corners and then spreads to edges and surface, in contrast to the well-known surface melting mechanism of spherical nanoclusters where melting starts from the surface resulting in an amorphous/liquid shell that propagates inwards and forms a liquid shell-solid core coexisting structure^{5,6}. Although this corner-initiated melting mechanism of octahedral c-BN nanoparticles is different than traditional surface melting behavior, it can still be quantitatively monitored by calculating the Lindemann index of different shells comprising the nanoparticle. For spatial analysis of the phenomenon, each c-BN nanoparticle is divided into four regions or concentric shells: (1) a surface shell, (2) a next outer shell, (3) an inner shell, and (4) a core shell. The neighbor list of each atom at every picosecond is constructed, and the average Lindemann index of each shell is calculated. The upper graph of Figure 5-2 presents the Lindemann index values of the different shells as a function time of this c-BN nanoparticle. The value of the core shell does not increase much until 1ns, while the values of the other three shells increases steadily from the onset. At 3.5 nanoseconds, the Lindemann index value of every shell exceeds 0.1, viz. there is 10% of bond fluctuation, implying that the whole nanoparticle is melted or phase separated and no longer crystalline. This threshold is in agreement with the generic Lindemann index value of 0.08–0.15 used to determine melting for simple solids^{6,7}. We track the total number of B-N bonds, B-B bonds, and N-N bonds as presented in the lower graph of Figure 5-2. The number of B-N bonds continuously decreases due to bond breaking, while the numbers of B-B bonds and N-N bonds continuously increase. This trend supports the concept of phase separation occurring

concurrently with melting for the c-BN nanoparticle. A corresponding experimental study of laser heating of c-BN powders to assess melting phenomena is conducted. Transmission electron microscopy (TEM) of c-BN powder after laser treatments seems to show phase separation of boron particles, similar to that predicted by the simulations. The details are discussed in the following section.

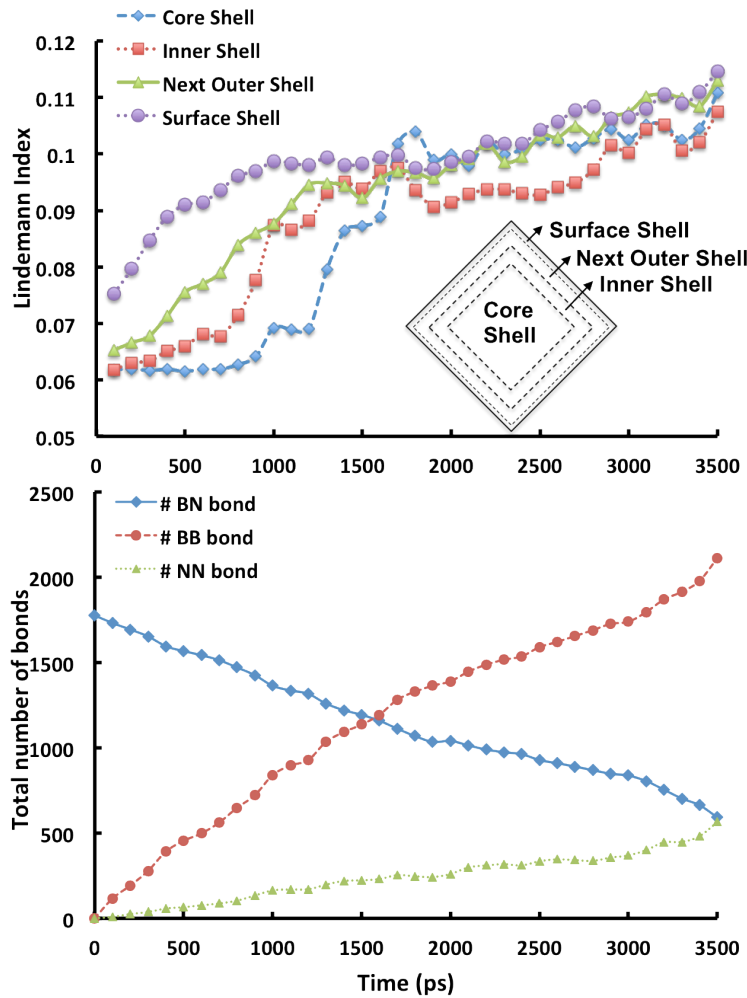


Figure 5-2. The Lindemann index of each shell of the 2.04nm octahedral c-BN nanoparticle and the total number of B-N, B-B, and N-N bonds in NVE simulation with initial $T=3340\text{K}$.

5.2.3 Laser treatment of c-BN powders for validation of phase separation

To assess the MD prediction of concurrent phase separation during melting of c-BN, a laser experiment is designed to heat up and melt c-BN nanoparticles. The samples are then characterized with TEM to see if phase segregation is exhibited. The second harmonic (532 nm) of a Quanta-Ray Nd:YAG laser operating at 10 Hz is employed to irradiate the c-BN powders in an inert Ar atmosphere. The laser power is set to 20mJ/pulse with 10ns pulse width (full width at half maximum), when there is no visible plasma formation. TEM image, **Figure 5-3 (a)**, of c-BN particles before the laser heating shows that some of the c-BN particles are approximately ~100 nm in size. The inset shows the selected area electron diffraction (SAED) pattern, which confirms the single crystalline structure of pre-treated c-BN. After laser treatment, phase separation may be inferred because of the presence of boron particles (~50-100 nm diameters) divulged in the TEM imaging, as displayed in **Figure 5-3 (b)**. From the SAED pattern of the boron particles, inset of **Figure 5-3(b)**, the indexed spots with d -spacings of 4.40 Å, 3.75 Å and 2.47 Å match very well with the reflections from the {200}, {111} and {311} planes of tetragonal boron, respectively. In addition, formation of c-BN particles with non-monocrystalline nanostructured features, not present in the initial powder, can be found in the post-heated powder, as revealed in **Figure 5-3(c)**. The SAED pattern (inset of **Figure 5-3(c)**) confirms that it is polycrystalline cubic boron nitride. These results seem to indicate that the original c-BN particles have been reconstructed, rather than have been vaporized and condensed back onto the powder, which would likely take on discrete nanoparticle form. There does exist the possibility that the intense laser heating vaporized the c-BN powder into B and N atoms, with B clusters condensing back on the

target powder. Further investigation by turning down the laser fluence such that there is no spectroscopic B emission from the gas phase should better clarify the issue. Nevertheless, the experimental data provide evidence that the MD results for phase separation during melting of c-BN nanoparticles may be possible.

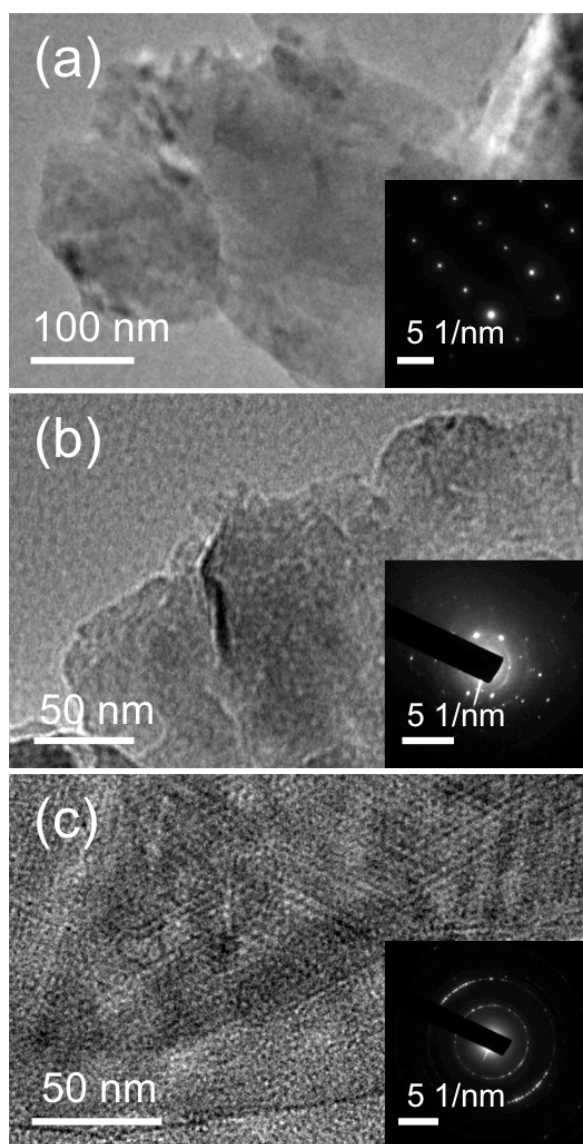


Figure 5-3. (a) Top-view TEM image of c-BN particles before laser treatment; inset shows the SAED pattern revealing its single-crystal feature. (b) TEM image of the phase separated boron particles after the laser treatment; inset shows the corresponding SAED pattern. (c) TEM image of the nanostructured c-BN, with polycrystalline structure after laser treatment as revealed by its SAED pattern in the inset. (These results were provided by Zhizhong Dong and Gang Xiong in Prof. Tse's group).

5.3 Definition of Melting Point

An intermediate-sized octahedron nanoparticle with a side length of 2.55 nm and containing 1771 atoms is chosen for investigating melting point behavior. First, a computationally efficient NVE simulation of the 2.55 nm octahedral c-BN nanoparticle in the temperature range from 2200 K to 3500 K is conducted, in increments of 100 K. The octahedral nanoparticle is relaxed in NVE for 3 nanoseconds after each initial temperature. Next, the Lindemann index of the entire nanoparticle is calculated and plotted with respect to the final temperature of the nanoparticle in Figure 2-1 to define the melting temperature. Afterwards, a series of computationally intensive NVT simulations is performed to test our estimate of the melting temperature. The details are discussed in the following two sections.

5.3.1 Estimate of Melting Point Using Lindemann Index

A bond-length fluctuation indicator, i.e. Lindemann index, is employed to monitor the melting behavior of c-BN nanoparticles. In the MD simulations, melting starts from the vertices to the edges and surfaces and then gradually proceeds inwards; we call this, corner-initiated melting. Various parameters of each shell are determined, from the surface to the core, to better understand the melting phenomenon by extracting the information from the trajectory results of MD NVE simulations. At every picosecond, the neighbor list for each atom is constructed, and the local bond stretch value of each atom is measured, as given in Equation 5-1. Then, the total bond stretch value for each shell (given in Equation 4-2) is calculated, Equation 4-2 along with the Lindemann index of each shell (given in Equation 5-3). Here, r_{ic} represents the distance from a single atom to

the centroid of the whole nanoparticle. The temperature for each shell (given in Equation 5-4) is also recorded every 1 picosecond.

$$\text{Equation 5-1: } \delta_i = \sqrt{\frac{1}{n_i} \sum_{j=1}^{n_i} \frac{r_{ij}^2}{a^2}}$$

$$\text{Equation 5-2: } \delta_{sh} = \sqrt{\frac{1}{N_{sh}} \sum_{i=1}^{N_{sh}} \left(\frac{1}{n_i} \sum_{j=1}^{n_i} \frac{r_{ij}^2}{a^2} \right)}$$

$$\text{Equation 5-3: } \gamma_{sh} = \sqrt{\frac{1}{N_{sh}} \sum_{i=1}^{N_{sh}} \frac{(|r_{ic}| - \langle |r_{ic}| \rangle_t)^2}{a^2}}, \langle |r_{ic}| \rangle_t = \frac{\sum_{t=1}^{time} |\vec{r}_i - \vec{r}_c|}{time}$$

$$\text{Equation 5-4: } T_{sh} = \frac{\sum_{i=1}^{N_{sh}} m_i (v_{xi}^2 + v_{yi}^2 + v_{zi}^2)}{3k_B N_{sh}}$$

As explained in Chapter 4, the onset of melting is estimated as the temperature at which the Lindemann index starts to upturn, specifically when the Lindemann index deviates by more than 5% from its low-temperature linear behavior. The Lindemann indices of the entire nanoparticle, the surface shell, as well as that of the inner three shells are plotted as a function of temperature; and as will be shown below, all three plots upturn at the same temperature.

Figure 2-1 shows the three different plots (the surface shell, the inner three shells, and the overall nanoparticle) of the Lindemann index for the 2.55 nm octahedral c-BN nanoparticle. The Lindemann index initially increases linearly from about 2150K to 2950K, as the vibrational motion of the atoms increases with increasing kinetic energy. At the onset of melting, the Lindemann index exhibits nonlinear behavior, jumping up,, as the boron-nitrogen bonds at the vertices start to break, along with boron clusters beginning to form. In addition, part of the contribution to Lindemann index is from the nitrogen atoms diffusing around on the surface of the nanoparticle, as well as from the interior to the surface due to vaporization of surface nitrogen atoms. Above 2950K, the

Lindemann index starts to exhibit non-linear behavior, with the deviation exceeding 5% at 3000K, as shown in Figure 5-5. Therefore, 3000K is estimated for the onset of melting. Since the value of the Lindemann index for the entire nanoparticle at 3000K is 0.11, this value for melting is consistent with the general rule-of-thumb for Lindemann index values of 0.08–0.15 that are used to demarcate melting for simple solids^{3,4}.

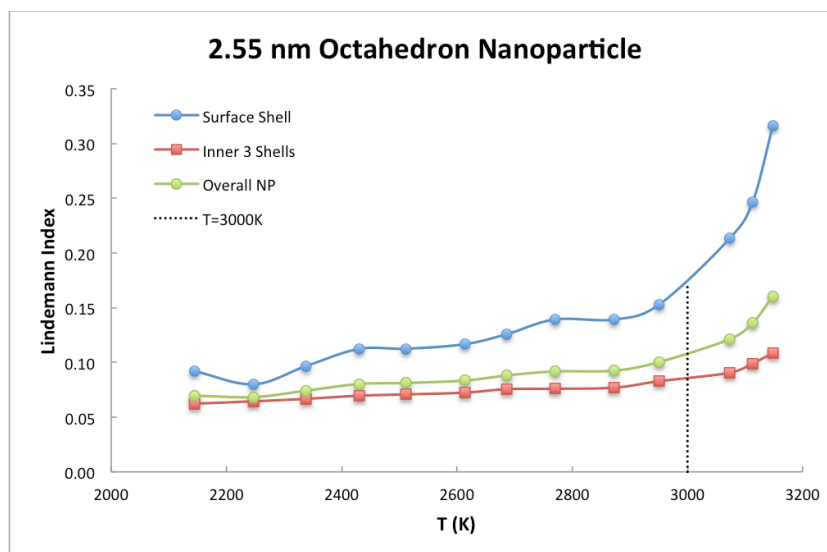


Figure 5-4. Lindemann index of 2.55 nm octahedral c-BN nanoparticle w.r.t. temperature.

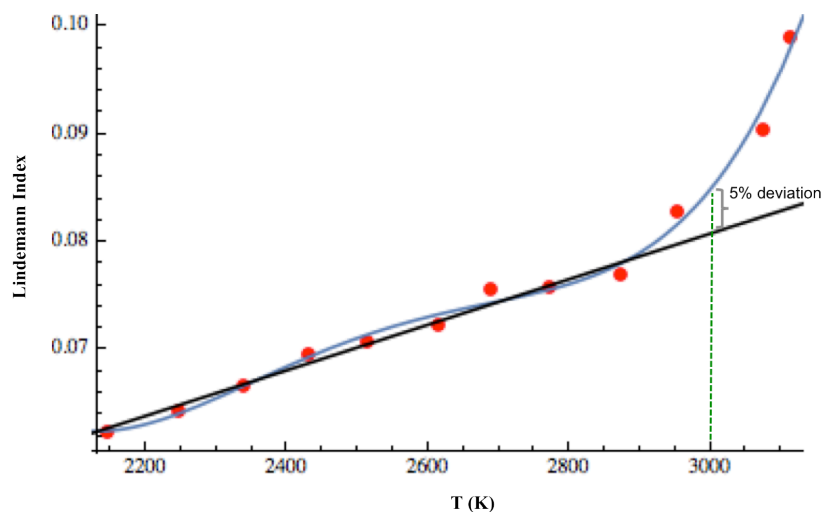


Figure 5-5. Linear fitting from the Lindemann index values of inner three shells of 2.55 nm octahedral c-BN nanoparticle shown as red dots.

Applying the same criteria of 5% deviation from the low-temperature linear behavior for the other three c-BN nanoparticle sizes of 2.04 nm, 3.57 nm and 4.59 nm, the estimated onset of melting is obtained at 2890K, 3090K, and 3090K, respectively, as indicated in Figure 5-6, Figure 5-7, and Figure 5-8. The details of the melting dynamics will be discussed in a later section on the size-dependence of the melting temperature.

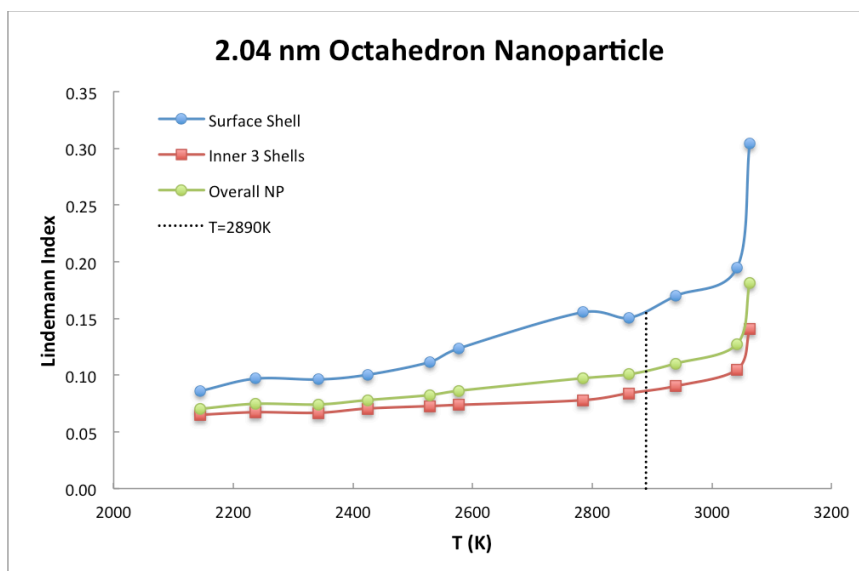


Figure 5-6. Lindemann index of 2.04 nm octahedral c-BN nanoparticle w.r.t. temperature.

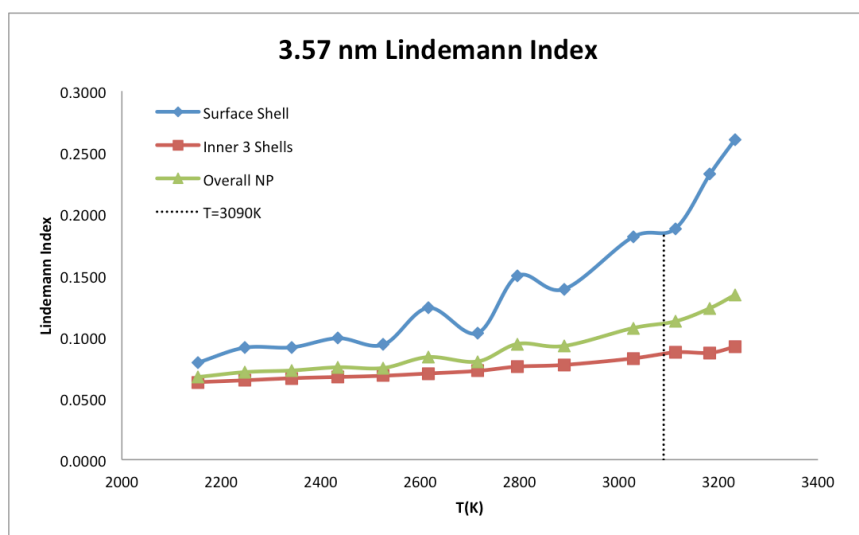


Figure 5-7. Lindemann index of 3.57 nm octahedral c-BN nanoparticle w.r.t. temperature.

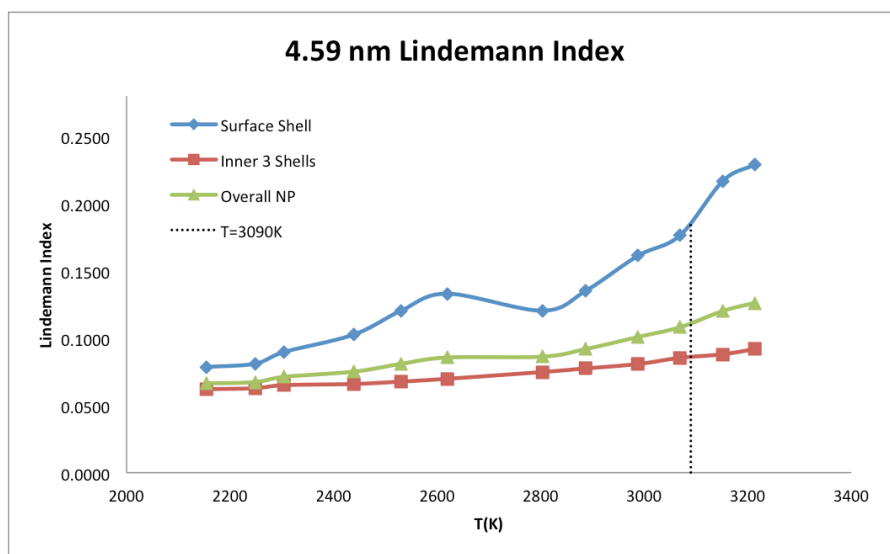


Figure 5-8. Lindemann index of 4.59 nm octahedral c-BN nanoparticle w.r.t. temperature.

5.3.2 Estimate of Melting Point Using Caloric Curve and Specific Heat

To verify our estimate of the melting temperature, a series of computationally-intensive NVT simulations for the 2.55 nm nanoparticle in the temperature range of 2618 K to 3218 K are performed, in increments of 100 K, from which the specific heat behavior is calculated. The NVT simulation at each temperature is stopped when the core of the octahedron nanoparticle starts melting. Otherwise, it terminates at 50 nanoseconds of simulation time with a time step of 0.1 femtosecond, if the core remains crystalline at lower temperatures. The total energy versus temperature from the simulation results is plotted in the upper chart of Figure 5-9. A discontinuity of the caloric curve is found to occur between 2918K and 2968K, indicating that phase transition is occurring. We would like to see the behavior of the heat capacity as a function of temperature, and we calculate it in two different ways to validate the phase transition. First, the derivative from the total energy as a function of temperature, i.e. $C(T) = dU/dT$, is computed, and it is shown as the green curve in the lower chart of Figure 5-9. Second, employing the fluctuation-

dissipation theorem, the specific heat is calculated from the fluctuation of the total energy, i.e. $C(T) = (U - \langle U \rangle)^2 / k_B T^2$, as plotted by the red curve in the lower chart of Figure 5-9. Both curves have peaks indicating the occurrence of a phase transition. Furthermore, the peaks of the curves indicates that the phase transition happens at about 2950 K, which is close to where the Lindemann index curve starts to upturn. Therefore, we are confident that the estimate of the melting point from the computationally-efficient NVE simulation provides an upper limit of the temperature at which the entire octahedral c-BN nanoparticle will melt when thermodynamic equilibrium is achieved.

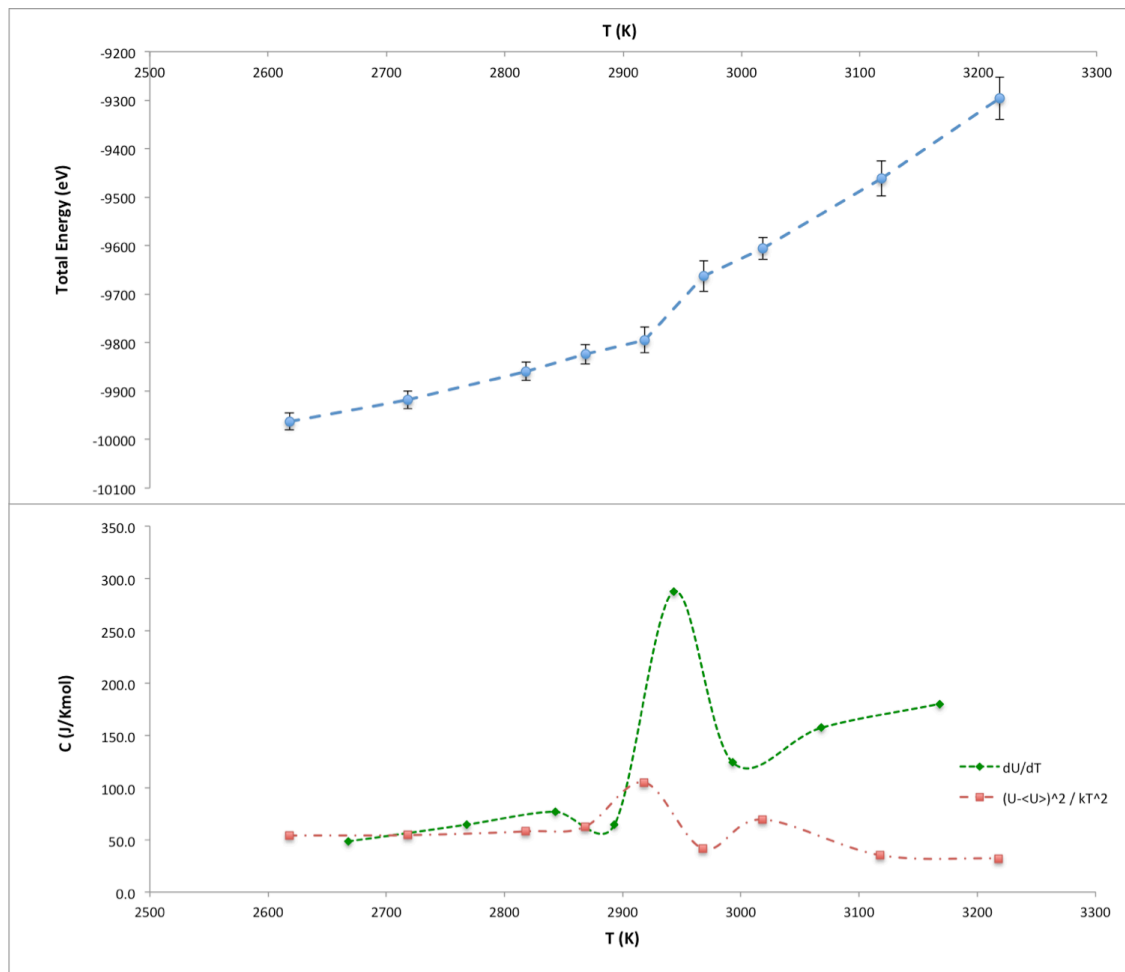


Figure 5-9. The caloric curve of the 2.55nm octahedral c-BN nanoparticle has a jump, and the plots of the specific heat show that melting occurs at approximately 2950K.

5.4 Size Dependence of Melting Point of Octahedral c-BN Nanoparticles

The size-dependence of octahedral nanoparticles is discussed in this section. Nanoparticle geometry is the main factor that affects the melting temperature, which reasonably agrees with theoretical models that include geometric considerations.

5.4.1 Size Dependence of Melting Point of Octahedral c-BN Nanoparticle

We use the computationally-efficient method of 3 nanosecond-NVE simulations and calculation of the Lindemann index of the octahedral c-BN nanoparticles to study the size dependence of the melting point. There are four different sized octahedral c-BN nanoparticles discussed in this section, i.e. 2.04 nm (969 atoms), 2.55 nm (1771 atoms), 3.57 nm (4495 atoms), and 4.59 nm (9139 atoms). All of them are cut to where half of the facets are boron termination and half are nitrogen terminations, with the same configuration of edges and corners. Figure 5-10 displays the overall cluster Lindemann index of the four nanoparticles with respect to temperature. The curve of the 2.04 nm nanoparticle starts to upturn at the lowest temperature, followed by the 2.55 nm nanoparticle. The difference between the 3.57 nm and 4.59 nm nanoparticle is not significant. For completeness, we also plot the Lindemann index of the surface shell, as well as the average Lindemann index of the inner three shells (Figure 5-11), to confirm the initiation of melting throughout the entire nanoparticle. Notably, there is a visible suppression of the surface shell Lindemann index near the onset of melting, as shown in Figure 5-12, which is due to surface reconstruction. We will discuss this aspect further in detail below. Using the 5% deviation point from linear behavior of the Lindemann index curve of the inner 3 shells as an estimate, the upper limits of the melting points are

determined for each octahedral nanoparticle size, as represented by red diamonds in Figure 5-13. The results are compared with several models of melting point depression.

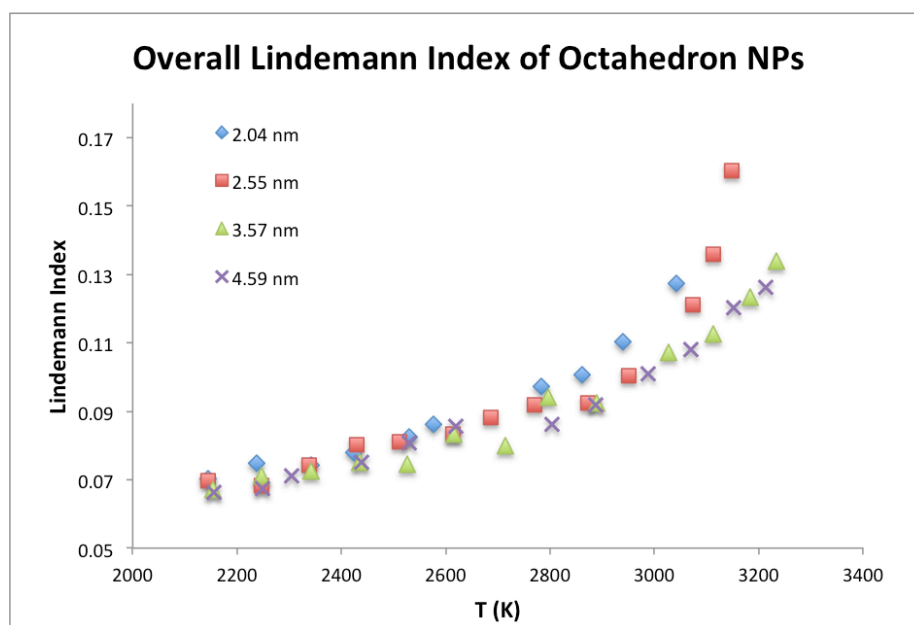


Figure 5-10. The Lindemann index of the overall nanoparticle versus temperature of varied-sized octahedral c-BN nanoparticles. The melting points are determined by the 5% deviation point from the low-temperature linear behavior.

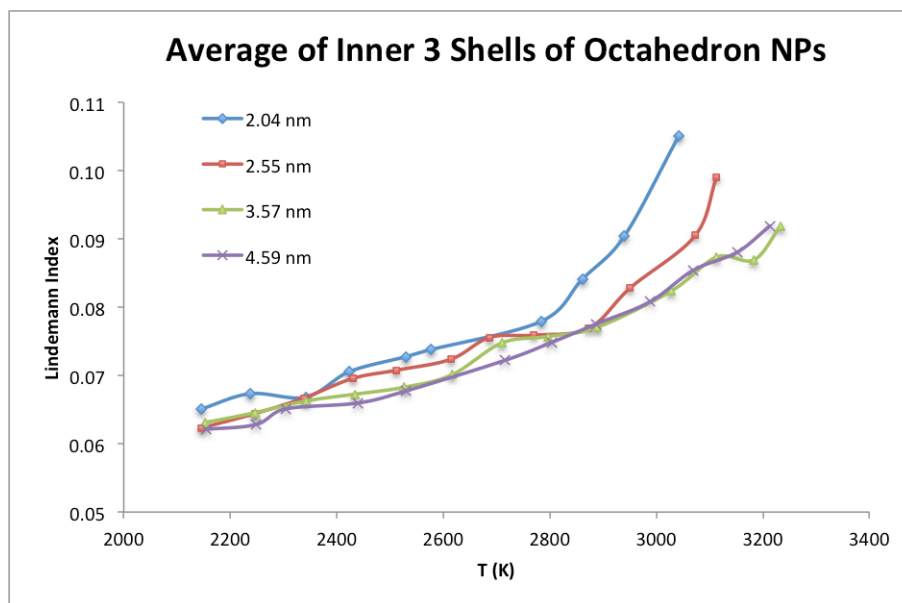


Figure 5-11. The Lindemann index of the inner three shells versus temperature of varied-sized octahedral c-BN nanoparticles. The melting points are determined by the 5% deviation point from the low-temperature linear behaviour..

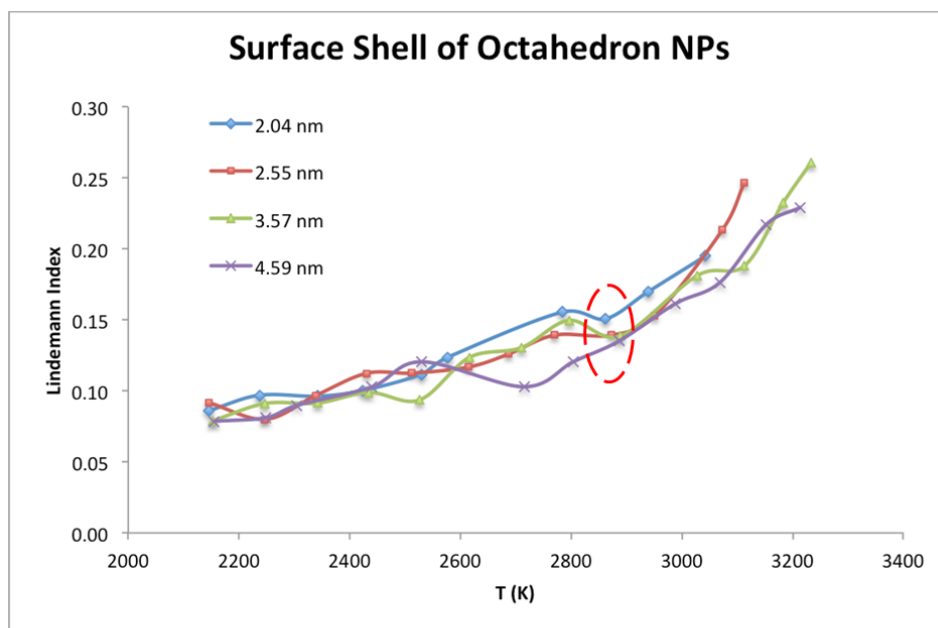


Figure 5-12. The Lindemann index of the surface shell versus temperature of varied-sized octahedral c-BN nanoparticles. Notice that there is a suppression of the Lindemann index near the onset of melting for all the sizes, indicated by the red dashed circle.

From our study, we know that the nanoparticle shape affects the melting point, so the traditional liquid drop or liquid-shell models are not suitable anymore. Instead, models considering coordination number⁸, cohesive energy⁹, and geometric factors¹⁰ can better describe the size dependence of octahedral c-BN nanoparticles. We measure the average coordination number of the nanoparticles and obtain the calculated melting points shown as black crosses in Figure 5-13. This method overestimates the melting temperature of the 2.04 nm, but fits our result for the 2.55 nm, 3.57 nm and 4.59 nm nanoparticles fairly well. In addition, we measure the cohesive energy of the octahedral nanoparticles and c-BN bulk crystals at the corresponding melting points, and the calculated melting temperatures form a lower bound, which is shown as blue bars in Figure 5-13. If we calculate the cohesive energy at 0 K, then the calculated melting temperatures are identical to the average coordination number model. Finally, we make

use of the Wautelet model¹⁰ that considers different geometries, including spherical, cubic, and octahedral among others. The calculated melting points shown as green circles in Figure 5-13, provides the best match to our results.

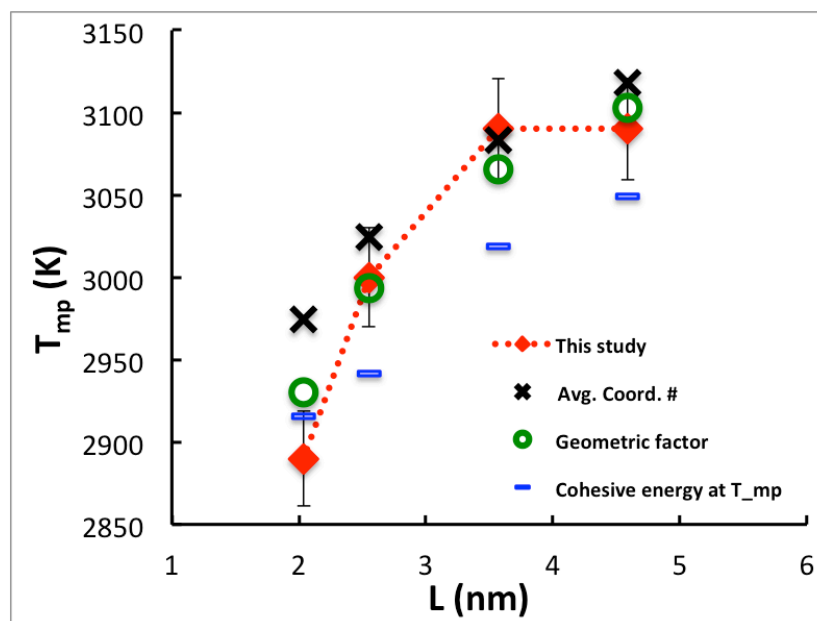


Figure 5-13. Size dependence of the melting point of octahedral c-BN nanoparticles with 1% error bars included, and the predictions from several melting point depression models.

5.5 Surface Reconstruction Near Onset of Melting

The Lindemann index of the surface shell, Figure 5-12, shows an interesting suppression of fluctuation for octahedral nanoparticles of all the sizes at a temperature slightly below their estimated melting temperatures. By visualizing the simulation results in VMD, we observe that surface reconstruction effects occur near the onset of melting for 2.04 nm, 2.55 nm, and 2.57 nm here, thereby stabilizing the octahedral nanoparticle, as reflected in the suppression of the Lindemann index. This effect is exactly the same phenomenon of surface reconstruction stabilizing the nanoparticle that we had observed earlier in the

melting of the cube nanoparticle, discussed in Chapter 4. Thus it is very satisfying to observe the same mechanism at work in nanoparticles of different shapes and sizes.

In Figure 5-14 to Figure 5-17, the VMD visualized results are displayed of the nanoparticles slightly below their melting temperature. NVT simulations are carried out on three of the smallest sizes, i.e. 2.04 nm, 2.55 nm, and 3.57 nm, over a temperature range of about 2600K to 3200K. NVT simulations are not conducted for the 4.59 nm nanoparticle because it contains about 10,000 atoms, which is too computationally expensive. Instead, the NVE simulation result is presented, which reveals the same mechanism at work.

All four nanoparticles exhibit the previously-discussed corner-initiated melting mechanism, along with surface reconstruction to some extent. The two smaller nanoparticles exhibit more extensive surface reconstruction. Figure 5-14 and Figure 5-15 for the 2.04 nm and 2.55 nm nanoparticles, respectively, both divulge the formation of a nitrogen dimer-stabilized $\{100\}$ facet at the edge between the two $\{111\}$ facets of an octahedron, as well as vertices that have completely melted. In comparison, the two larger nanoparticles show slightly less reconstruction. The edges have yet to melt and reconstruct, but the vertices have re-formed into nitrogen dimer-stabilized $\{100\}$ facets. Extensive nitrogen diffusion on the boron-terminated $\{111\}$ facets is also observed.

Therefore, taken together, these four results suggest that the melting process of octahedral c-BN nanoparticles starts with corner-initiated melting and reconstruction into nitrogen dimer-stabilized $\{100\}$ facets, together with extensive nitrogen diffusion on boron-terminated surfaces. This stage is then followed by melting of the edges with formation of dimer-stabilized $\{100\}$ facets between $\{111\}$ facets. Finally, complete

melting is marked by full phase separation of the boron and nitrogen, as discussed in the sections above. We point out that this surface reconstruction results in the formation of a truncated octahedron, which is most obviously discerned from the two larger nanoparticles. This outcome is in complete agreement with the melting results of the cube, which also reforms into a truncated octahedron-like structure composed of a mixture of dimerized $\{100\}$ faces and reconstructed $\{111\}$ faces, prior to complete melting, as illustrated in **Figure 5-18**. This theoretical result has actually been observed experimentally by Mishima and Era¹¹, which is given in **Figure 5-19**. To the best of our knowledge, this is the first time such a result for c-BN nanoparticles has been reported using an MD approach.

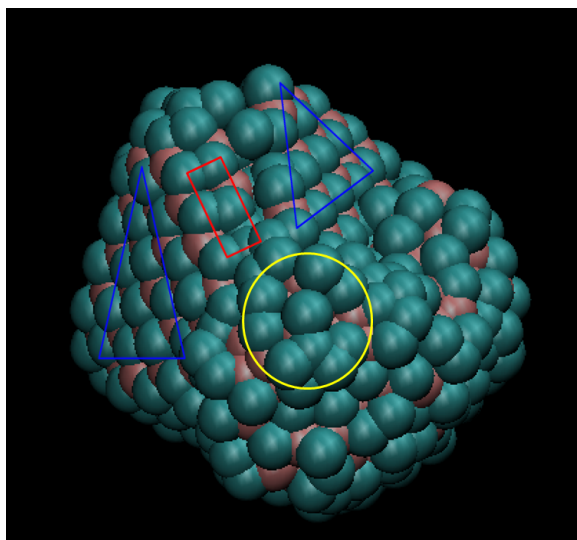


Figure 5-14. 2.04 nm octahedron in NVT simulation with $T=2840\text{K}$ for 50ns. The red rectangular area shows the dimerized $\{100\}$ face in between two blue triangular areas of $\{111\}$ faces. The vertex is melted shows in yellow circled area.

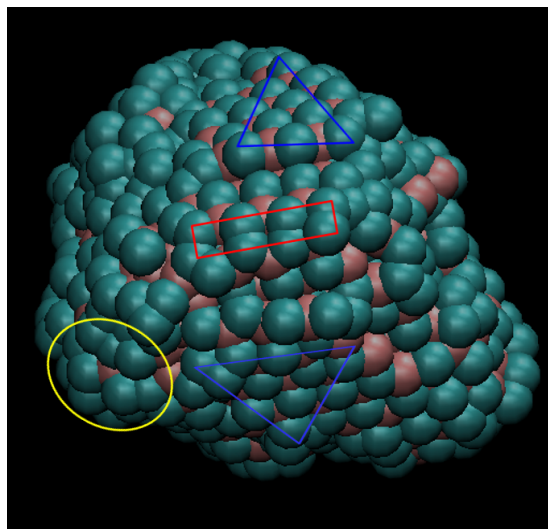


Figure 5-15. 2.55 nm octahderon in NVT simulation with $T=2968\text{K}$ for 40ns. The red rectangular area shows the dimered $\{100\}$ face in between two blue triangular areas of $\{111\}$ faces. The vertex is melted shows in yellow circled area.

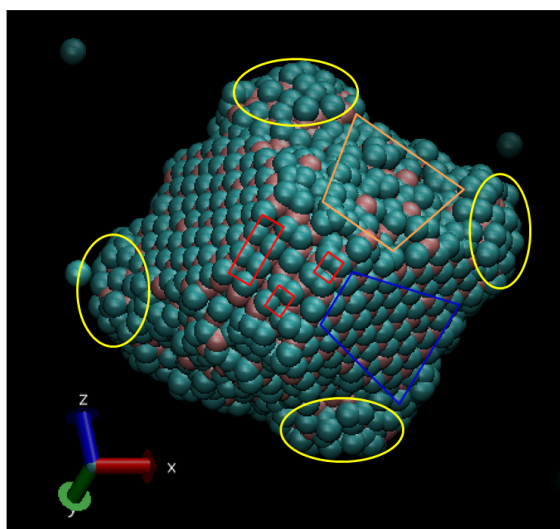


Figure 5-16. 3.57 nm octahderon in NVT simulation with $T=3076\text{K}$ for 42ns. The red rectangular areas show the dimered $\{100\}$ face in between the $\{111\}$ faces. The vertice are melted shows in yellow circled area.

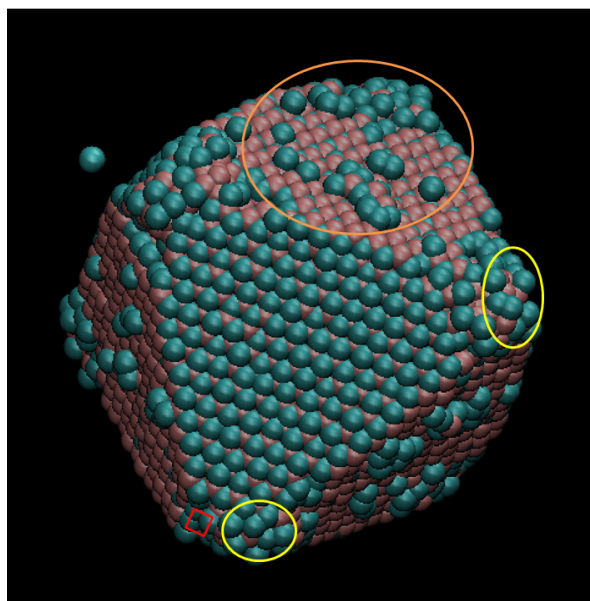


Figure 5-17. 4.59 nm octahedron in NVE simulation with initial $T=3500\text{K}$ for 3ns. The vertex are melted shows in yellow circled area and nitrogen atoms diffuse around on boron facets.

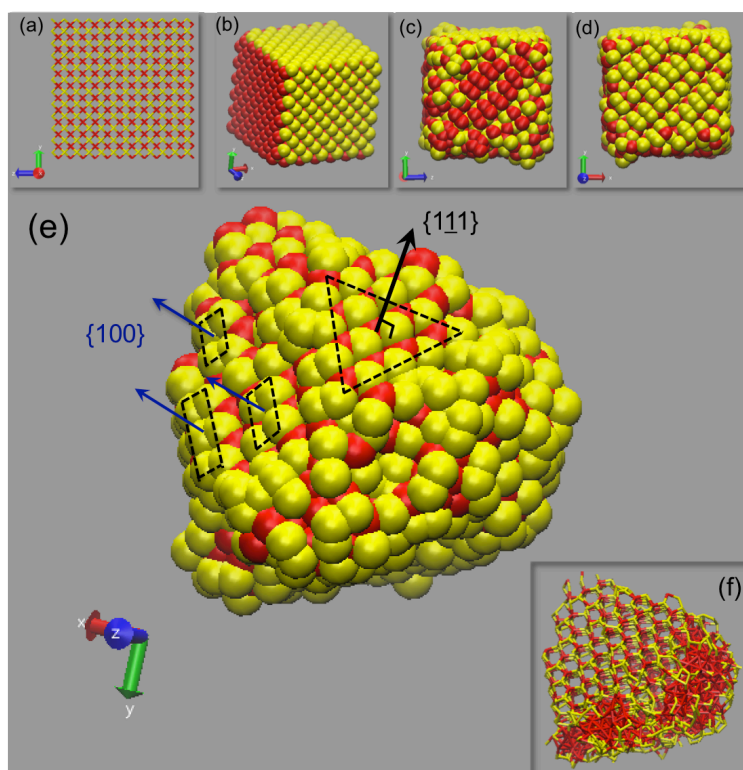


Figure 5-18. Surface reconstruction on c-BN $\{100\}$ facets. Relaxation of the cubic nanoparticle in microcanonical ensemble with an initial temperature of 2400K (a) the initial configuration shown as bond structure seen from $\{100\}$ direction (b) 0ps: red and yellow spheres denote boron and nitrogen, respectively (c) 10ps: dimerized boron pairs on $\{100\}$ facet (d) 10ps: dimerized nitrogen pairs on $\{001\}$ facet (e) 2700ps: reconstructed $\{111\}$ facet and dimerized $\{100\}$ facets on the surface of cube nanoparticle (f) 2700ps: the same orientation as (e) but shown as bond structure.

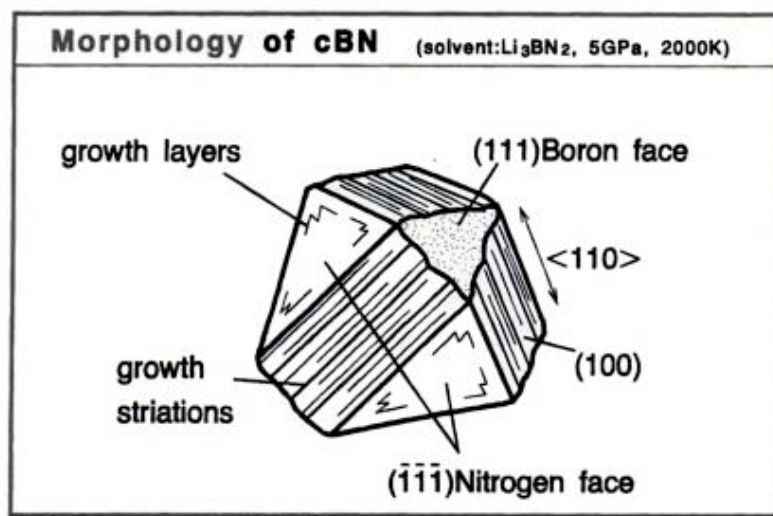


Figure 5-19. Morphology of c-BN clusters (reproduced from [11]).

5.6 References

1. Shirinyan A, Wautelet M. Phase separation in nanoparticles. *Nanotechnology*. 2004;15(12):1720.
2. Suenaga K, Colliex C, Demoncey N, Loiseau A, Pascard H, Willaime F. Synthesis of nanoparticles and nanotubes with well-separated layers of boron nitride and carbon. *Science*. 1997;278(5338):653-655.
3. Wu J, Han W, Walukiewicz W, et al. Raman spectroscopy and time-resolved photoluminescence of BN and $B_xC_yN_z$ nanotubes. *Nano letters*. 2004;4(4):647-650.
4. Madelung O, Rossler U, Schulz M. Boron nitride (BN), melting point, debye temperature density, entropy, etc., cubic modification. In: *Group IV elements, IV-IV and III-V compounds. part b - electronic, transport, optical and other properties*. Vol 41A1b. Springer Berlin Heidelberg; 2002:1-8.
5. Baletto F, Mottet C, Ferrando R. Molecular dynamics simulations of surface diffusion and growth on silver and gold clusters. *Surf Sci*. 2000;446(1):31-45.
6. Neyts EC, Bogaerts A. Numerical study of the size-dependent melting mechanisms of nickel nanoclusters. *The Journal of Physical Chemistry C*. 2009;113(7):2771-2776.
7. Koparde VN, Cummings PT. Sintering of titanium dioxide nanoparticles: A comparison between molecular dynamics and phenomenological modeling. *Journal of Nanoparticle Research*. 2008;10(7):1169-1182.

8. Safaei A, Shandiz MA, Sanjabi S, Barber Z. Modeling the melting temperature of nanoparticles by an analytical approach. *The Journal of Physical Chemistry C*. 2008;112(1):99-105.
9. Shandiz MA, Safaei A, Sanjabi S, Barber Z. Modeling the cohesive energy and melting point of nanoparticles by their average coordination number. *Solid State Commun*. 2008;145(9):432-437.
10. Wautelet M, Dauchot J, Hecq M. On the phase diagram of non-spherical nanoparticles. *Journal of Physics: Condensed Matter*. 2003;15(21):3651.
11. Mishima O, Era K. Science and technology of boron nitride. *Electric Refractory Materials*. 2000:495-556.

Chapter 6

6 Sintering of c-BN Octahedron Nanoparticles

6.1 Introduction

The sintering of two solid nanoparticles is a complicated process involving long reaction kinetic times^{1,2}; and occasionally, phase transitions can be involved during the sintering process³. The high melting temperature and covalent bonding of c-BN makes it even more complex and difficult to sinter, but several experimental groups have managed to successfully sinter c-BN powders^{4,5}. However, a careful theoretical study of c-BN nanoparticles and its sintering process is still lacking in the community. Such study would also aid in the understanding of agglomeration and aggregation in the gas-phase synthesis of c-BN nanopowders. Based upon the results we obtained from studying the melting of c-BN nanoparticles, we performed MD simulations to investigate the temperature dependence of coalescence and/or aggregation of free c-BN nanoclusters. In this thesis, we are interested in the sintering of c-BN {111} facets as we have demonstrated it to be the most stable surface. Mishima and Era reported the twinned structure of c-BN⁶ stacking on {111} facets. Tian et al. also synthesized the nanotwinned c-BN bulk samples, with Knoop hardness of 77.7 GPa⁷.

First, particle-particle collisions of c-BN octahedral nanoparticles are studied statistically to gain a basic understanding of the collision-orientation and sintering behavior. Computationally intensive MD simulations (50 ns for each case) of the sintering of c-BN octahedral nanoparticles in isolated environments are conducted to evaluate the optimal temperature range for sintering.

6.2 Statistical Study of Particle-Particle Collision

The sintering process of two equal-sized octahedron c-BN nanoparticles of 2.55 nm are examined, with a starting gap between the two nanoparticles at around 3 nm. The first nanoparticle is denoted as NP1 and is on the left, as shown in Figure 3-1. The second nanoparticle is placed on the right side and is denoted as NP2. In order to simulate the particle-particle collision statistically, NP1 & NP2 are placed in NVE conditions and NP2 is rotated randomly. NP2 is first rotated along the z-axis with an angle of θ_1 , and is then rotated again along the new x-axis with an angle of θ_2 . A set of 100 randomly rotated NP1 and NP2 pairs are created, and Figure 6-2 shows the distribution of the randomly rotated angles. The melting temperature of the 2.55 nm octahedron c-BN nanoparticle is around 3000 K, according to the discussion in Chapter 4, the set of 100 randomly rotated pairs is simulated at three temperatures below the melting point and at one temperature above the melting point. The initial temperatures for the NVE simulation are: 2500 K, 2700 K, 2900 K, and 3100 K. The results of the nanoparticle dynamics at each initial temperature are discussed in the flowing sections.

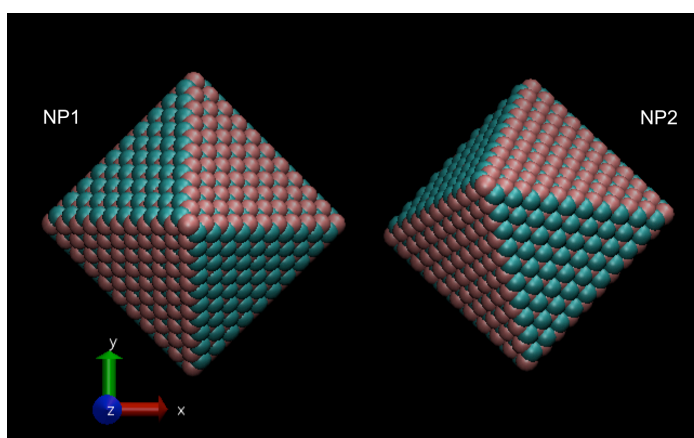


Figure 6-1. Two octahedral c-BN nanoparticles with the same size for simulation of particle-particle collision.

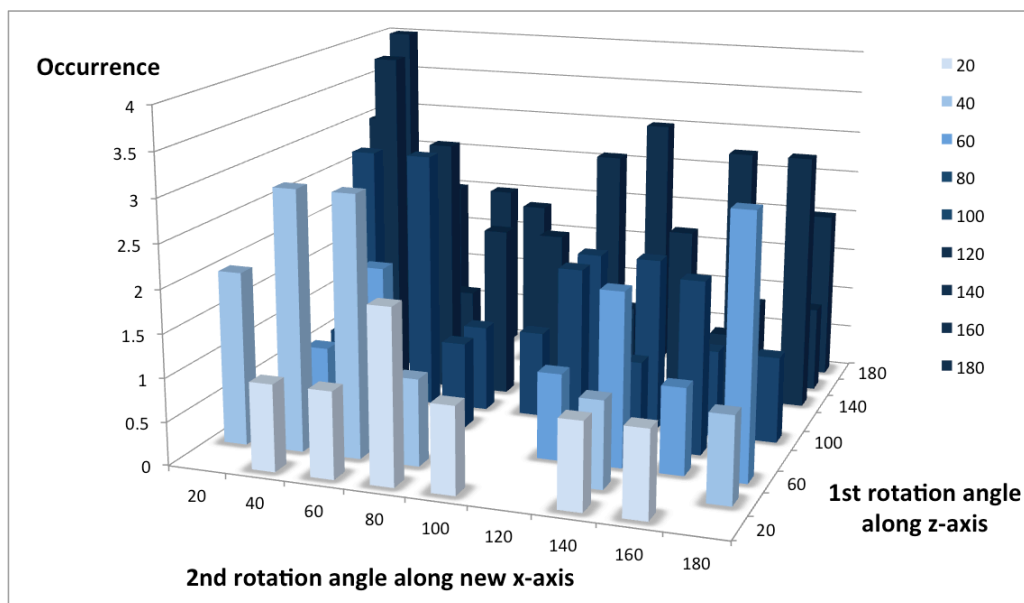


Figure 6-2. 100 sets of random rotation angles for initial orientations of NP2.

6.2.1 Initial Temperature of 2500 Kelvin

The 100 cases of randomly rotated octahedron nanoparticles are placed in an MD box with sufficient vacuum space so that they are separated initially and isolated in a gas phase. Periodic boundary conditions are imposed. After 3 ns of simulation in MD with NVE conditions, the change in kinetic energy is recorded, and the nanoparticles at the instance of collision are examined using VMD. When the two nanoparticles collide, new bonds are formed at the interface, causing a gain in potential energy. Due to energy conservation in the NVE microcanonical ensemble, internal kinetic energy then increases as the potential energy drops. Therefore, the temperature of whole system rises once the two nanoparticles come into contact and start forming bonds with each other. Figure 6-3 shows a special case where the surfaces gradually merge after collision. NP2 is rotated along z-axis by 83° , then along the new x-axis by 47° , as displayed in Figure 6-3(a). Figure 6-3(b) shows the initial collision of a vertex of NP2 with a edge of NP1; and the

unstable contact turns into a boron-boron facet contact as displayed in Figure 6-3(c). Figure 6-3(d) and (e) show the gradual sliding and merging of the two boron-terminated surfaces of NP1 and NP2. We term this a boron-boron collision case. The kinetic energy has a sudden jump of about 35 eV at the point of collision, and then increases gently with the merging of the two nanoparticles, as displayed in Figure 6-4, with a total increase in kinetic energy (ΔKE) of about 52 eV. Since this collision is contact between two boron surfaces, a boron-boron grain boundary is formed at the end of the 3ns simulation as displayed in Figure 6-5.

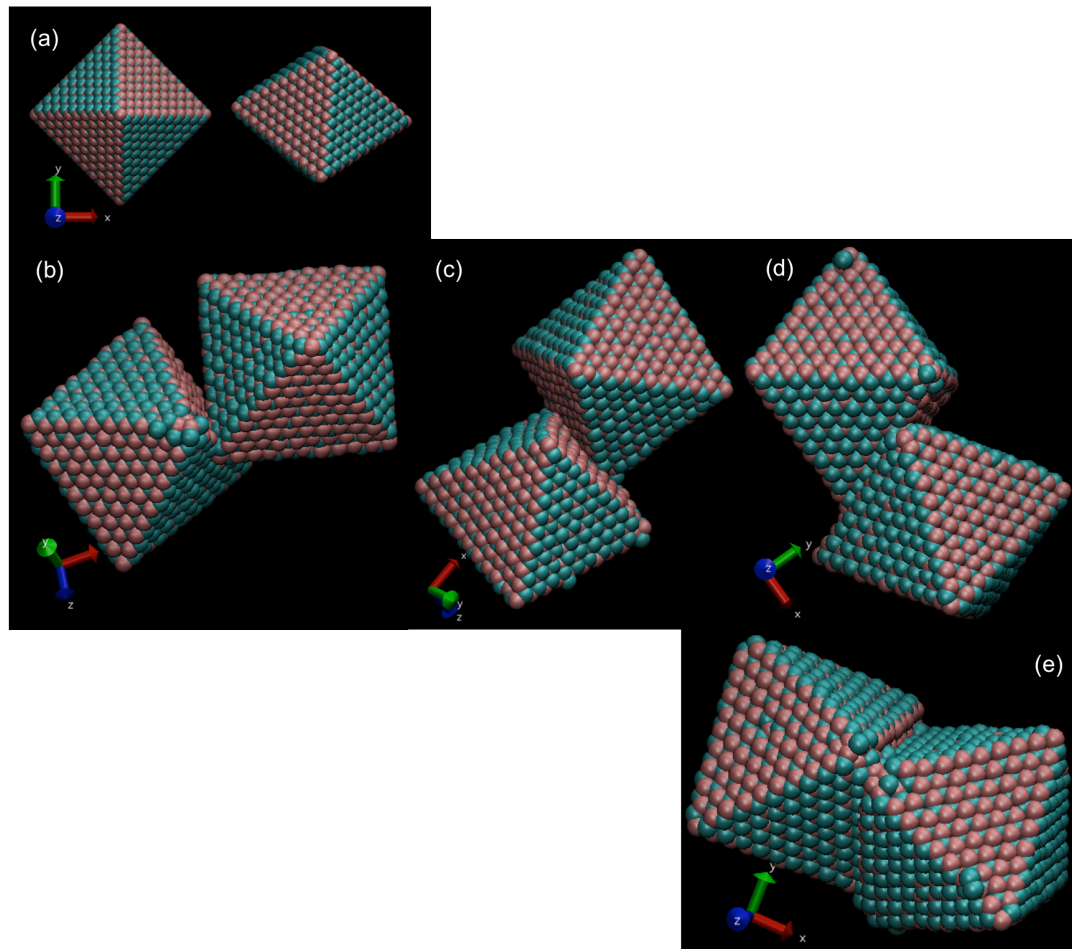


Figure 6-3. Two Octahedron c-BN nanoparticle in MD NVE simulation with initial temperature of 2500K. (a) 0 ps: red and green spheres denote boron and nitrogen respectively (b) 70 ps: tip hitting edge (c) 75 ps: boron facet in contact with another boron facet (d) 80 ps: surface sliding and merging (e) 500 ps: reaching the maximum contact surface area.

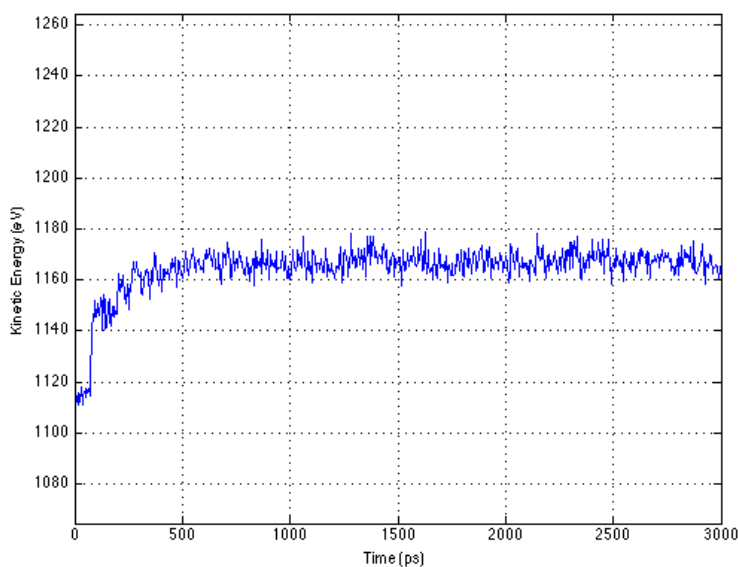


Figure 6-4. The kinetic energy as a function of time showing the boron-boron collision case in 2500K.

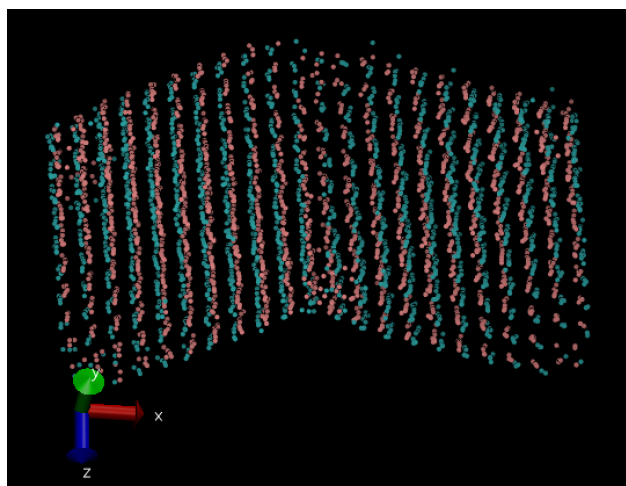


Figure 6-5. Boron-boron grain boundary at the contact interface.

We next introduce a boron-nitrogen collision case as presented in Figure 6-6. NP2 is rotated along z-axis by 53° , then along the new x-axis by 118° , as displayed in Figure 6-6 (a). Figure 6-6 (b) shows the tip of NP2 hitting the corner of NP1 at 73 ps, forming an unstable bond. The weakly-bonded nanoparticles wobble, and then one edge of NP1 collides and bonds to the boron-terminated facet of NP2 at 80 ps, as exhibited in Figure

6-6(c). However, this edge-to-facet bonding is still unstable; and at 82 ps, as revealed in Figure 6-6(d), a nitrogen-terminated facet of NP1 finally comes in contact with NP2, forming a nitrogen-boron interface. At 90 ps, Figure 6-6(e), there is almost complete facet-to-facet contact between the two nanoparticles. From the 90 ps mark until the end of the simulation at 3-ns, as exhibited in Figure 6-6(f), nitrogen atoms continue diffusing around the surface. Figure 6-7 shows the increase of kinetic energy (ΔKE) as a function of time, and the total increase of about 72 eV is the largest increase in kinetic energy among all the boron-nitrogen cases. This collision of nitrogen-boron facets appears as nice grain growth, as shown in Figure 6-8.

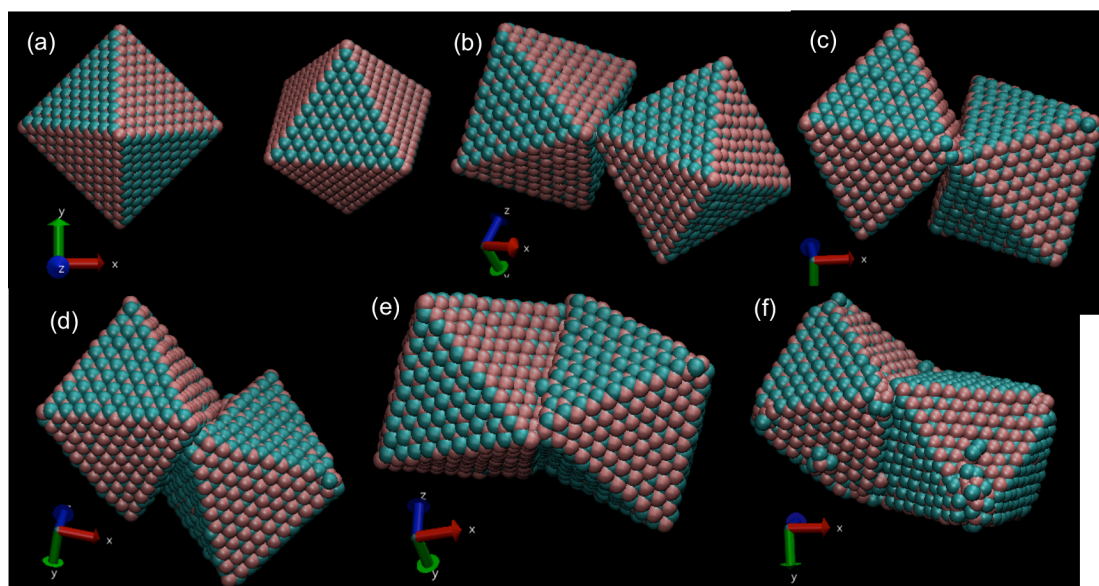


Figure 6-6. Boron-nitrogen collision in NVE with initial temperature of 2500K. (a) 0 ps: red and green spheres denote boron and nitrogen respectively (b) 73 ps: tip hitting corner (c) 80 ps: edge in contact with boron facet (d) 82 ps: nitrogen facet in contact with boron facet (e) 90 ps: sliding and merging (f) 3 ns:some atoms diffusing around the surface and formed small clusters on the surface.

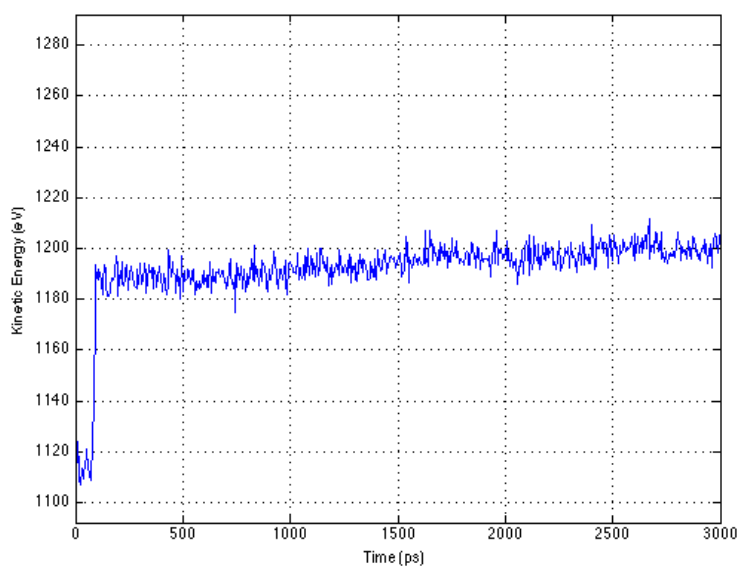


Figure 6-7. The kinetic energy as a function of time showing the nitrogen-boron collision case in 2500K.

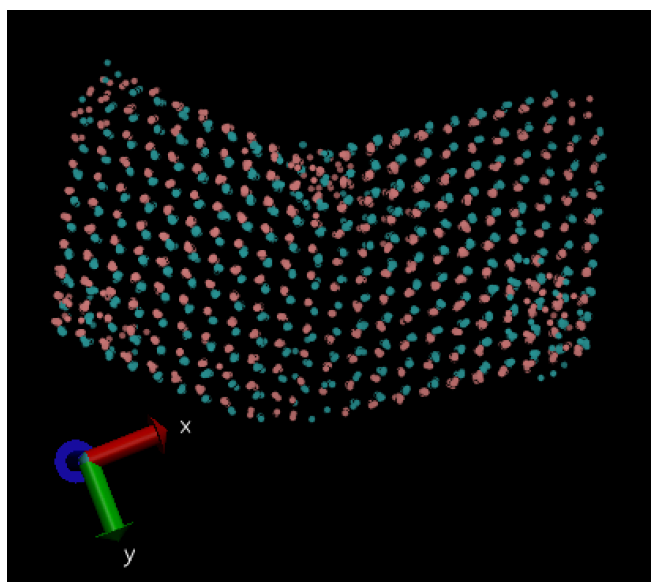


Figure 6-8. Grain growth at the interface of nitrogen-boron collision.

Finally, we do a quantitative study of all the 100 cases simulated in NVE conditions with initial temperature of 2500 K. The ΔKE from the 100 collisions is plotted in Figure 6-9, and a bi-modal result is obtained. Among the 100 collisions, there are 52 cases of boron-nitrogen (B-N) contact, 43 cases of boron-boron (B-B) contact, and only 5

cases of nitrogen-nitrogen (N-N) contact. The ΔKE for BN collisions is shown in Figure 6-10, and the peak occurs in the ΔKE range between 11 and 20 eV. The ΔKE for B-B collisions is given in Figure 6-11, and the peak occurs in the ΔKE range between 61 and 70 eV. Therefore, the bi-modal curve in Figure 6-9 arises from B-N collisions with a low ΔKE peak, and B-B collisions with a high ΔKE peak.

Simple probability suggests that there should be 50 B-N cases, and 25 B-B cases and N-N cases. However, since the proper sintering of NP1 and NP2 after initial collision requires the formation of stable bonds, there will therefore be a larger number of B-N and B-B cases because the B-N bond has a binding energy of -3.58 eV, and the B-B bond has a binding energy of -2.27 eV, as displayed in Figure 6-12. In comparison, the N-N bond has the weakest binding energy of -2.11 eV among the three, and is highly unstable at these high temperatures, as evidenced by the large nitrogen diffusion observed. Therefore, a dominance of B-N and B-B collisions is detected. At the not-too-high temperature of 2500K, there is a large gain in potential energy for B-B collisions, as B-B bonds are still stable that temperature. Since the unit cell of elemental boron is a 12-boron icosahedra⁸, there is a large coordination number for boron, and hence a correspondingly large gain in bond potential energy is available for B-B. However, as will be shown later, this collision orientation is not stable at higher temperatures.

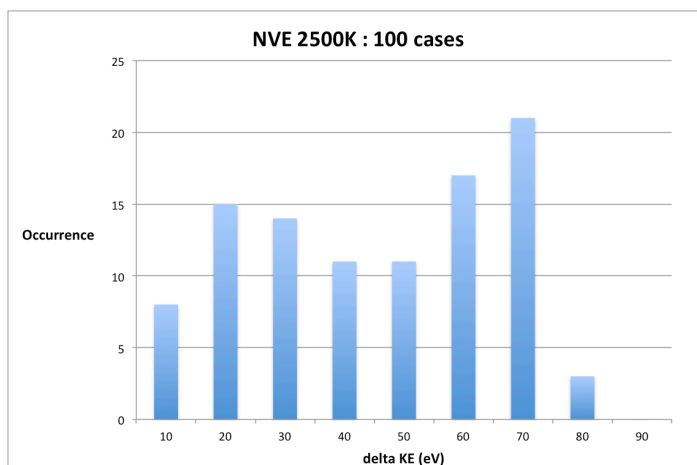


Figure 6-9. Statistics of change in kinetic energy from 100 collision cases in NVE 2500K.

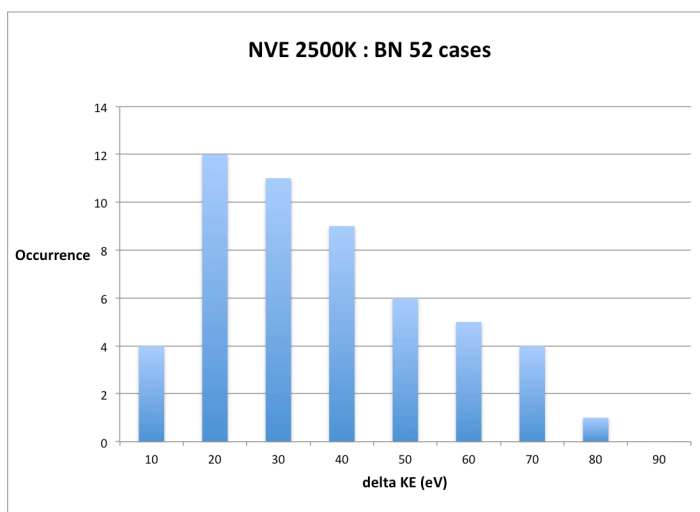


Figure 6-10. Statistics of change in kinetic energy from BN collision cases in NVE 2500K.

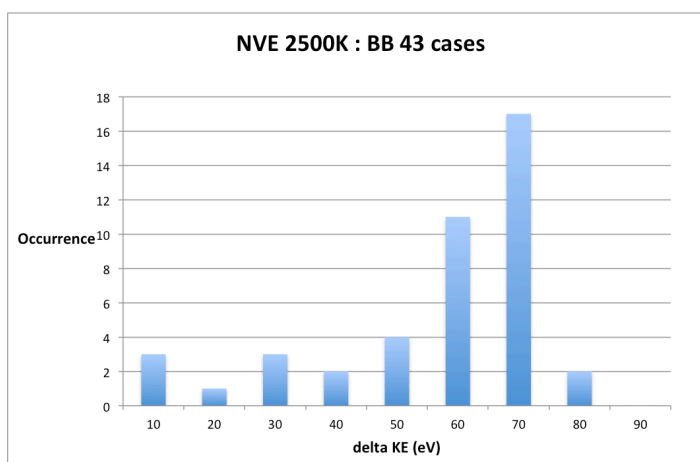


Figure 6-11. Statistics of change in kinetic energy from BB collision cases in NVE 2500K.

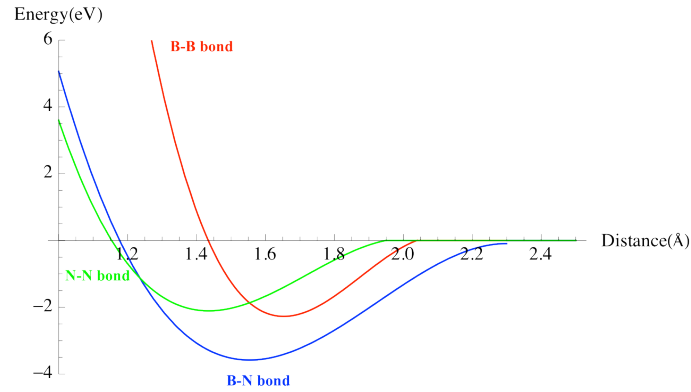


Figure 6-12. Binding energies of B-N, B-B and N-N bonds.

6.2.2 Comparison of Various Initial Temperature

NVE simulations at 2700 K, 2900 K, and 3100 K are also performed, and the total number of N-N cases is extremely low (4 or 5) at each temperature because of the unstable nature of N-N bonds at high temperatures. Boron-boron collision is much more favorable than nitrogen-nitrogen collision due to the higher binding energy of B-B bonds, as indicated in Figure 6-12. This aspect is reflected in the difference of the surface energy between the boron-terminated $\{111\}$ facet and the nitrogen-terminated $\{111\}$ facet, as presented in Table 6-2. The energy analysis in Chapter 4 assumes that half the facets are boron termination and half are nitrogen termination, with an average value of $-2.1240 \text{ eV}/\text{\AA}^2$. Here, for further investigation of particle-particle collision, the surface energy of $\{111\}$ facet (γ_{111}) is $-2.2342 \text{ eV}/\text{\AA}^2$ for boron facet, and the surface energy of $\{111\}$ facet (γ_{111}) $-2.0138 \text{ eV}/\text{\AA}^2$ for nitrogen facet, while there is no difference between $\{100\}$ facets of boron and nitrogen.

Figure 6-13, Figure 6-14, and Figure 6-15 show the ΔKE for all 100 cases, the B-N cases, and the B-B cases, respectively. Figure 6-13 reveals that the bi-modal distribution becomes less pronounced as temperature increases from 2500 K to 3100 K.

Also, the peak on the right side shifts lower while the left peak remains at 20 eV. The distribution of ΔKE in the B-B cases becomes more uniform as temperature increases (Figure 6-15), and the total number and average ΔKE of B-B cases also decrease as the temperature rises (Table 6-1). In Figure 6-14, the distribution of ΔKE and the average ΔKE of B-N cases for each temperature does seem not change much, but the total number of B-N cases at each temperature increases along with the rise of temperature. This result indicates that the B-B bond becomes less stable as temperature increases, while the B-N bond remains stable; hence the number of B-B cases decreases while the number of B-N cases increases.

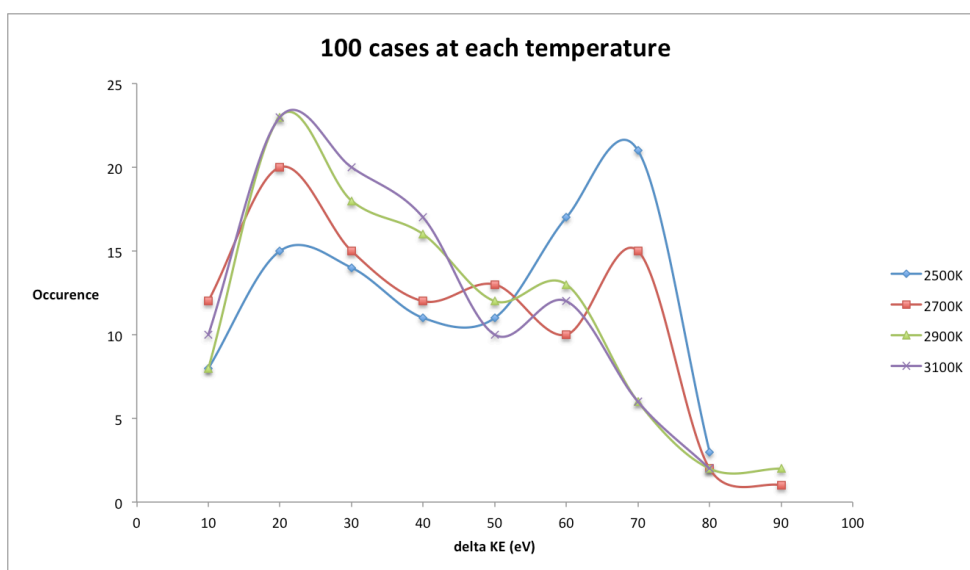


Figure 6-13. Statistics of change in kinetic energy from 100 collision cases at each temperature.

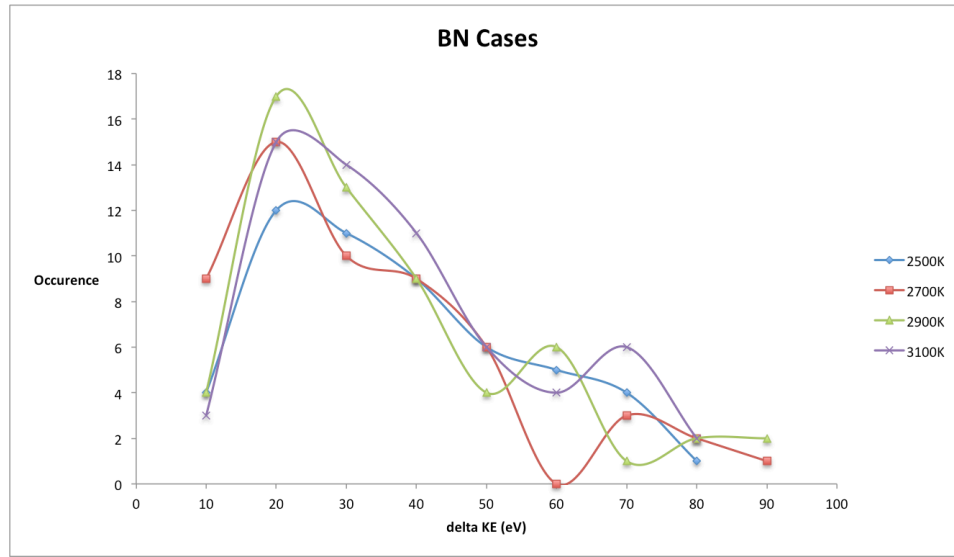


Figure 6-14. Statistics of change in kinetic energy from BN collision cases at each temperature.

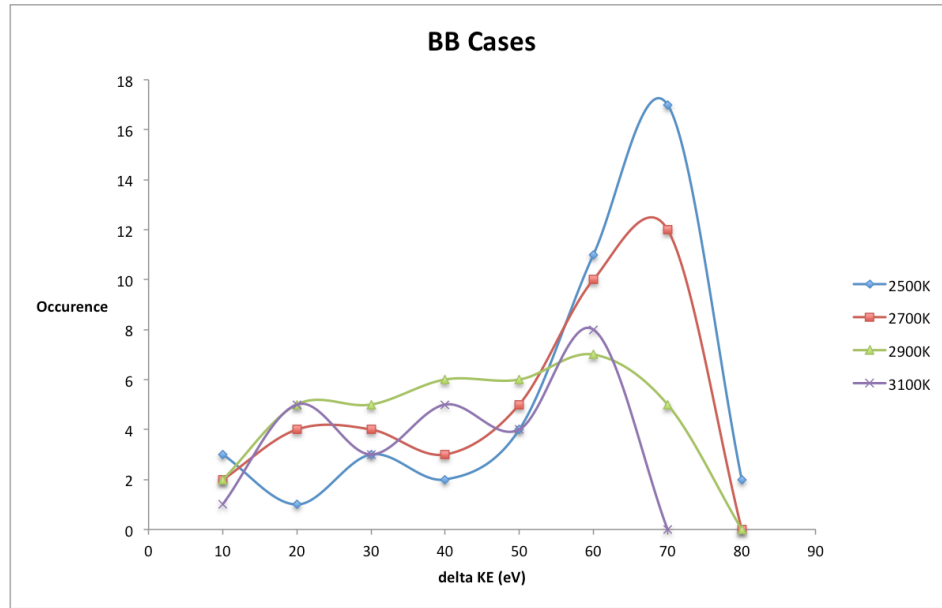


Figure 6-15. Statistics of change in kinetic energy from BB collision cases at each temperature.

Table 6-1. Comparison of particle-particle collision at various temperatures.

Temperature	# BN	# BB	# NN	Average ΔKE of 100 cases	Average ΔKE of BN cases	Average ΔKE of BB cases	Average ΔKE of NN cases
2500 K	52	43	5	40.59	32.65	51.63	28.20
2700 K	55	40	5	36.15	28.82	47.28	27.80
2900 K	60	36	4	33.96	30.90	39.08	33.75
3100 K	70	26	4	31.99	30.94	36.92	18.25

Table 6-2. Surface energy of {100} & {111} facets with boron or nitrogen termination.

Facet	Boron termination (eV/Å ²)	Nitrogen termination (eV/Å ²)	Half boron-half nitrogen (eV/Å ²)
{100}	$\gamma_{100} = -1.0438$	$\gamma_{100} = -1.0438$	$\gamma_{100} = -1.0438$
{111}	$\gamma_{111} = -2.2342$	$\gamma_{111} = -2.0138$	$\gamma_{111} = -2.1240$

Additionally, the onset of melting of the 2.55 nm c-BN octahedron nanoparticle is about 3000K, and melting starts from the corners according to the discussion in Chapter 4. Therefore, we find that the sintering at 3100 K initial temperature in NVE simulation is slightly different than that at lower temperatures. There are 17 cases showing vertex-to-vertex collision, where the tips stick together at the initial stage of sintering, and then turn into either B-N contact, B-B contact, or melted vertex-to-facet contact within the 3 ns simulation time, as exhibited in Figure 6-16. Moreover, we see some collisions which are initially nitrogen on nitrogen facets (N-N collisions), but rotate into the stable B-B or B-N configuration; and some B-B and B-N cases can rotate into B-N and B-B, respectively. Most importantly, no B-B or B-N collision are seen turning into N-N cases, as expected given the instability of the N-N bond at high temperatures.

In the next section, we choose some B-N collision cases and simulate them in NVE conditions for a longer duration (50 ns) to study the grain growth, diffusion, and sintering with respect to temperature.

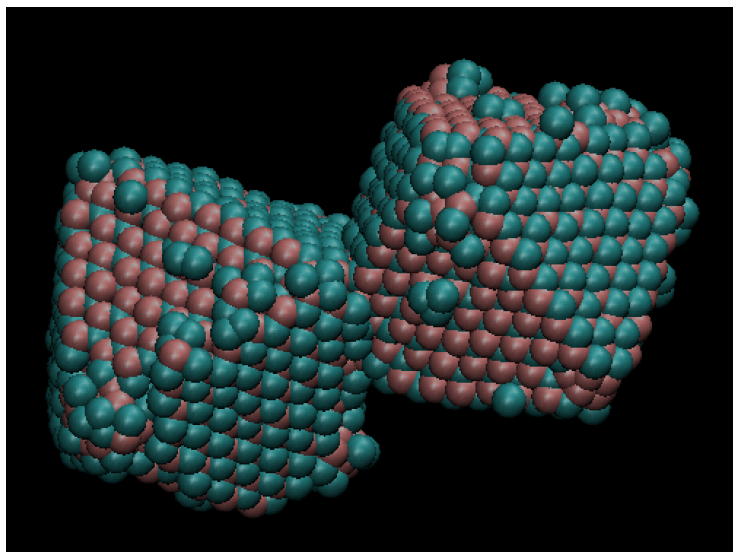


Figure 6-16. Vertex-to-facet case at $T=3100\text{K}$.

6.3 Sintering of c-BN Nanoparticles

The initial orientation of the B-N collision case investigated is displayed in Figure 6-17. It is run in NVE for 50 nanoseconds at initial temperatures of 2500 K, 2700 K, 2900 K, and 3100 K, which will be discussed in the following sections.

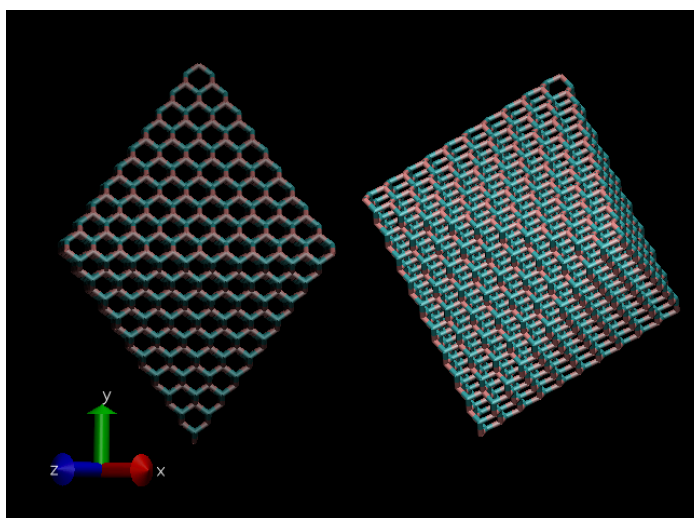


Figure 6-17. Initial configuration of NP2 with rotation along z-axis of 106° & along new x-axis of 73° .

6.3.1 2500 & 2700 Kelvin

In the NVE simulation with an initial temperature of 2500 K, the mid-sections of the two octahedral nanoparticles collide at 70ps, forming a B-N interface, as illustrated in Figure 6-18(a). Figure 6-18(b) shows the simulation at 3ns, where there is no obvious grain growth in the contact area within this simulation time period. Meanwhile, some corners of the octahedrons have started melting. At the end of the simulation (50ns), grain growth can be seen in the contact area as circled in Figure 6-18(c); Figure 6-18(d) displays the same view as Figure 6-18(c) but with a different presentation to better show how some nitrogen (green) atoms have diffused on the surface and are covering the boron cluster formed at the corner. At the end of simulation, the final temperature is around 2590 K, and the nanoparticles still remain in octahedral shape at 50 ns.

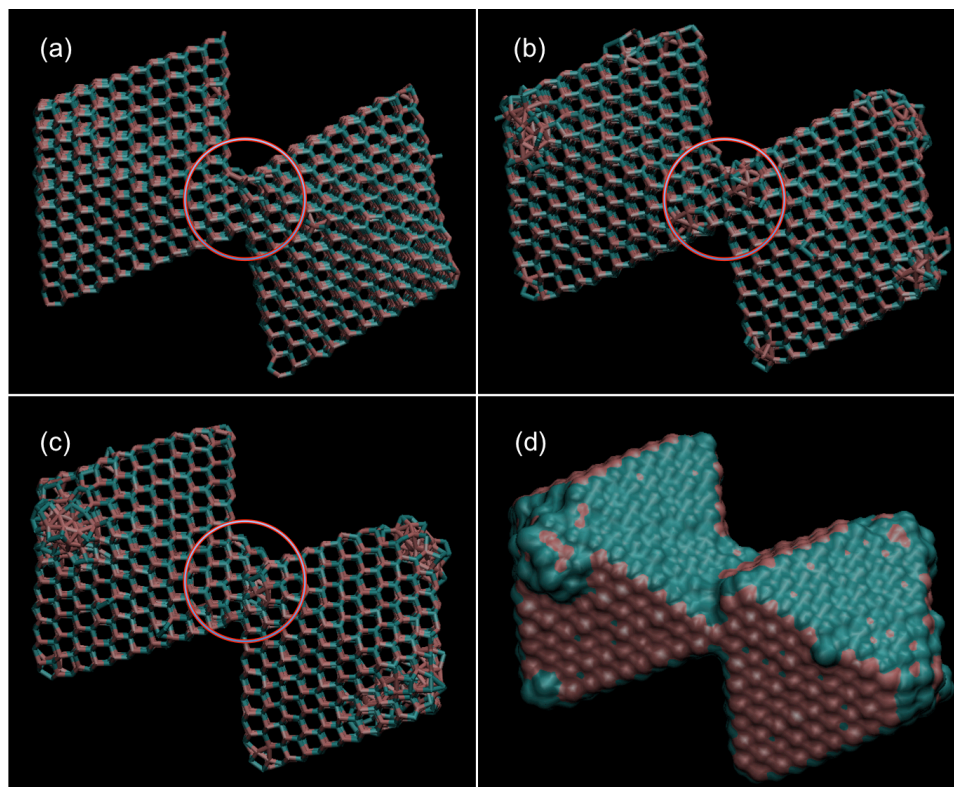


Figure 6-18. NVE simulation with initial temperature of 2500K for 50ns (a) 70ps (b) 3ns (c) 50ns (d) 50ns with surface presentation.

When the initial temperature is raised to 2700 K, the first collision of the two nanoparticles is very similar to the case at 2500 K, i.e. contact around the mid-section of the octahedron. Figure 6-19(a) presents the top view of the two nanoparticles after collision at 70 ps, and Figure 6-19(b) presents the same view at the end of the 50 ns simulation time. Sliding of the contact surfaces is observed at this temperature, along with grain boundary diffusion as shown from step (a) to (b) in Figure 6-19. The well-developed BN boundary is indicated in Figure 6-19(c), and some corners have melted. Using the surface presentation in Figure 6-19(d), it is easier to see the accumulation of diffused nitrogen atoms on the surface. In this case, the final temperature is around 2830 K, and the nanoparticle starts to lose its octahedral shape.

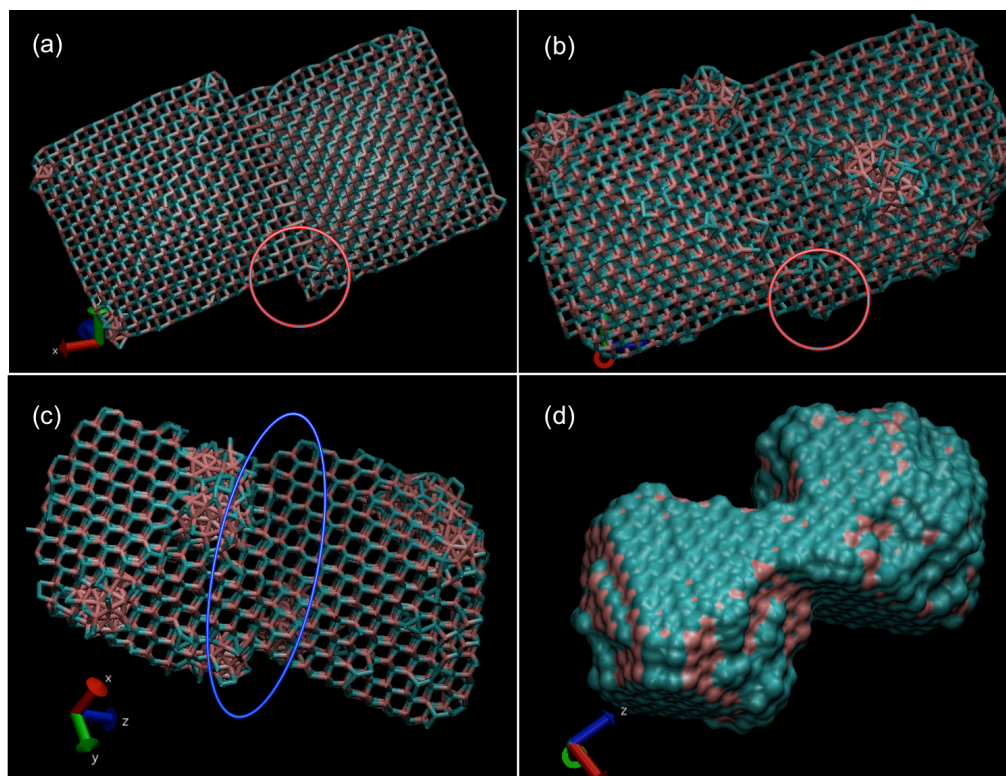


Figure 6-19. NVE simulation with initial temperature of 2700K for 50ns. (a) 70ps (b) 50ns with top view (c) 50ns with side view (d) 50ns side view with surface presentation.

6.3.2 2900 & 3100 Kelvin

In the NVE simulation with an initial temperature of 2900 K, we observe the crystallographic alignment between two nanoparticles. Figure 6-20(a) shows the initial contact of the nanoparticles. The circled areas display the different orientation of the two nanoparticles, where the two $\{111\}$ facets indicated point in different directions, and the normal vector for these two surfaces are not parallel. However, after evolving for 38ns, as shown in Figure 6-20(b), the orientation of the $\{111\}$ facets have aligned together, as revealed in the circled areas, i.e. the normal vectors are now parallel. The temperature at 38ns is about 3050K, which is slightly higher than the melting temperature of a 2.55nm octahedron. This important development will aid in the sintering process by allowing the growth of a $\{111\}$ facet across the entire conjoined nanoparticle, as shown below.

We then further investigate the sintering of these two nanoparticles. Figure 6-21(a) still shows the evolution at 38 ns, but from a different view highlighting that the nanoparticles are losing their octahedral shape due to melting of the corners. At 43 ns, one side of the sintered nanoparticle starts to develop visible growth of the two $\{111\}$ facets that were aligned at 38 ns (the right side of the sintered nanoparticle in Figure 6-21(b)), and the surface keeps growing as shown in Figure 6-21(c). The right side of Figure 6-21(b) is the atomic view of the flat surface at 45 ns ($T=3200\text{K}$), exhibiting a well-developed $\{111\}$ facet that has evolved from the merged octahedron nanoparticles. Boron clusters also grow at the corners of the sintered nanoparticle as shown in Figure 6-21(a) & (b). Figure 6-21(d) & (e) displays the sintered nanoparticle at 48 ns ($T=3300\text{K}$) and 49 ns ($T=3350\text{K}$) respectively. Phase separation is spreading towards the center of

the entire sintered nanoparticle, and almost complete segregation is seen at 50ns ($T=3850\text{K}$), as shown in Figure 6-21(f).

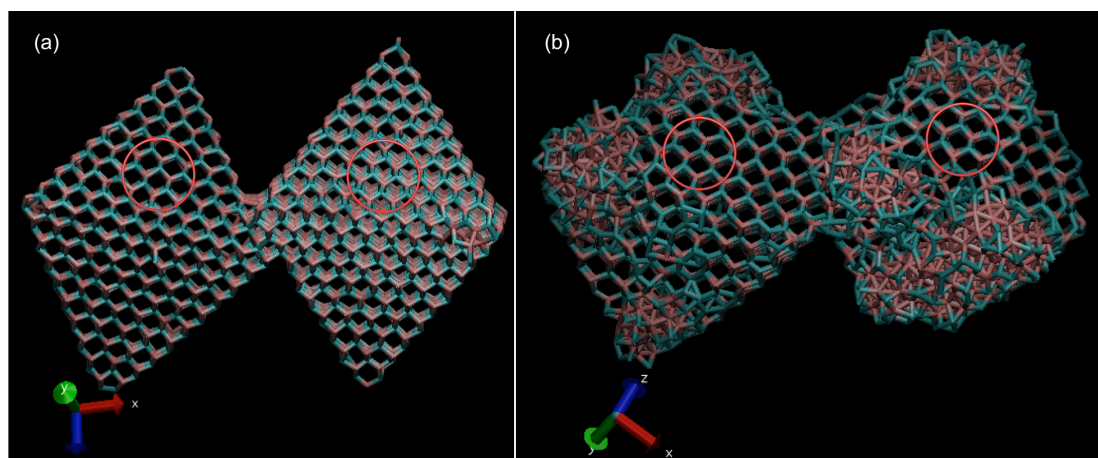


Figure 6-20. NVE simulation with initial temperature of 2900K for 50ns. (a) 100ps (b) 38ns.

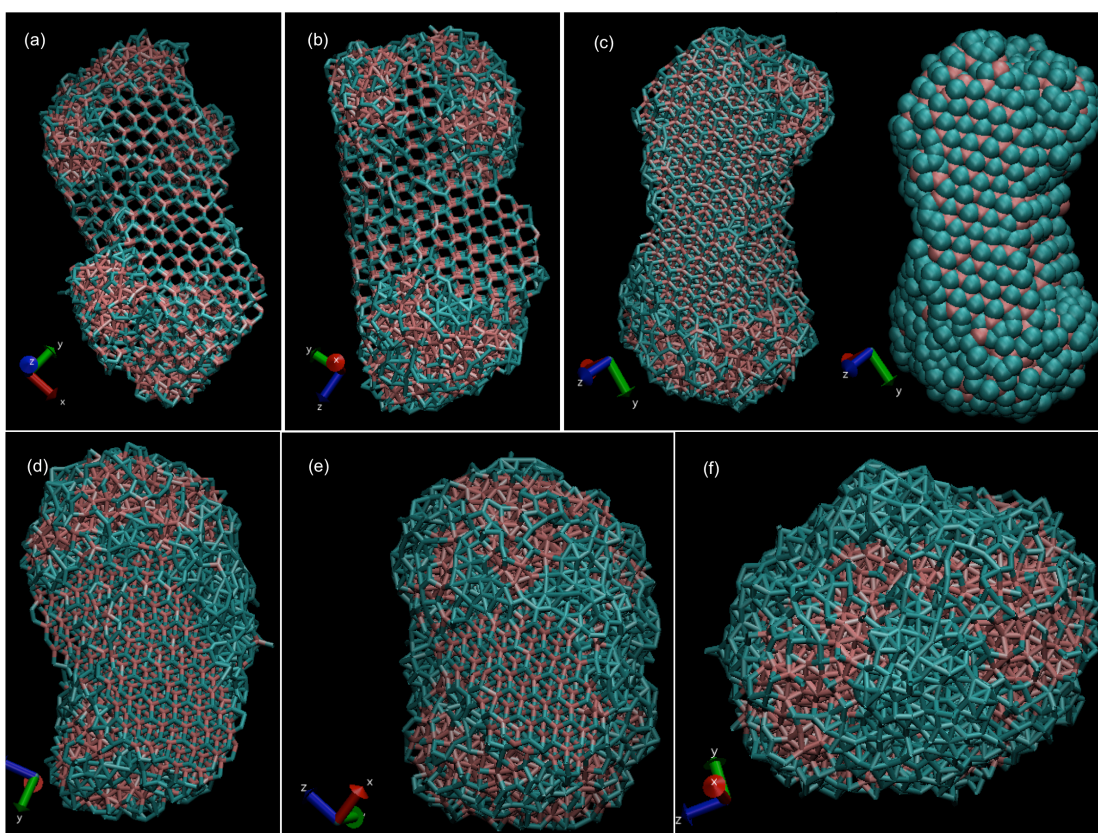


Figure 6-21. NVE simulation with initial temperature of 2900K for 50ns. (a) 38ns (b) 43ns (c) 45ns: the bond presentation on the left and atom presentation on the right (d) 48ns (e) 49ns (f) 50ns: phase separation taking place.

Finally, the 3100 K case is presented in Figure 6-22, with the left and right columns representing the top view and side view of the nanoparticles, respectively. The circled areas represent the grain boundaries. The two nanoparticles are well aligned initially, thereby allowing proper growth of a single $\{111\}$ surface, as evidenced by the clear neck growth at the point of contact from Figure 6-22(a) to (d). From Figure 6-22(a) to (d), grain growth is clearly seen at the boundary from the side view of the nanoparticles, while the top view reveals that melting has started from the corner. Melting then proceeds to the edges and surfaces, and the phase separation-driven melting causes the amorphous boron clusters to grow and finally spreads throughout the entire sintered nanoparticle. The complete phase separation occurs earlier at 16.5 ns due to the higher sintering temperature of 3540K.

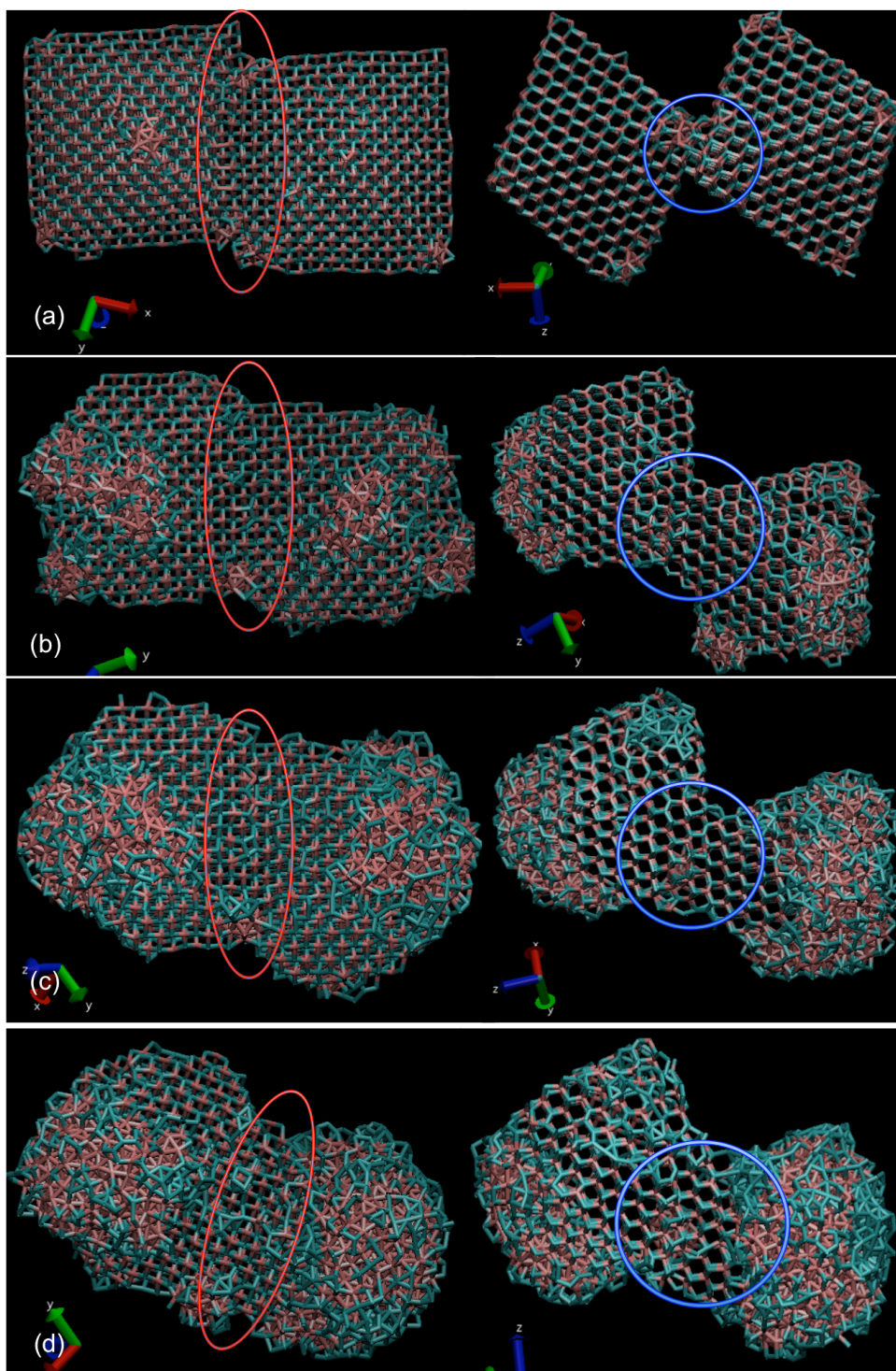


Figure 6-22. NVE simulation with initial temperature of 3100K for 50ns. (a) 100ps with $T=3050\text{K}$ (b) 8ns with $T=3125\text{K}$ (c) 12ns with $T=3230\text{K}$ (d) 15ns with $T=3320\text{K}$.

6.3.3 Concluding Remarks

In NVE simulation conditions, an initial temperature is set for the entire system, and the temperature of single nanoparticles are chosen to be between 50 to 100 degrees Kelvin lower than the target temperature. When the two nanoparticles collide, the temperature typically increases by tens to hundreds of degrees Kelvin, depending on the change in potential energy, i.e. the contact area and type of bonds formed. The maximum temperature change for the boron-nitrogen collision case with full facet-on-facet contact from the statistical study of particle-particle collisions, i.e. the maximum gain in potential energy, is about 170 K with a ΔKE of 85 eV. For the full-facet boron-boron collision case, it is 160 K with a ΔKE of 72 eV.

From the discussion in the section on sintering, we know that grain growth at the boundary of collided nanoparticles can occur at around 2600 K without complete melting of the octahedral shape of the c-BN nanoparticle. Furthermore, phase separation does not affect the sintering process since the sintering temperature is a few hundred-degrees Kelvin lower than the characteristic melting temperature of a 2.55 nm octahedron c-BN nanoparticle. When the temperature rises up to around 2830 K, crystalline grain growth occurs at the boundary, even though some corners of the octahedrons have started melting. In the NVE simulation with an initial temperature of 2900K, the sintering temperature exceeds 3000 K at 25 ns, and continues increasing gradually because of the on-going sintering process. Upon going beyond the melting temperature at 3000K, the two separate $\{111\}$ facets of the collided nanoparticles begin aligning, which allows for crystalline grain growth and formation of a single $\{111\}$ facet across the entire sintered nanocluster. Finally, coalescence ensues and results in the evolution of a flat and well-

developed $\{111\}$ surface. However, when the temperature exceeds 3200K, phase separation starts propagating aggressively towards the center of the sintered nanoparticle, and eventually spreads out all over the entire cluster. In our final case study, the highest temperature of the aggregated nanoparticle at the initial stage of sintering is approximately 3050K, as shown in Figure 6-22(a). Rapid grain growth is again observed in the temperature range of 3050K to 3320K, and as mentioned earlier, phase separation again engulfs the entire cluster when the temperature exceeds 3200K.

Since most c-BN powders are a mixture of $\{111\}$ and $\{100\}$ facets, the onset of melting can happen at temperature as high as 3100K, if $\{111\}$ facets dominate (like truncated octahedron). Or onset can be as low as 2700K, if $\{100\}$ facets dominate (like cuboctahedron), for the size range of 2 to 3 nm that have been analyzed. Furthermore, the probability of boron-nitrogen collision increases with temperature. Therefore, in order to achieve coalescence of mainly $\{111\}$ faceted c-BN nanoparticles without phase separation taking over the sintering process, we propose that the initial temperature be set at 2900K, which should maintain the sintering temperature at around 3050K for 2-3 nm sized c-BN nanoparticles.

6.4 References

1. Zhu H. Sintering processes of two nanoparticles: A study by molecular dynamics simulations. *Philosophical Magazine Letters*. 1996;73(1):27-33.
2. Baletto F, Ferrando R. Structural properties of nanoclusters: Energetic, thermodynamic, and kinetic effects. *Reviews of modern physics*. 2005;77(1):371.
3. Koparde VN, Cummings PT. Phase transformations during sintering of titania nanoparticles. *ACS nano*. 2008;2(8):1620-1624.

4. Taniguchi T, Akaishi M, Yamaoka S. Sintering of cubic boron nitride without additives at 7.7 GPa and above 2000 C. *J Mater Res*. 1999;14(01):162-169.
5. Zhao Y, Wang M. Effect of sintering temperature on the structure and properties of polycrystalline cubic boron nitride prepared by SPS. *J Mater Process Technol*. 2009;209(1):355-359.
6. Mishima O, Era K. Science and technology of boron nitride. *Electric Refractory Materials*. 2000:495-556.
7. Tian Y, Xu B, Yu D, et al. Ultrahard nanotwinned cubic boron nitride. *Nature*. 2013;493(7432):385-388.
8. Bullett D. Structure and bonding in crystalline boron and B₁₂C₃. *Journal of Physics C: Solid State Physics*. 1982;15(3):415.

Chapter 7

7 Conclusions and Future Work

7.1 Review of Results and Conclusions

The focus of this thesis is the melting mechanism of c-BN nanoparticles using MD simulations. In particular, the emphasis here is on octahedral nanoparticles which consist solely of $\{111\}$ facets. A careful study of three different potentials typically employed to describe covalent bonds in binary systems, namely the Tersoff, Albe, and Stillinger-Weber potentials are conducted and assessed for their suitability to be applied to nanoparticle systems. Via a series of MD simulations of c-BN bulk crystals, the modified SW potential, adopted from Moon and Hwang's results, is determined to be most apropos for simulating c-BN nanoparticles in the high temperature regime of interest.

The next stage of research utilizes this modified SW potential to analyze the surface energy of the $\{100\}$, $\{110\}$, and $\{111\}$ c-BN crystallographic surfaces. This analysis determines that the stability of c-BN nanoparticles is severely affected by geometry, which plays a leading role in the melting behavior of small-sized nanoparticles. Based on surface energy considerations, the octahedron is the most stable, followed by truncated-octahedron, cuboctahedron, and cube being the least stable. However, the molecular dynamics simulations reveal that the specific truncated octahedron studied here melts at higher temperatures than the octahedron due to surface reconstruction effects.

As detailed in Chapter 4, the least stable $\{100\}$ facet undergoes significant surface reconstruction even at near room temperatures. In the MD simulation of the cube nanoparticle at 400K in NVE conditions, all the $\{100\}$ facets undergo complete

dimerization to form either boron dimerized or nitrogen dimerized $\{100\}$ facets and start to melt around 2300K. More dramatically, patches of the $\{100\}$ facet reconstruct into the most stable $\{111\}$ facet at 2902K, near the onset of melting of the $\{111\}$ facet. This outcome is in line with the underlying principle of minimizing the ground state energy of the nanoparticle, as discussed in Chapter 3. The stabilizing effect of this surface reconstruction of $\{100\}$ facet is reflected in a suppression of the bond fluctuation just before the onset of $\{111\}$ facet melting. Similar analyses for the cuboctahedron and truncated octahedron divulge the same mechanism at work on the $\{100\}$ facets. Consequently, the truncated octahedron is more dynamically stable with respect to the octahedron owing to the formation of dimer-stabilized $\{100\}$ facets, resulting in a higher melting temperature.

The melting mechanism is studied in detail; and most surprisingly, phase separation of boron nitride occurs during the melting of c-BN nanoparticles, resulting in formation of a boron-core/nitrogen-shell structure. We focus on octahedral shaped c-BN nanoparticle, as it consists solely of the most stable $\{111\}$ facet. MD simulations are conducted in both the NVE microcanonical ensemble and the NVT canonical ensemble. Chapter 5 discusses the results visualized by post-processing the MD simulation results in VMD at different time steps, which allows tracking the initiation and progression of melting, as well as the physical segregation of the boron and nitrogen atoms throughout the melting process. This analysis allows clear observation of corner-initiated melting and the simultaneous phase separating that occurs. Two quantitative measures, i.e. the Lindemann index and the number of B-N, B-B, and N-N bonds, are also tracked as

functions of time, with the results supporting our picture of corner-initiated melting and phase separation.

The results reveal that melting initiates from the corners and edges because the atoms with lower coordination number act as the nucleation sites for the onset of melting. The boron-nitrogen bonds at the vertices start to break, and boron clusters begin to form. In addition, extensive diffusion of nitrogen atoms occurs on the surface of the nanoparticle, as well as from the interior to the surface due to vaporization of surface nitrogen atoms. This stage is then followed by melting of the edges with formation of dimer-stabilized $\{100\}$ facets between $\{111\}$ facets, with the resulting partially-melted nanoparticle strongly resembling a truncated octahedron. This behavior provides further support for the truncated octahedron, with dimer-stabilized $\{100\}$ facets, being the most stable shape. Finally, complete melting is marked by full phase separation with formation of a boron-rich core and a nitrogen-rich shell. This prediction is seemingly supported by our laser heating of c-BN micropowders experimental results, which show boron nanoparticles intermixed with nanocrystalline c-BN.

The size dependence of the melting point of octahedral nanoparticles is also reported here, and we conclude that the size effect on melting is significant for small c-BN nanoparticles with a total number of atoms less than 5000 from MD simulation results. In addition, we compare our result with existing models of melting point depression, showing good agreement with the theoretical model that includes geometrical considerations.

Finally, the statistical study of particle-particle collision of two equal-sized octahedral c-BN nanoparticles is carried out in NVE simulations. Various initial

temperatures, from 2500 K to 3100 K, in 200K increments, are examined to gain basic understanding of the sintering behavior of 2.55-nm sized octahedral c-BN nanoparticles. As discussed in Chapter 6, the nitrogen-nitrogen facet collision is found to be least favorable due to the weakest binding energy among B-N, B-B, and N-N bonds. N-N is highly unstable at these high temperatures as evidenced by the large nitrogen diffusion observed. The total number of B-N collision cases at each temperature increases with increasing initial temperature, while the total number of B-B collision cases diminishes as sintering temperature goes up. These results indicate that the B-B bond becomes less stable as temperature increases, whilst the B-N bond in the cubic boron nitride tetrahedral structure remains stable.

The chosen B-N collision case is investigated in NVE simulations for a longer period of time (50 ns) to evaluate the optimal temperature range for sintering. The results show that the alignment of the $\{111\}$ orientation of the two-aggregated nanoparticles occurs at a temperature around 3050K, which is an important development that will aid in the sintering process by allowing the growth of a $\{111\}$ facet across the entire conjoined nanoparticle. In addition, rapid grain growth is observed when the sintering temperature is between 3100K and 3250K. However, phase separation also takes place at the corners away from the plane of collision of the aggregated nanoparticles at high temperatures, engulfing the entire sintered nanocluster as the temperature exceeds 3300K. Therefore, in order to achieve coalescence of mainly $\{111\}$ faceted c-BN nanoparticles without phase separation taking over the sintering process, we propose that the initial temperature be set at 2900K, maintaining the sintering temperature at around 3050K for 2-3 nm sized c-BN nanoparticles.

7.2 Suggestion for Future Work

This dissertation provides several key insights into the melting behavior of c-BN nanoparticles, with special focus on surface reconstruction on $\{100\}$ facets and corner-initiated melting of octahedron nanoparticles composed of eight $\{111\}$ facets. This work also lays out the fundamental processes for understanding particle-particle collision and sintering of c-BN nanoparticles using MD simulations. Based on this foundation, another geometry of c-BN nanoparticle, i.e. truncated octahedron-like structure with a mixture of $\{111\}$ and $\{100\}$ facets, should be further investigated in the sintering and aggregation of c-BN clusters. Moreover, the consequence of the phase separation on melting and sintering of c-BN should be a significant consideration in the consolidation of c-BN powders. Hence, detailed and carefully designed experiments for further study of the phase separation phenomenon is an interesting and important direction for future work.

Finally, the melting point of diamond crystals is about 1000K higher than c-BN crystals, despite having the same crystalline structure and similar bond strength and elastic properties. An interesting perspective arisen from this work poses the question: does phase separation of compounds drive their melting, resulting in a much lower melting temperature? This issue can be addressed by a detailed examination and comparisons to diamond using MD simulations.